University of California
Santa Barbara

Extending classical nucleation theory: Understanding the effects of trace additives and inhomogeneous concentration distributions

A dissertation submitted in partial satisfaction
of the requirements for the degree

Doctor of Philosophy
in
Chemical Engineering

by

Geoffrey G. Poon

Committee in charge:

Professor Baron Peters, Chair
Professor Glenn Fredrickson
Professor Ram Seshadri
Professor M. Scott Shell

January 2018

The Dissertation of Geoffrey G. Poon is approved.

Professor Glenn Fredrickson

Professor Ram Seshadri

Professor M. Scott Shell

Professor Baron Peters, Committee Chair

December 2017

Extending classical nucleation theory: Understanding the effects of trace additives and inhomogeneous concentration distributions

by

Geoffrey G. Poon

Dedicated to my family: Michelle, Gary, and Lily Poon.

Acknowledgements

I have been incredibly blessed to be surrounded by so many friends, family members, colleagues, and mentors. This list is hardly complete, but I hope these acknowledgments express my gratitude to those whom have supported me and helped me grow personally and professionally.

First, I would like to thank my advisor, Baron Peters. Six years ago, I had no experience doing research in a computational group, and I never would have imagined myself running simulations and deriving new theories. However, his guidance made it all possible. Over the past five-and-a-half years, he helped me learn a great deal about statistical mechanics, nucleation and other rare events, and reaction rate theory. But more importantly, he taught me how to think about new problems, discover new avenues for research, ask the right questions, and communicate my ideas clearly and concisely. I know these are skills helped me succeed as a graduate student and will continue to help me well beyond my Ph.D. studies.

I would also like to thank my committee members, Glenn Fredrickson, Ram Seshadri, and Scott Shell. Their invaluable insights and advice were incredibly helpful.

I've also been incredibly lucky to be surrounded by the brilliant past and present members of the Peters and Shell group and other UCSB colleagues. Starting from the moment I first joined the Peters group,the senior members (Nathan Duff, Ryan Mullen, and Bryan Goldsmith) helped me get up to speed. I am not sure where I would be without them answering my stupid questions regarding the cluster or discussing our own research. Sean Cray was another amazing resource when I first started. He graciously volunteered his time to organize reading groups, help me learn the fundamentals, and talk through problems in my own research. I would also like to thank Mark Joswiak, Nils Zimmerman, Kartik Kamat, Jacob Monroe, Dave Smith, and Tanmoy Sanyal for

constantly indulging my love for whiteboard sessions and discussions. I have always learned best by discussing ideas with others, and they provided the perfect environment to do just that. I also need to thank all of the undergraduates and collaborators who contributed to my research, especially Tobias Lemke and Stefan Seritan who contributed a great deal to projects detailed in this thesis.

My research would also not be possible without the emotional support of the friends I made at UCSB, especially Nick Cadirov and Doug Vogus (two awesome roommates who share my love for sports), Rodrigo Nery Azevedo, Anirudha Banerjee, John Henske, Arash Nowbahar, Ian Williams, Vahagn Yeranossian, and Christi Peterson. Whether we were exploring downtown Santa Barbara, laughing over wine and beer, barbecuing on the beach, camping along the coast, playing basketball, or "ruining" friendships over board games, they helped make my experience in Santa Barbara outside of Engineering II so memorable. I know I have made lifelong friends here, and I look forward to our next set of adventures.

Finally, I have to thank my parents (Gary and Lily Poon) and my big sister (Michelle Poon). I cannot imagine my life without their love, support, and encouragement. Michelle, you have been one of my greatest mentors from day one. Growing up, I always looked up to you. You taught me perseverance and to pursue my dreams. But more importantly, you have been one of my best friends. I could always confide in you and count on you to pick me up when life has me down. Mom and Dad, you are the one who seeded my love for science. You did everything you could to ensure I had every possibility to grow intellectually. Those after-school courses really paid off! You also gave me the freedom to explore my own passions. But most importantly, you taught me how to be a better person. You taught me morals, work ethic, and compassion. I am sorry that I might never be able to convey how honored I am to be your son.

And to everyone else who helped me along the way. I am truly grateful.

Curriculum Vitæ

Geoffrey G. Poon

Education

2017	Ph.D. in Chemical Engineering (Expected), University of California, Santa Barbara. Advisor: Prof. Baron Peters
2012	B.S. in Chemical Engineering, University of California, Berkeley.

Honors and Awards

- National Science Foundation (NSF) Graduate Research Fellowship, 2013
- University of California, Berkeley Department of Chemical and Biomolecular Engineering Undergraduate Researcher Award, 2012

Publications

1. Poon, G. G., Lemke, T., Peter, C., Molinero, V., and Peters, B. (2017). "Oligomeric Nucleants: Simulations of Chain Length, Binding Strength, and Volume Fraction Effects." The Journal of Physical Chemistry Letters.
2. Padmanabhan, S., Schwyter, P., Liu, Z., Poon, G., Bell, A. T., and Prausnitz, J. M. (2016). "Delignification of miscanthus using ethylenediamine (EDA) with or without ammonia and subsequent enzymatic hydrolysis to sugars." 3 Biotech, 6(1), 23.
3. Poon, G. G., and Peters, B. (2015). "Accelerated nucleation due to trace additives: a fluctuating coverage model." The Journal of Physical Chemistry B, 120(8), 1679-1684.
4. Poon, G. G., Seritan, S., and Peters, B. (2015). "A design equation for low dosage additives that accelerate nucleation." Faraday discussions, 179, 329-341.
5. Poon, G. G., and Peters, B. (2013). "A stochastic model for nucleation in the boundary layer during solvent freeze-concentration." Crystal Growth and Design, 13(11), 4642-4647.
6. Rodrguez, H., Padmanabhan, S., Poon, G., and Prausnitz, J. M. (2011). "Addition of ammonia and/or oxygen to an ionic liquid for delignification of miscanthus." Bioresource technology, 102(17), 7946-7952.
7. Xin, Q., Poon, G. G., and Prausnitz, J. M. (2010). "Fluid-phase equilibria in binary systems containing an ionic liquid. Application of the PercusYevickvan der Waals equation of state." The Journal of Supercritical Fluids, 55(2), 817-824.

Abstract

Extending classical nucleation theory: Understanding the effects of trace additives and inhomogeneous concentration distributions

by

Geoffrey G. Poon

Nucleation is the first step in the conversion of a metastable phase to a more stable one. It involves the formation of a post-critical nucleus that is thermodynamically favorable to grow and is important in most phase transitions. Our understanding of the thermodynamics and kinetics of nucleation is largely based on classical nucleation theory (CNT). It was formulated on the basic principle developed by Gibbs, who reasoned that the free energy required to form a nucleus involves two competing contributions: (1) a favorable bulk driving force and (2) an unfavorable surface penalty, and the subsequent work by Volmer and Weber, Farkas, Becker and Doring, and Zeldovich that developed rate laws. Almost 100 years later, most studies of nucleation still borrow at least some elements of CNT. Although CNT provides a simple and intuitive framework to understand nucleation, it is not applicable in many important situations.

In this thesis, we develop corollary theories that adapt CNT to understand solute precipitate nucleation when different factors affect the driving force or surface energy. We introduce a spatio-temporal survival probability model to provide the first stochastic model of nucleation due to solute enrichment ahead of a crystallizing front. The model predicts the distribution of nucleation times as a function of CNT rate parameters and growth conditions. Finally, we investigate how adsorbing additives can promote nucleation. We created a theoretical framework for modeling the thermodynamics and kinetics of solute precipitate nucleation when molecular surfactants can adsorb onto nuclei and

reduce the surface energy. We also used lattice simulations to study how properties of adsorbing molecular and oligomeric additives affect nucleation barriers.

Contents

Chapter 1

Introduction to nucleation

1.1 Background

A thermodynamic phase is a region of space with essentially uniform physical properties (e.g. density and chemical composition). Different phases are often physically and/or chemically distinct and are stable at different thermodynamic conditions (i.e. temperature, pressure, and composition). However if two phases coexist at equilibrium, they are equally stable, and the thermodynamic conditions define the coexistence or binodal curve on a phase diagram. If the system is not in equilibrium, one phase will have a lower free energy and be *truly stable* while the higher free energy phase will be *metastable.*[1] The transition from the metastable phase to the stable phase is a first-order phase transition from a metastable state.[1] A common example of a first-order phase transition is the boiling of water which involves converting pure liquid water (a high density fluid) to a vapor (a low density fluid), as shown in Figure 1.1a. The metastable state is created by heating water above its boiling point. Beyond the boiling point, water vapor is more sta-

[1]For the sake of completeness, the chemical potential of each phase is equivalent but their first derivate (i.e. molar volume) is not for first-order phase transitions at equilibrium.

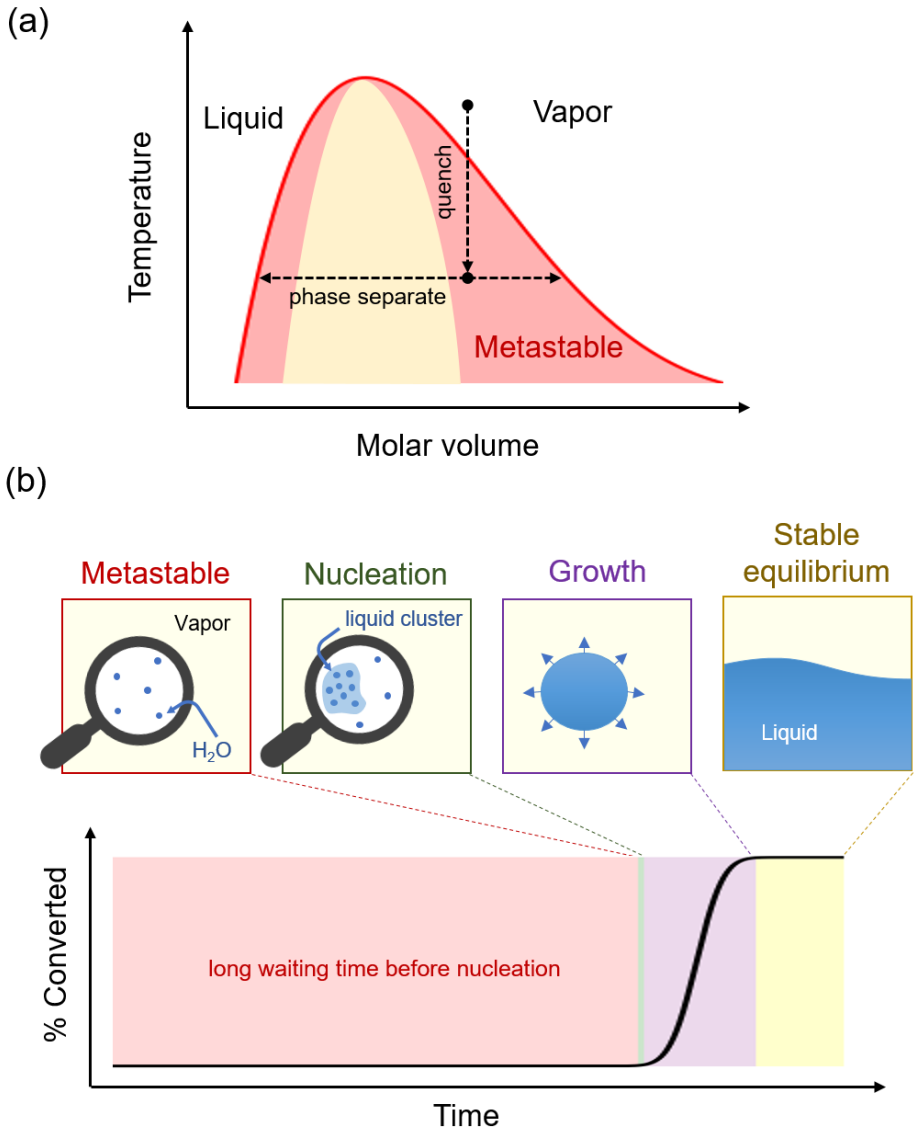

Figure 1.1: (a) Quench and phase separation path overlaid on top of a phase diagram. Shows that a more stable phase will be born from the metastable one. The metastable zone is shown in red, and the unstable region under the spinoidal curve is shown in yellow. (b) A schematic of liquid-vapor water nucleation which also illustrates the time scale separation between waiting times and the length of a nucleation event.

ble, and the superheated liquid is converted into water vapor. Metastable states in other systems can also be prepared by quickly changing the thermodynamic conditions (e.g. temperature, pressure, and/or composition) until a different phase is the more stable equilibrium state.

Phase transitions occur because of the necessity for the system to occupy the lowest free energy state at macroscopic equilibrium. However, the transition is often not instantaneous, and the metastable state can persist for a long time (see Figure 1.1b). For example, distilled water can survive indefinitely without freezing at $-10°\mathrm{C}$.[2] This long lifetime is because the initial state is *metastable* instead of unstable. Metastable states are stable to small thermal fluctuations; however, eventually there is a rare fluctuation that is large enough to drive the formation of clusters of the more stable phase. This process of cluster formation is nucleation.

Since nucleation is the first step in many phase transitions, the ability to understand, predict, and control nucleation is of great practical significance. Even if we just consider pure water systems, nucleation has many implications including heat transfer in boilers,[3] ice and cloud formation in the atmosphere,[4,5] and intracellular freezing of biological organisms in subzero environments.[6,7] Nucleation and the early stages of crystallization can also affect properties, such as polymorph type, shape, and purity, of crystalline ingredients of pharmaceutical drugs.[8] These properties can affect the drug's bio-availability and down-stream processing. The nucleation and growth of gas hydrates can result in the plugging and corrosion of oil and gas pipelines where the temperature is low and the pressure is high.[9]

Unfortunately, our ability to study nucleation via experiments is limited by the time and length scales of nucleation. Nucleation has two relevant time scales: (1) the induction time or waiting time and (2) the formation time or transition path time. The induction time is a measure of how long the metastable phase persists before a phase transition

occurs and, as we mentioned previously, can be as long as days. However, the time for a cluster of the stable phase to form and grow to post-critical size is often much faster and can be as short as a few nanoseconds. The large separation time scales makes it difficult to study nucleation. To obtain enough statistics to study a stochastic process, an experiment should be carried out over a long time (i.e. hours to days) observe tens to hundreds of nucleation events. But measurements to detect and characterize nuclei should be taken *very* quickly (i.e. nanoseconds) to study the properties of near-critical nuclei, which quickly redissolves or grows to macroscopic size. This means measurements are ideally taken very frequently over the entire experiment to probe nucleation. In addition to the separation of time scales, the nano-scale size of nuclei makes it even more difficult for experiments to directly observe nucleation and typically limits studies to rate measurements from induction time data. Therefore, it is especially important to use theory and simulations to connect these rate measurements to physically meaningful parameters and mechanistic insights.

In the following sections, we will briefly review classical nucleation theory (CNT) and suggest opportunities to extend its theoretical framework. We outline the thermodynamics and kinetics of both homogeneous (HON) and heterogeneous nucleation (HEN). We finally discuss the assumptions built into CNT and the opportunities to relax them using corollary theories.

1.2 Classical nucleation theory (CNT)

1.2.1 Thermodynamics of nucleation

The thermodynamic foundation of classical nucleation theory (CNT) was developed by J.W. Gibbs.[2] Gibbs reasoned that the free energy required to form a nucleus involves two competing contributions: (1) a favorable (negative) bulk free energy driving force and (2) an unfavorable (positive) surface free energy penalty.

Homogeneous nucleation (HON)

For homogeneous nucleation (HON), the free energy to create a cluster composed of n molecules or building units is (see Figure 1.2)

$$F_{\mathrm{CNT}}(n) = -n\Delta\mu + \gamma a\phi n^{2/3}, \tag{1.1}$$

where $\Delta\mu$ is the positive difference between the chemical potential of the metastable parent phase and that of the more stable nucleating phase and γ is the interfacial free energy per unit area. ϕ is a shape factor and a is an area term such that $a\phi n^{2/3}$ is the surface area of the cluster. The competition between the unfavorable surface term and favorable bulk term gives $F_{\mathrm{CNT}}(n)$ its non-monotonic behavior, which we will discuss later in this section.

The constant value of $a\phi$ is due to the CNT assumption that the shape of clusters are approximately the same for all sizes. That constant can be derived for any geometric cluster shape, but the most commonly assumed shape is a sphere. For a spherical nucleus of size n, the volume the cluster occupies is $nv_0 = 4\pi R^3/3$ where v_0 is the volume of the

[2]The longer I study thermodynamics, the more convinced I am that Gibbs has his impact on almost every field in thermodynamics. It is no surprise that Albert Einstein called him "the greatest mind in American history." (J. Willard Gibbs, *Physics History.* American Physical Society)

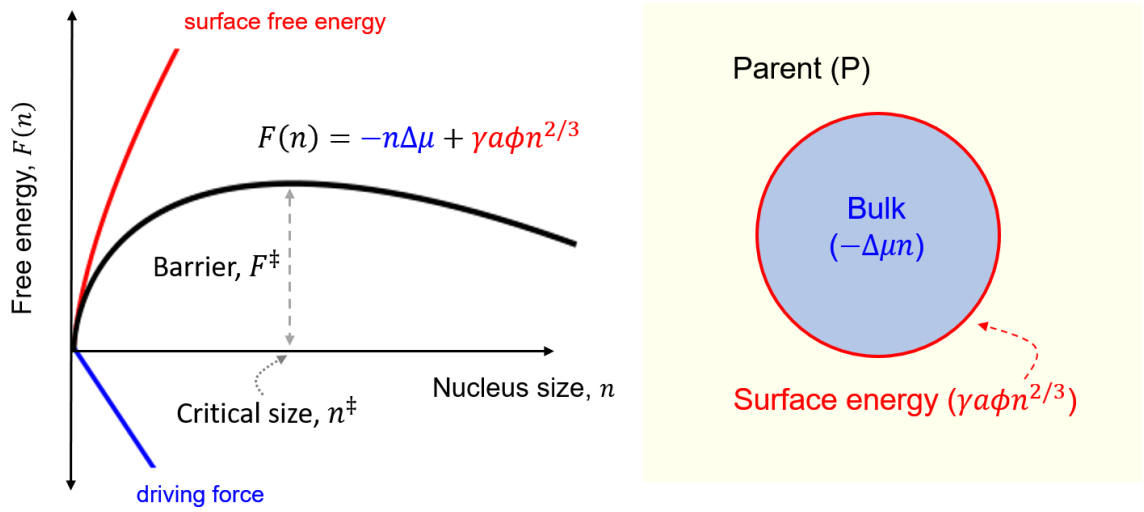

Figure 1.2: Diagram of classical nucleation theory free energy model for homogeneous nucleation and the two competing contributions: unfavorable surface free energy and favorable driving force.

nucleating phase per building unit and $R = (3nv_0/4\pi)^{1/3}$ is the radius of the nucleus. $a\phi$ is therefore

$$a\phi = 4\pi \left(\frac{3v_0}{4\pi}\right)^{2/3} \approx 4.84 v_0^{2/3}. \tag{1.2}$$

$a\phi v_0^{-2/3}$ is larger for other three dimensional shapes because of the increased surface area to volume ratio (e.g. $a\phi \approx 7.21 v_0^{2/3}$ for tetrahedrons, $a\phi \approx 6 v_0^{2/3}$ for cubes, and $a\phi \approx 5.72 v_0^{2/3}$ for octahedrons).

The thermodynamic driving force $\Delta\mu$ is

$$\Delta\mu = k_B T \ln(f_0/f_{\text{sat}}) \tag{1.3}$$

for nucleation in the gas phase and

$$\Delta\mu = k_B T \ln(a_0/a_{\text{sat}}) \tag{1.4}$$

for nucleation in a liquid solution where f_0 and a_0 are the fugacity and activity of the nucleating species and f_{sat} and a_{sat} are the equilibrium fugacity and activity. For sufficiently low concentrations, the ratio of fugacities f_0/f_{sat} and activities a_0/a_{sat} is commonly estimated as the supersaturation $S = c_0/c_{\text{sat}}$. As suggested by Equation 1.1, the system must be *supersaturated* (i.e. $S > 1$ and therefore $\Delta\mu > 0$), not just saturated, for nucleation to be possible.

For the nucleation of a fluid from a fluid (e.g. bubble or droplet nucleation), the surface energy γ is equivalent to the surface tension of that interface. For the nucleation of a solid precipitate from solution, γ is the interfacial free energy. It should be noted that γ is traditionally defined as the bulk surface energy. However, since there is no reason to expect a nano-scale cluster has the same interfacial properties as a macroscopically flat surface, γ is commonly treated as an effective parameter.

The non-monotonic shape of the nucleation free energy $F_{\text{CNT}}(n)$ suggests differing behavior for nuclei of different sizes. Small nuclei tend to dissolve because of the surface penalty for growth, but large nuclei tend to grow because the bulk driving force dominates. The critical nucleus size $n^{\ddagger}$ that separates these two distinct behaviors is the size that maximizes $F_{\text{CNT}}(n)$ in Equation 1.1 (i.e. size where $\partial F_{\text{CNT}}/\partial n = 0$):

$$n^{\ddagger} = \left(\frac{2\gamma a}{3\Delta\mu}\right)^3. \tag{1.5}$$

The maximum free energy $F^{\ddagger}_{\text{CNT}} = F_{\text{CNT}}(n^{\ddagger})$ is

$$F^{\ddagger}_{\text{CNT}} = \frac{4(\gamma a\phi)^3}{27\Delta\mu^2}. \tag{1.6}$$

$F_{\text{CNT}}(n)$ also tells us the relative abundance of nuclei of different sizes. The equilibrium populations $\rho_{eq}(n)$ of nuclei of size n relative to the population ρ_1 of monomeric

building units (i.e. $n = 1$) follows a Boltzman distribution:

$$\begin{aligned} \frac{\rho_{eq}(n)}{\rho_1} &= \exp\left[-\beta F_{\mathrm{CNT}}(n) + \beta F_{\mathrm{CNT}}(1)\right] \\ &= \exp\left[-\beta \Delta F_{\mathrm{CNT}}(n)\right], \end{aligned} \tag{1.7}$$

where $1/\beta = k_B T$ is the thermal energy at a temperature T and $\Delta F_{\mathrm{CNT}}(n) \equiv F_{\mathrm{CNT}}(n) - F_{\mathrm{CNT}}(1)$.

Heterogeneous nucleation (HEN)

In practice, nucleation is generally not in a clean environment, and the presence of a foreign substrate or surface can reduce the free energy of nucleation. The nucleation on a nucleation site on the surface is known as heterogeneous nucleation (HEN). CNT takes a similar thermodynamic approach for HEN (see Figure 1.3):

$$F_{\mathrm{CNT}}(n) = -n\Delta\mu + \gamma_{\mathrm{np}} a \phi v_{\mathrm{HEN}}^{1/3}(\theta) n^{2/3}, \tag{1.8}$$

where the first and second term is still the favorable bulk and unfavorable surface terms respectively. A key difference in the free energy expression is the factor v_{HEN} which is the ratio of the volume of the heterogeneous nucleus relative to that of a sphere of the same curvature (see Figure 1.3). For a spherical-cap-shaped nucleus growing on a flat substrate,

$$v_{\mathrm{HEN}}(\theta) = \frac{1}{4}(2 + \cos\theta)(1 - \cos\theta)^2. \tag{1.9}$$

where θ is the contact angle between the tangent of the spherical cap and the surface. θ can be estimated using Young's equation which sets the net force along each of the

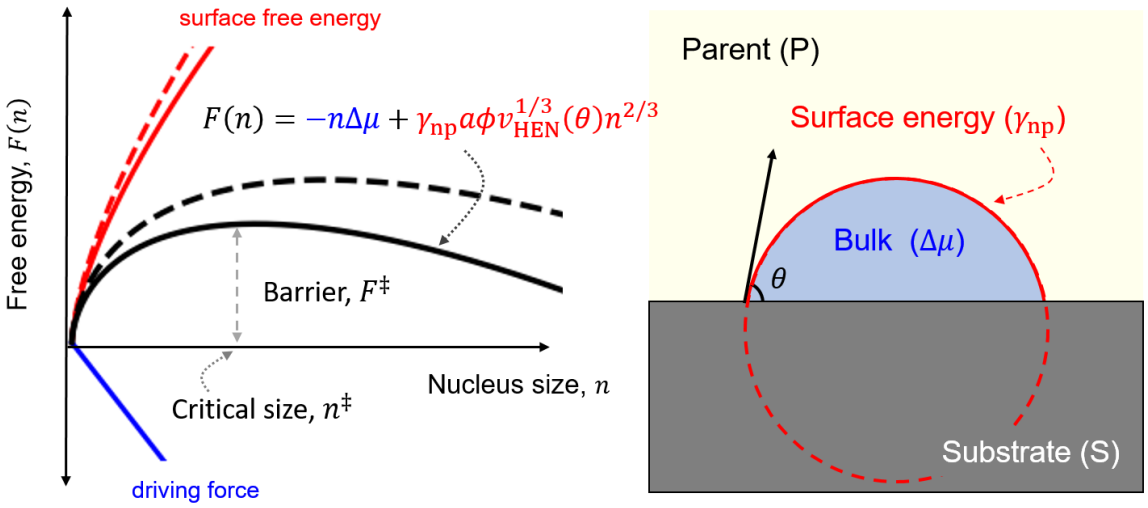

Figure 1.3: Diagram of classical nucleation theory free energy model for heterogeneous nucleation and the two competing contributions: unfavorable surface free energy and favorable driving force. The dotted curves are the corresponding homogeneous nucleation curves.

interface to zero at equilibrium:

$$\cos\theta = (\gamma_{sp} - \gamma_{sn})/\gamma_{np} \tag{1.10}$$

where γ_{sp}, γ_{sn}, and γ_{np} are the surface energies of the substrate-parent, substrate-nucleus, and nucleus-parent interfaces respectively. Other models for v_{HEN} are necessary for other surface geometries (e.g. pores and rough surfaces).

Equation 1.8 and Figure 1.3 clearly show that the free energy barrier for HEN is *always* lower than HON. This is because v_{HEN} acts as a scaling factor that reduces the surface penalty and therefore decreases both the barrier and critical nucleus size:

$$n^{\ddagger}_{HEN} = v_{HEN} n^{\ddagger}_{HON} \tag{1.11a}$$

$$F^{\ddagger}_{HEN} = v_{HEN} F^{\ddagger}_{HON}. \tag{1.11b}$$

Since $0 \geq v_{\mathrm{HEN}} \geq 1$, a substrate can only promote nucleation,[3] and nucleation behavior is often sensitive to the amount and morphology of solid impurities or surfaces.

1.2.2 Kinetics of nucleation

In Section 1.2.1, we discussed the thermodynamics of cluster formation, the equilibrium concentration of nuclei of size n relative to the concentration of monomers ($n = 1$), and identified the critical nucleus size $n^{\ddagger}$ and its population. However, nucleation is a non-equilibrium process, and any model of nucleation rates requires some information about the dynamics. Volmer and Weber proposed the first rate expression to account for this. They modeled the nucleation rate as the product of the equilibrium probability of forming a critical nucleus $\rho_{eq}(n^{\ddagger})/\rho_1 = \exp[-\beta \Delta F_{\mathrm{CNT}}(n^{\ddagger})]$ and the attachment rate (or rate clusters grow to a larger size).[10] In this section, we will briefly review the derivations of CNT rate equations and how the parameters can be connected to meaningful quantities.

Becker-Döring equation

Instead of directly using the equilibrium distribution like Volmer and Weber, Becker and Döring obtained the nucleation rate from the steady state distribution of cluster sizes.[11] Here, we will briefly outline this result. CNT assumes that molecules (or building units) attach and detach from a cluster one unit at a time, so the non-equilibrium steady state population $\rho(n)$ of clusters of each size n can be described by the following discrete master equation (see Figure 1.4):

$$\frac{d\rho(n)}{dt} = k_{n-1}\rho(n-1) - k_n^{(-)}\rho(n) + k_n\rho(n) + k_{n+1}^{(-)}\rho(n+1), \tag{1.12}$$

[3] This is true at least from a free energy perspective. The rate prefactor should also be considered for an accurate comparison.

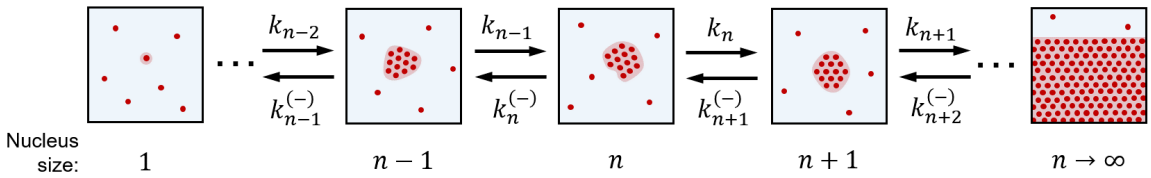

Figure 1.4: Diagram of Becker-Doring master equation. Building units (red) attach/detach to clusters (light red) one at a time.

where k_n is the rate to attach a building unit to the cluster of size n and $k_n^{(-)}$ is the rate to detach a building unit. It is important to note that an equilibrium cannot be reached in this model. As suggested by Equation 1.1 and 1.7, the free energy of a post-critical nucleus continues to decline and $\rho_{eq} \to \infty$ as $n \to \infty$. However, a steady state can be reached by including adsorb-and-replace boundary conditions:

$$\text{source (or replace)}: \ \xi(n) = 1 \qquad \text{for } n = 1 \tag{1.13a}$$

$$\text{sink (or adsorb)}: \ \xi(n) \to 0 \qquad \text{for } n \to \infty, \tag{1.13b}$$

where $\xi(n) \equiv \rho(n)/\rho_{eq}(n)$. The first boundary condition sets the number of monomers equal to the equilibrium population of monomers at that supersaturation. The second boundary condition ensures that the number of very large nuclei are vanishingly large because they are constantly removed when formed. At steady state (i.e. $d\rho/dt = 0$), the nucleation rate J (or net flux) is constant for all values of n and is

$$J = k_n \rho_{ss}(n) - k_{n+1}^{(-)} \rho_{ss}(n+1) = k_n \rho_{eq}(n) \left[\xi_{ss}(n) - \xi_{ss}(n+1)\right], \tag{1.14}$$

where ρ_{ss} is the population density at steady state and $\xi_{ss}(n) = \rho_{ss}(n)/\rho_{eq}(n)$. The second equality in Equation 1.14 is due to detailed balance (i.e. where the forward and reverse rates must be equivalent at equilibrium for all n, $k_n \rho_{eq}(n) = k_{n+1}^{(-)} \rho_{eq}(n+1)$).

Since

$$\sum_{n=1}^{\infty} \frac{J}{\rho_{eq}(n)k_n} = J\sum_{n=1}^{\infty} \frac{1}{\rho_{eq}(n)k_n} = \sum_{n=1}^{\infty} [\xi_{ss}(n) - \xi_{ss}(n+1)] = 1$$

due to arithmetic cancellations and the boundary conditions, the steady state nucleation rate is

$$J = \left[\sum_{n=1}^{\infty} \frac{1}{k_n \rho_{eq}(n)}\right]^{-1} \tag{1.15}$$

Although Equation 1.15 (also known as the Becker-Döring equation) does not explicitly mention a critical nucleus size, the dominate contribution to the summation is when $\rho_{eq}(n)$ is the smallest (i.e. when the size is near the critical nucleus size, $n \sim n^{\ddagger}$). This feature is consistent with Volmer and Weber's approach and reemphasizes that the rate primarily depends on the equilibrium population $\rho(n^{\ddagger})$ of critical nuclei and the attachment frequency $k_{n^{\ddagger}}$ onto critical nuclei.

CNT rate law from Zeldovich-Frenkel equation

The more commonly used CNT rate expression

$$J = A \exp\left[-\frac{B}{\ln^2 S}\right], \tag{1.16}$$

where A and B are constants, comes from a continuous (instead of discrete) representation of nucleus size. Equation 1.12 is a "one-step" type master equation (where transitions only exist between neighboring states) and can be converted into a corresponding Smoluchowski equation:

$$\frac{\partial \rho(n,t)}{\partial t} = \frac{\partial}{\partial n}\left\{\mathcal{D}(n)\rho_{eq}(n)\frac{\partial}{\partial n}\left[\frac{\rho(n,t)}{\rho_{eq}(n)}\right]\right\}, \tag{1.17}$$

where $\mathcal{D}(n)$ is the diffusion coefficient along the n-coordinate. At steady state, Equation 1.17 simplifies to

$$0 = \frac{d}{dn}\left\{\mathcal{D}(n)\rho_{eq}(n)\frac{d\xi_{ss}}{dn}\right\} = \frac{d\mathcal{D}}{dn}\left\{\rho_{eq}(n)\frac{d\xi_{ss}}{dn}\right\} + \mathcal{D}(n)\frac{d}{dn}\left\{\rho_{eq}(n)\frac{d\xi_{ss}}{dn}\right\}. \tag{1.18}$$

If we assume that $\mathcal{D}$ varies slowly (i.e. $d\mathcal{D}/dn$ is small), we can neglect the first term of the second equality. We can can approximate the solution $\xi_{ss}(n)$ by approximating the nucleation free energy as a harmonic barrier top:

$$\begin{aligned}\beta F_{\mathrm{CNT}}(n^\ddagger + \delta n) \quad &\approx \beta F_{\mathrm{CNT}}(n^\ddagger) + \frac{1}{2}\frac{d^2(\beta F_{\mathrm{CNT}})}{dn^2}\bigg|_{n=n^\ddagger}\delta n^2 \\ &\approx \beta F_{\mathrm{CNT}}(n^\ddagger) - \pi Z^2 \delta n^2 \end{aligned} \tag{1.19}$$

where $Z = \sqrt{\beta F''_{\mathrm{CNT}}(n^\ddagger)/2\pi}$ is the Zeldovich factor and imposing the adsorb-and-replace boundary conditions far from the critical nucleus size:

$$\text{source (or replace)}: \ \xi_{ss}(n^\ddagger + \delta n) \to 1 \qquad \text{for } \delta n \to -\infty \tag{1.20a}$$

$$\text{sink (or adsorb)}: \ \xi_{ss}(n^\ddagger + \delta n) \to 0 \qquad \text{for } \delta n \to \infty. \tag{1.20b}$$

After substituting Equation 1.19, $\rho_{eq}(n)/\rho_1 = \exp\left[-\beta \Delta F_{\mathrm{CNT}}(n)\right]$, and $n = n^\ddagger + \delta n$ into Equation 1.18, the solution $\xi_{ss}(n)$ that matches the boundary conditions is

$$\xi_{ss}(n) = \frac{1}{2}\mathrm{erfc}\left[Z\sqrt{\pi}(n - n^\ddagger)\right]. \tag{1.21}$$

Therefore, the steady state rate is

$$J = -\mathcal{D}(n^\ddagger)\frac{d\rho_{ss}}{dn}\bigg|_{n=n^\ddagger}. \tag{1.22}$$

Since $\xi'_{ss}(n^\ddagger) = -\xi'_{ss}(n^\ddagger)\rho'_{eq}(n^\ddagger) + \rho'_{ss}(n^\ddagger)/\rho_{eq}(n^\ddagger)$ and $\xi'_{ss}(n^\ddagger) = 0$,

$$\begin{aligned} J &= -\mathcal{D}(n^\ddagger)\frac{d\xi_{ss}}{dn}\bigg|_{n=n^\ddagger}\rho_{eq}(n^\ddagger) \\ &= \mathcal{D}(n^\ddagger)Z\rho_1 \exp\left[-\beta\Delta F_{\mathrm{CNT}}(n^\ddagger)\right] \\ &= \rho_1\mathcal{D}(n^\ddagger)Z\exp\left[F_{\mathrm{CNT}}(1)\right]\exp\left[-\beta F^\ddagger_{\mathrm{CNT}}\right]. \end{aligned} \tag{1.23}$$

After comparing the second equality with Equation 1.16, we can see that coefficients A and B are

$$A = \rho_1\mathcal{D}(n^\ddagger)Z\exp\left[F_{\mathrm{CNT}}(1)\right] \tag{1.24a}$$

$$B = \beta F^\ddagger_{\mathrm{CNT}} \quad \text{when } S = e. \tag{1.24b}$$

Once again, we see that the nucleation rate can be predicted by the equilibrium probability to form critical nuclei and the dynamics at the barrier top.

The huge benefit we get from Equation 1.16 and 1.24a and b is the ability to relate rate predictions to physically meaningful variables. For example, we can inspect how CNT rate parameters depend on the supersaturation S. Remember, B has no S dependence because the S-dependence of $F^\ddagger_{\mathrm{CNT}}$ is factored out (i.e. $F^\ddagger_{\mathrm{CNT}} = B/\ln^2 S$), but the prefactor A does depend on S. The concentration of monomers ρ_1 is proportional to S. If we use the CNT free energy model (Equation 1.1), Z is proportional to $\ln^2 S$, $\exp\left[F_{\mathrm{CNT}}(1)\right]$ is approximately proportional to $1/S$, and the radius of critical nuclei $R_\ddagger$ is proportional to $(n^\ddagger)^{1/3}$ and therefore $1/\ln S$. The S-dependence of $\mathcal{D}(n^\ddagger)$ depends on the rate of monomers attachment to clusters. Monomer attachment generally follows two sequential steps: (1) diffusion to the nucleus surface and (2) incorporation into the nucleus. Therefore, the upper bound on the rate is when the process is diffusion-limited and incorporation is very fast. However, the incorporation into the nucleus could be a

drastically slower activated process (e.g. slow desolvation or slow reaction). In that case, the attachment frequency is addition-limited. For a spherical nucleus,

$$\text{diffusion limited}: \quad \mathcal{D}(n^\ddagger) = 4\pi R_\ddagger^2 \left[D\rho_1 / R_\ddagger\right] \tag{1.25a}$$

$$\text{activated addition limited}: \quad \mathcal{D}(n^\ddagger) = 4\pi R_\ddagger^2 \left[k_s \rho_1\right], \tag{1.25b}$$

where D is the diffusion coefficient of the monomer and k_s is the incorporation rate. Therefore,

$$\text{diffusion limited}: \quad A = 4\pi R_\ddagger D \rho_1^2 Z \left[F_{\mathrm{CNT}}(1)\right] \propto S \ln S \tag{1.26a}$$

$$\text{activated addition limited}: \quad A = 4\pi R_\ddagger^2 k_s \rho_1^2 Z \left[F_{\mathrm{CNT}}(1)\right] \propto S. \tag{1.26b}$$

In Equation 1.16, it is important to note that the exponential term has a much stronger supersaturation dependence than the prefactor, so the prefactor is often treated as a constant.

Summary

In Section 1.2.2, we have briefly reviewed classical nucleation theory (CNT) and its derivation of the nucleation free energy F_{CNT} and nucleation rate J. Rate predictions using Equation 1.15 or 1.23 do not explicitly require the use of the CNT free energy model. However, when we do use either Equation 1.1 or 1.8, we obtain a beautiful and simple theoretical framework that allows us to predict kinetic trends from physically meaningful parameters, including supersaturation, surface energy, and diffusion constants. Many experimental and computational studies have verified the predicted approximately linear relationship[4] between $\ln J$ and $1/\ln^2 S$.[12–20]

[4] $\ln J \propto 1/\ln^2 S$ if we neglect the prefactor's much weaker S-dependence.

1.3 Corollary theories of classical nucleation theory

Even though CNT absolute rate predictions are notoriously inaccurate when bulk parameters are used, CNT remains the primary theory used to understand and interpret nucleation. Unlike purely empirical models, CNT offers a theoretical framework to interpret kinetic trends, estimate relevant and physically meaningful parameters, and infer mechanisms using nucleation rate data. However, CNT makes a number of assumptions that might be responsible for its poor predictions in specific cases. To obtain F_{CNT} for homogeneous nucleation using Equation 1.1, CNT assumes that:

1. Nuclei and the metastable parent phase are separated by a sharp interface defined by the Gibbs dividing surface. This allows the assumption that the excess free energy $F_{\mathrm{ex}}(n) \equiv F_{\mathrm{CNT}}(n) - n\Delta\mu$ scales with area (i.e $F_{\mathrm{ex}}(n) = \gamma a \phi n^{2/3}$). Other factors that could affect the excess free energy are neglected. For example in solid-solid nucleation, long-range strain effects due to a lattice mismatch between the nucleating and parent phases may not scale with the nucleus surface area.

2. The nucleating phase has a size-independent bulk chemical potential $\Delta\mu$ and surface tension γ. Both are often assumed to be their macroscopic quantities, but effective properties can also be used for γ if the interfacial properties of small nuclei differ from that of a macroscopic flat interface.

To obtain J using Equation 1.23, CNT assumes that:

1. The primary dynamic variable of interest (i.e. the reaction coordinate) is nucleus size n. The dynamics of all other variables thermalize much faster than that of n, so nucleation can be modeled as a "one-dimensional" process along the n-coordinate.

2. The growth/dissolution of nuclei is only due to the attachment/detachment of monomeric growth units. CNT does not account for aggregation.

3. Nucleation is an activated one-step process. This means that no stable intermediate phases are formed during the transition from the metastable phase to the stable nucleating phase.

4. The barrier is sufficiently high. This assumption improves the accuracy of the quadratic approximation of the barrier top and allows us to approximate the rate using only the equilibrium and dynamical properties of near critical nuclei. Therefore, Equation 1.23 is generally more suitable for modeling nucleation at moderate supersaturations.

5. The process is in steady state, so supersaturation remains constant. If supersaturation changes in time, the quasi-steady rate predictions are only appropriate if the cluster distribution of the metastable state re-equilibrates much faster than the rate supersaturation changes.

We can generate corollary theories that invoke *some* elements of CNT but relaxes an assumption and/or relates CNT parameters (e.g. driving force or surface energy) to other factors. An example of a corollary theory is δ-CNT, where the surface energy in the CNT free energy and rate law now includes a cluster size correction. CNT assumes that the surface energy (or surface tension) is constant and equivalent to that of the macroscopic flat interface. However, it is questionable to expect nanometer-sized nuclei composed of fewer than hundreds of solute molecule to have the same interfacial properties as a macroscopic flat surface.[12,21,22] A common thermodynamic size-dependent correction to the surface energy is the Tolman equation:[23]

$$\gamma(R) = \gamma\left[1 - \frac{2\delta}{R} + \cdots\right], \tag{1.27}$$

where δ is the Tolman length (i.e. $\delta = R_e - R_s$, the difference between the radii defined

by the Gibbs dividing surface R_e and the surface of tension R_s). δ can be positive or negative, depending on where the dividing surfaces are located, so the surface energy can either increase or decrease with increasing size. Joswiak et al. showed that CNT can accurately predict experimental water droplet nucleation rates *if* the Tolman correction is included.[24,25] Without the correction, CNT-predicted and experimentally-measured rates differ by several orders of magnitude because the planar surface tension used in CNT underestimates the surface tension of nano-scale droplets.

In the following chapters, we develop several extensions of CNT. Chapter 2 addresses a situation where the creation of localized enrichment enhances nucleation. We study how the macroscopic concentration boundary layer that develops during freeze-concentration localizes and accelerates nucleation of a dissolved solute. We relate the growth velocity to the distribution of nucleation times. Chapter 4 and 5 address situations when adsorbing additives lower the surface energy and therefore accelerates nucleation. In Chapter 4, we develop a theoretical framework to understand how dilute molecular surfactants can promote nucleation. We combine CNT free energy expressions and rate laws with Langmuir adsorption theory to relate nucleation rates to surfactant binding strength and concentration. We also show that our theory is consistent with our lattice simulations. In Chapter 5, we study the how oligomeric additives promote nucleation. We use lattice simulations to show that the rate is very sensitive to chain length and binding strength. We also show that oligomers can sometimes be more much more effective promoters than their monomeric counterpoint.

1.4 Summary

Nucleation is notoriously difficult to directly observe experimentally; however, contributions from theory and simulations have provided more context for experimental

measurements. Classical nucleation theory (CNT), in particular, provides a simple yet intuitive framework to relate nucleation rates to physically meaningful thermodynamic and kinetic properties (e.g. supersaturation, interfacial energy, and attachment rate) and understand trends.[26] CNT makes several assumptions about these properties. For example, it assumes that the shape, surface energy, and bulk chemical potential of nuclei remains the same as it grows. However, these assumptions can be relaxed by modifying those parameters in CNT. Corollary theories that borrow many elements of CNT can predict other kinetic and thermodynamics trends by relating CNT parameters to other variables that do not explicitly appear in CNT. This allows us to understand nucleation in situations where the original formulations of CNT are not applicable.

Bibliography

[1] P. G. Debenedetti, *Metastable liquids: concepts and principles*. Princeton University Press, 1996.

[2] D. W. Oxtoby, *Nucleation of first-order phase transitions*, *Accounts of Chemical Research* **31** (1998), no. 2 91–97, [http://dx.doi.org/10.1021/ar9702278].

[3] D. F. Chao and M. M. Hasan, *Nucleate boiling heat transfer studied under reduced-gravity conditions*, .

[4] T. Bartels-Rausch, *Chemistry: Ten things we need to know about ice and snow*, *Nature* **494** (2013), no. 7435 27–29.

[5] B. J. Murray, T. W. Wilson, S. Dobbie, Z. Cui, S. M. Al-Jumur, O. Möhler, M. Schnaiter, R. Wagner, S. Benz, M. Niemand, *et. al.*, *Heterogeneous nucleation of ice particles on glassy aerosols under cirrus conditions*, *Nature Geoscience* **3** (2010), no. 4 233–237.

[6] A. Lintunen, T. Hölttä, and M. Kulmala, *Anatomical regulation of ice nucleation and cavitation helps trees to survive freezing and drought stress*, *Scientific reports* **3** (2013).

[7] P. Mazur, *Cryobiology: the freezing of biological systems*, *Science* **168** (1970), no. 3934 939–949.

[8] J. Bernstein, *Cultivating crystal forms*, *Chemical Communications* (2005), no. 40 5007–5012.

[9] A. K. Sum, C. A. Koh, and E. D. Sloan, *Clathrate hydrates: From laboratory science to engineering practice*, *Ind. Eng. Chem. Res.* **48** (2009), no. 16 7457–7465.

[10] M. Volmer and A. Weber, *Nuclei formation in supersaturated states*, *Z. Phys. Chem.* **119** (1926) 277–301.

[11] R. Becker and W. Doring, *Kinetic treatment of grain-formation in super-saturated vapours*, *Annalen der Physik* **24** (1935), no. 8 719–752.

[12] D. Kashchiev, *Nucleation: Basic Theory With Applications*. Butterworth-Heinemann, Oxford, 2000.

[13] D. Kashchiev and G. M. van Rosmalen, *Review: Nucleation in solutions revisited*, *Cryst. Res. Technol.* **38** (2003), no. 7-8 555–574.

[14] D. Kashchiev and A. Firoozabadi, *Nucleation of gas hydrates*, *J. Cryst. Growth* **243** (2002), no. 3-4 476–489.

[15] A. E. Nielsen, *Homogeneous nucleation in barium sulfate precipitation*, *Acta Chem. Scand.* **15** (1961), no. 2 441–&.

[16] A. E. Nielsen, *Nucleation in aqueous solution*, *J. Phys. Chem. Solids* **S** (1967) 419–&.

[17] K. F. Kelton, A. L. Greer, and C. V. Thompson, *Transient nucleation in condensed systems*, *J. Chem. Phys.* **79** (1983), no. 12 6261–6276.

[18] R. J. Davey, S. L. M. Schroeder, and J. H. ter Horst, *Nucleation of organic crystalsa molecular perspective*, *Angew. Chem. Int. Ed.* **52** (2013), no. 8 2166–2179.

[19] M. Horsch, J. Vrabec, and H. Hasse, *Modification of the classical nucleation theory based on molecular simulation data for surface tension, critical nucleus size, and nucleation rate*, *Physical Review E* **78** (2008), no. 1 011603.

[20] J. Wölk and R. Strey, *Homogeneous nucleation of h2o and d2o in comparison: the isotope effect*, *The Journal of Physical Chemistry B* **105** (2001), no. 47 11683–11701.

[21] V. Agarwal and B. Peters, *Precipitate Nucleation: A Review of Theory and Simulation Advances*, vol. 155 of *Advances in Chemical Physics*. John Wiley & Sons, New Jersey, USA, 2014.

[22] K. Kelton and A. L. Greer, *Nucleation in condensed matter: applications in materials and biology*, vol. 15. Elsevier, 2010.

[23] R. C. Tolman, *The effect of droplet size on surface tension*, *The journal of chemical physics* **17** (1949), no. 3 333–337.

[24] M. N. Joswiak, N. Duff, M. F. Doherty, and B. Peters, *Size-dependent surface free energy and tolman-corrected droplet nucleation of tip4p/2005 water*, *The journal of physical chemistry letters* **4** (2013), no. 24 4267–4272.

[25] M. N. Joswiak, R. Do, M. F. Doherty, and B. Peters, *Energetic and entropic components of the tolman length for mw and tip4p/2005 water nanodroplets*, *The Journal of chemical physics* **145** (2016), no. 20 204703.

[26] B. Peters, *Common features of extraordinary rate theories*, *The Journal of Physical Chemistry B* **119** (2015), no. 21 6349–6356.

Chapter 2

Accelerated solute nucleation during freeze-concentration

2.1 Background

Freeze-concentration refers to phenomena in which a crystallizing solvent excludes and thereby concentrates a solute near the solidification front (see Fig. 2.1). This is because the solubility of the solute in the solid phase is substantially less than that in the liquid phase. The solute that is not incorporated into the solid phase is displaced during crystallization, leaving behind a more concentrated solution.

Freeze-concentration is important in atmospheric chemistry,[1] zone refining,[2–4] fruit juice concentration,[5] protein crystallization,[6] amorphous calcium carbonate nucleation,[7] and perhaps in the formation of Liesegang precipitation rings.[8] In many of these processes, the localized enrichment of solute due to solvent crystallization (often ice formation in aqueous solutions) induces the nucleation of a dissolved solute. This chapter

Reproduced in part with permission from Poon, G. G., and Peters, B. (2013). "A stochastic model for nucleation in the boundary layer during solvent freeze-concentration." Crystal Growth and Design, 13(11), 4642-4647. Copyright 2013 American Chemical Society

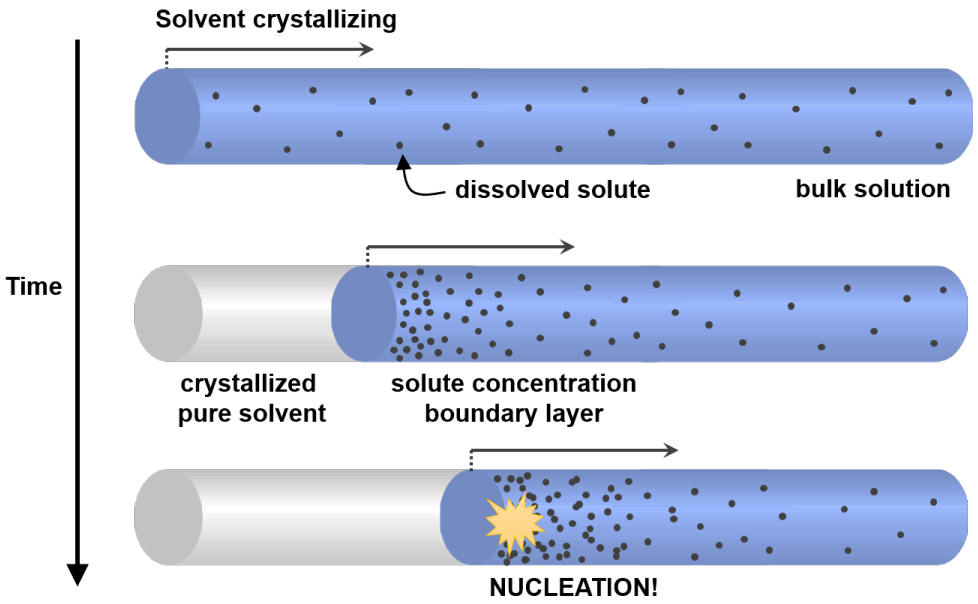

Figure 2.1: A schematic of freeze-concentration. The dissolved solute is excluded from the pure crystallizing solvent and accumulates ahead of the freeze-front, forming a concentration boundary layer. Eventually, the highly enriched boundary layer can induce nucleation.

discusses the interplay between spatiotemporal solute concentration profiles and nucleation kinetics, which depend strongly on the solute concentration.[9]

Pohl[10] and Tiller et al.[3,4] showed that a localized boundary layer of high-solute concentration forms ahead of the growing ice front. This feature makes freeze-concentration an intriguing way to control the conditions and location where nucleation occurs. For example, when the bulk solution is saturated (not supersaturated), then solute nucleation can only occur at or very near the ice surface at the freezing temperature. By contrast, nucleation in many other environments is a messy affair. For example, it is difficult to be certain whether nucleation is homogeneous (spontaneous organization of solutes in solution) or heterogeneous (catalyzed by some dust particle or defect in the glassware). Such difficulties in the mechanistic interpretation impede the development of accurate nucleation theories. Freeze-concentration allows nucleation sites away from the ice growth front to be excluded from consideration.

Previous investigators have noted that nucleation of gas bubbles in the moving ice front leaves a record of nucleation events as bubbles trapped in ice.[11–13] As the ice grows, the solute accumulates in a thin boundary layer ahead of the ice front until a nucleus forms. The nucleus grows creating a bubble near the advancing ice. Eventually, the bubble depletes the local supersaturation and is engulfed by the ice. The cycle continues as the ice continues to grow and solute accumulates near the front again. Although nucleation is a stochastic process, previous investigators have exclusively used deterministic models to understand the spacing and size of entrapped bubbles.[11,12]

This chapter presents a dimensionless stochastic model for nucleation within the concentrated solute boundary layer formed by the moving front. We make several simplifying assumptions. First, we only consider the case where solute is completely rejected from the ice. Complete rejection is realistic when nucleation occurs at solute concentrations much lower than those required to force solute inclusions into the ice. However, our general framework is still valid when there is some finite solute incorporation in the ice if the concentration profile is adjusted accordingly. Note that Smith et al. found the concentration profile when the solute has a constant partition coefficient at the interface.[4] Second, we assume vertical ice growth in a perfectly quiescent environment with no convection. Note that even without forced convection, buoyancy driven flows can result from density differences between the concentrated boundary layer and the bulk solution.[14] Third, we ignore freezing point depression and the possible consequences of cellular/dendritic growth. Therefore, the analysis here is quantitatively accurate only for nucleation of sparingly soluble solutes.[15] Fourth, we assume that diffusion is slower than conduction (i.e., that the thermal boundary layer is thicker than the concentration boundary layer). This fourth assumption is typically true for liquid solutions.[16] Combining the third and fourth assumptions implies that the entire concentration boundary layer is isothermal and at the solvent freezing temperature.

2.2 Stochastic survival probability model

2.2.1 One dimensional temporal concentration profile

Nucleation rates are strongly dependent on the concentration of solute, so it is necessary to develop a model of how the concentration varies in both time and space. Here, we consider the simplest model of freeze-concentration, where solute is displaced in one direction (i.e. the outer normal direction of the solidification front). If the planar solidification front moves at a constant growth velocity g, the spatiotemporal concentration profile $c(x,t)$ is the solution to

$$\frac{\partial c}{\partial t} = D\frac{\partial^2 c}{\partial x^2} + g\frac{\partial c}{\partial x} \tag{2.1}$$

where D is the solute diffusion coefficient and x is position relative to (or ahead of) the solidification front (see Figure 2.2a). We restrict our study to a semi-infinite reservoir that is initially saturated (i.e. $c_\infty = c_{\text{sat}}$) with a solute that is insoluble in the crystallizing solid (i.e. no flux boundary condition at the solidification front). This results in the following initial and boundary conditions:

$$\text{Initial condition}: \quad c(x,0) = c_\infty \tag{2.2a}$$

$$\text{Boundary condition 1}: \quad \lim_{x\to\infty} c(x,t) = c_\infty \tag{2.2b}$$

$$\text{Boundary condition 2}: \quad gc(0,t) + D\frac{\partial c}{\partial x}(0,t) = 0 \tag{2.2c}$$

Equation 2.1 can be non-dimensionalized to yield

$$\frac{\partial \Delta}{\partial \tau} = \frac{\partial^2 \Delta}{\partial z^2} + \frac{\partial \Delta}{\partial z} \tag{2.3}$$

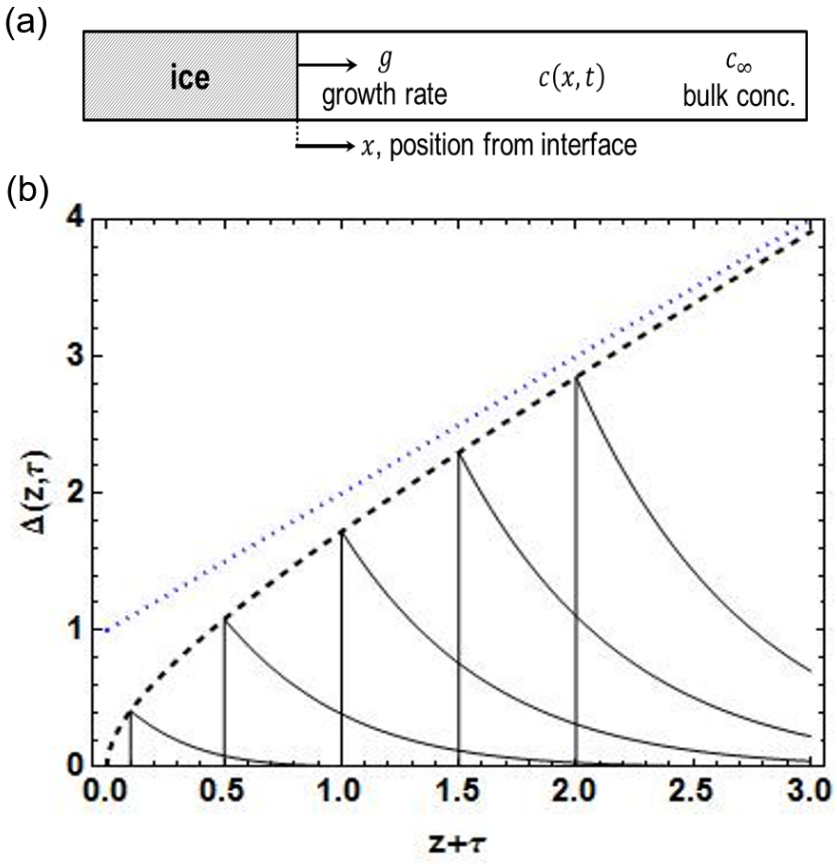

Figure 2.2: The interfacial supersaturation $\Delta(0,\tau)$ (dashed curve) and its large time limit $\Delta(0,\tau\to\infty)=1+\tau$ (dashed curve). Several supersaturations profiles $\Delta(zm\tau)$ (solid curves) at different times.

where $\Delta(z,\tau) \equiv (c - c_\infty)/c_\infty$ is the dimensionless concentration enrichment, $\tau \equiv tg^2/D$ is the dimensionless time, and $z \equiv xg/D$ is the dimensionless position. The initial conditions and boundary conditions are then

$$\text{Initial condition}: \ \Delta(z,0) = 0 \tag{2.4a}$$

$$\text{Boundary condition 1}: \ \lim_{z\to\infty} \Delta(z,\tau) = 0 \tag{2.4b}$$

$$\text{Boundary condition 2}: \ \Delta(0,t) + \frac{\partial \Delta}{\partial z}(0,t) = -1 \tag{2.4c}$$

Fedorchenko et al. showed how to obtain the exact solution to Equation 2.3.[17] If we define a dummy variable $\Delta^*(z,\tau) \equiv \Delta(z,\tau)e^{\tau/4+z/2}$, we can eliminate the convection term in Equation 2.3:

$$\frac{\partial \Delta^*}{\partial \tau} = \frac{\partial^2 \Delta^*}{\partial z^2} \tag{2.5}$$

with the following initial conditions and boundary conditions:

$$\text{Initial condition}: \ \Delta^*(z,0) = 0 \tag{2.6a}$$

$$\text{Boundary condition 1}: \ \lim_{z\to\infty} \Delta^*(z,\tau) = 0 \tag{2.6b}$$

$$\text{Boundary condition 2}: \ \frac{1}{2}\Delta^*(0,t) + \frac{\partial \Delta^*}{\partial z}(0,t) = -e^{\tau/4+z/2} \tag{2.6c}$$

Using Laplace transformations, we can show that the concentration profile for $\tau > 0$ and $z \geq 0$ is

$$\Delta(z,\tau) = \sqrt{\frac{\tau}{\pi}} e^{(z+\tau)^2/4\tau} + \frac{1 - z + \tau}{2} e^{-z} \text{erfc}\left[\frac{z-\tau}{2\sqrt{\tau}}\right] - \frac{1}{2}\text{erfc}\left[\frac{z+\tau}{2\sqrt{\tau}}\right] \tag{2.7}$$

The local supersaturation $S(z,\tau)$, the solute concentration relative to the solubility limit,

is easily calculated from $\Delta(z,\tau)$:

$$S(z,\tau) = \frac{c_\infty}{c_{\text{sat}}}\left[1+\Delta(z,\tau)\right] = 1+\Delta(z,\tau) \tag{2.8}$$

Figure 2.2b shows how the concentration profile develops with time after the onset of ice growth. The growth rate of ice and the solute diffusivity determine the extent of supersaturation in the boundary layer and the boundary layer thickness. For all but extremely short times, the concentration boundary layer is approximately D/g thick. In this model, the interfacial concentration continually increases without bounds until nucleation occurs.

2.2.2 Poisson process with a spatial-temporal rate

The dimensionless induction time for the first nucleation event τ_i is a stochastic random variable that depends on the rate of nucleation J, which increases rapidly with supersaturation.[9,18] As mentioned in Section 1.2.2, classical nucleation theory (CNT) predicts that J is approximately

$$J = A\exp\left[-\frac{B}{\ln^2 S}\right] \tag{2.9}$$

where A is a prefactor, $B\ln^2 S = \Delta F^{\ddagger}_{CNT}/k_BT$ is the dimensionless free energy barrier, and $S = c/c_{sat}$ is the supersaturation.[9] Although CNT predictions of A and B are notoriously inaccurate, nucleation kinetics often do exhibit a linear relationship between $\ln \mathrm{J}$ vs. $1/\ln^2 S$.[9,18,19] Equation 2.9 has also been used in the analysis of metastable zone width (MZW) data.[20–22] Stochastic models of MZW data are based on the Poisson survival probability, i.e. the probability that nucleation has not yet occurred after waiting for a time t.[20,23] For homogeneous nucleation in an observation volume V and with a

time-variant supersaturation $S(t)$, the survival probability used in prior studies[20,23] is

$$P(t) = \exp\left[-\int_0^t dt' \; J(t')V\right] \tag{2.10}$$

where $J(t)$ is the time-variant homogeneous nucleation rate.[20,21,24] Note that Equation 2.10 assumes a spatially uniform supersaturation, so it is not valid for nucleation during solvent freeze-concentration.

For homogeneous nucleation (HON), the appropriate stochastic survival probability model should consider the probability of nucleation anywhere in the solution volume ahead of the ice growth front. However, the HON rate J_{HON} vanishes at points far from the ice growth front when $c_\infty/c_{\mathrm{sat}} = 1$, and this is the special case that we model. The probability that nucleation has not happened in the semi-infinite volume ahead of the moving front up to time t is

$$P_{\mathrm{HON}}(t) = \exp\left[-a\int_0^t dt' \int_0^\infty dx \; J_{\mathrm{HON}}(x,t')\right] \tag{2.11}$$

where $J_{\mathrm{HON}}(x,t) = A_{\mathrm{HON}} \exp[-B_{\mathrm{HON}}/\ln^2 S(x,t)]$ is the local HON rate from Equation 2.9, a is the area of the planar interface, and the units of A_{HON} is nuclei per volume per time. We non-dimensionalize Equation 2.11 by introducing the Damkohler number $Da_{\mathrm{HON}} \equiv (aA_{\mathrm{HON}}D^2)/g^3$ and our previously defined dimensionless variables:

$$P_{\mathrm{HON}}(\tau) = \exp\left[-Da_{\mathrm{HON}}\int_0^\tau d\tau' \int_0^\infty dz \; \exp\left(-\frac{B_{\mathrm{HON}}}{\ln^2 S(z,\tau')}\right)\right] \tag{2.12}$$

$P_{\mathrm{HON}}(\tau)$ resembles an inverse sigmoidal curve (see Figure 2.3). $P_{\mathrm{HON}}(\tau) = 1$ for small times and then rather suddenly drops to 0 as $S(0,\tau)$ crosses through the metastable zone.

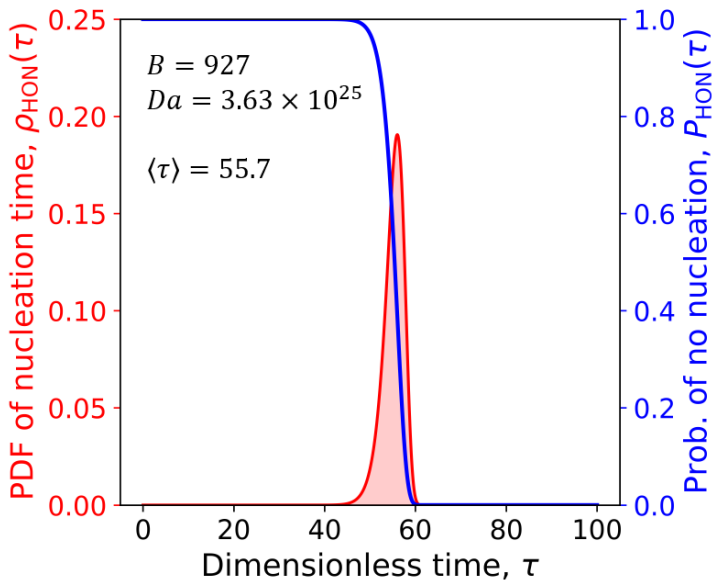

Figure 2.3: The probability distribution function (PDF) of nucleation time and probability of no nucleation as a function of time for the nucleation of methane hydrate with an ice front advancing at a rate of $g = 1$ μm/s for an area $a = 1$ cm^2. Parameters B and Da determined using values obtained by simulations done by Knott et al. [25]

The probability distribution for the moment of first nucleation is

$$\rho_{\mathrm{HON}}(\tau) = -\frac{dP_{\mathrm{HON}}}{d\tau} \tag{2.13}$$

and is used to find the average dimensionless induction time $\langle \tau_{\mathrm{HON}} \rangle$ for the first HON event to occur.

$$\langle \tau_{\mathrm{HON}} \rangle = \int_0^\infty d\tau \ \tau \rho_{\mathrm{HON}}(\tau) = \int_0^\infty d\tau \ P_{\mathrm{HON}}(\tau) \tag{2.14}$$

The final expression in Equation 2.14 is obtained using integration by parts. Using Equations 2.7, 2.8, 2.12, and 2.14, we can predict the dependence of $\langle \tau_{\mathrm{HON}} \rangle$ on B_{HON} and Da_{HON}.

However, it is also useful to quantify how stochastic nucleation is, or the width of the distribution of nucleation times. We define a relative 90% confidence interval width for

HON in the boundary layer as

$$90\%RCIW_{\mathrm{HON}} = \frac{\tau_5 - \tau_{95}}{(\tau_5 + \tau_{95})/2} \tag{2.15}$$

where $P_{\mathrm{HON}}(\tau_5) = 0.05$ and $P_{\mathrm{HON}}(\tau_{95}) = 0.95$. When $90\%RCIW_{\mathrm{HON}}$ is small, the distribution of first nucleation times is narrow and nucleation can be treated as a deterministic event. Conversely, a large $90\%RCIW_{\mathrm{HON}}$ implies that the stochastic nature of nucleation cannot be ignored. Numerical results for $\langle \tau_{\mathrm{HON}} \rangle = \langle g^2 t_{\mathrm{HON}}/D \rangle$ and $90\%RCIW_{\mathrm{HON}}$ are shown in Figure 2.4a. Figure 2.4a reveals that nucleation is slower and more stochastic when Da_{HON} is small (i.e. ice growth rate is fast). As expected, induction times increase exponentially with B_{HON} (i.e. barrier height).

A similar survival probability analysis for HEN on the ice-water interface can provide average induction times and relative confidence interval widths for HEN, $\langle \tau_{\mathrm{HEN}} \rangle$ and $90\%RCIW_{\mathrm{HEN}}$. The rate of HEN at the interface depends only on the time-dependent interfacial supersaturation $S(0, \tau)$. A new Damkohler number for HEN $Da_{\mathrm{HEN}} \equiv aADg^2$ can be introduced to nondimensionalize the arguments of the survival probability. The probability of no heterogeneous nucleation up to a dimensionless time τ is

$$P_{\mathrm{HEN}}(\tau) = \exp\left[-Da_{\mathrm{HEN}} \int_0^{\tau} d\tau' \int_0^{\infty} dz \ \exp\left(-\frac{B_{\mathrm{HEN}}}{\ln^2 S(0, \tau')} \right) \right] \tag{2.16}$$

and the distribution width is

$$90\%RCIW_{\mathrm{HEN}} = \frac{\tau_5 - \tau_{95}}{(\tau_5 + \tau_{95})/2}. \tag{2.17}$$

Figure 2.4b shows that the distribution of nucleation times for HEN is qualitatively very similar to that of HON. For example, the average induction time is very sensitive to B, and the distribution width is very sensitive to the corresponding Da.

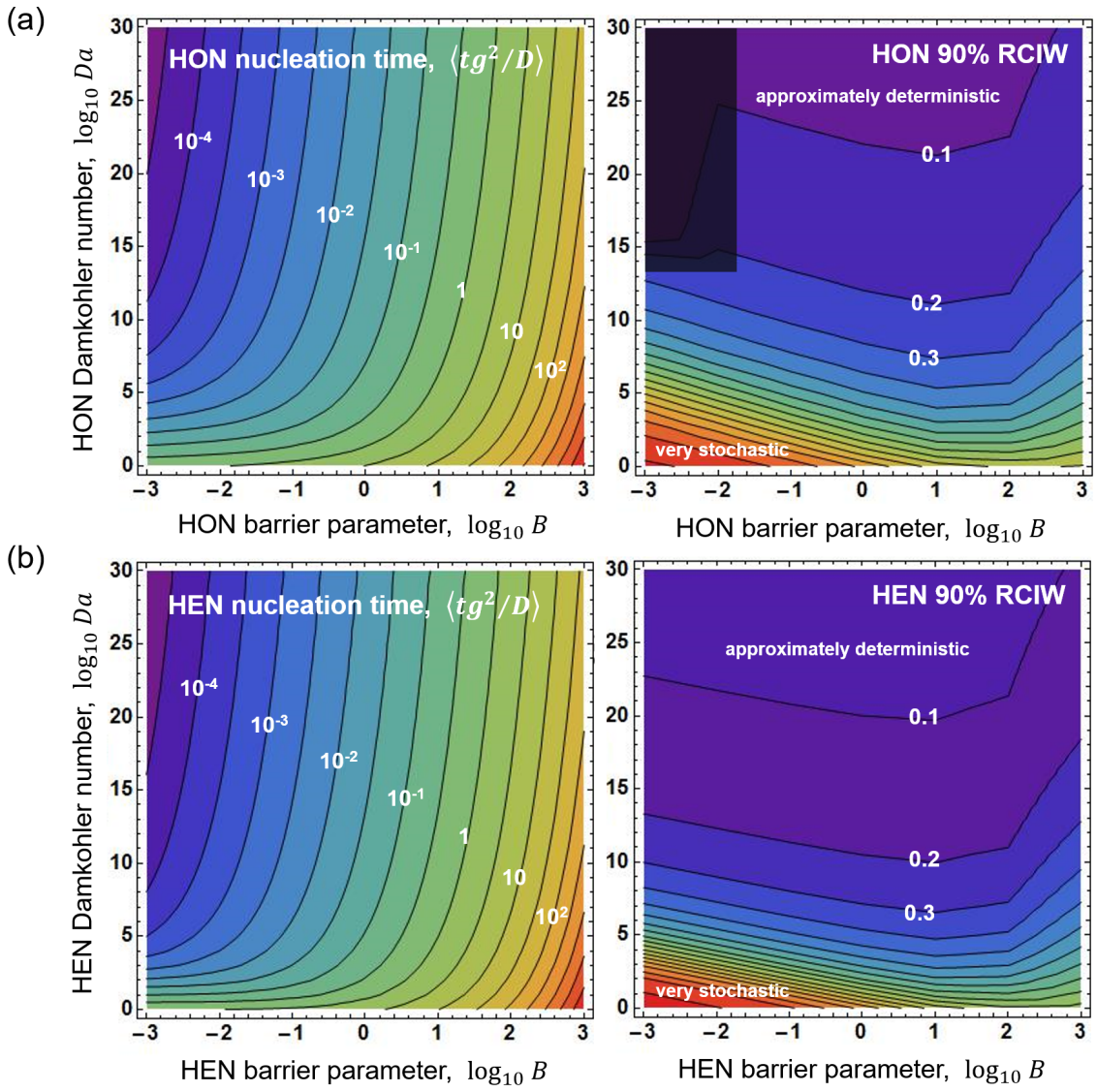

Figure 2.4: (a) (left) Contours of constant $\langle \tau_{\mathrm{HON}} \rangle$ as a function of $\log_{10} Da_{\mathrm{HON}}$ and $\log_{10} B_{\mathrm{HON}}$. (right) Contours of constant 90% $\mathrm{RCIW}_{\mathrm{HON}}$ as a function of $\log_{10} Da_{\mathrm{HON}}$ and $\log_{10} B_{\mathrm{HON}}$. The numerical accuracy in the yellow-black-striped region is questionable because of the precision of our numerical integration in Equation 2.12. (b) (left) Contours of constant $\langle \tau_{\mathrm{HEN}} \rangle$ as a function of $\log_{10} Da_{\mathrm{HEN}}$ and $\log_{10} B_{\mathrm{HEN}}$. (right) Contours of constant 90% $\mathrm{RCIW}_{\mathrm{HEN}}$ as a function of $\log_{10} Da_{\mathrm{HEN}}$ and $\log_{10} B_{\mathrm{HEN}}$.

If both HON and HEN can occur and if both $90\%RCIW$s are small, the nucleation mechanism with the lowest average induction time will tend to occur first.

2.2.3 Necessary constraints on time and length scales

The quasi-stationary rate laws in our stochastic models of nucleation require that the local supersaturation is approximately constant over the length scale of the nucleus. Specifically, the critical nucleus radius $R^{\ddagger}$ at the moment and location of nucleation should be much smaller than the characteristic length of the boundary layer (i.e. $R^{\ddagger} \ll Dg$). According to the classical nucleation theory (CNT), the critical size for a spherical nucleus in HON is

$$R^{\ddagger} = \frac{2v_0\gamma}{k_B T \ln S} \tag{2.18}$$

where v_0 is the volume per solute molecule in the nucleus, and γ is the interfacial free energy.[9,26] The nucleation barrier is

$$\frac{B_{HON}}{\ln^2 S} = \frac{F^{\ddagger}_{CNT}}{k_B T} = \frac{16\pi}{3v_0 \ln^2 S}\left(\frac{v0\gamma}{k_B T}\right)^3. \tag{2.19}$$

The first equality is the definition of the parameter B, and the second equality is from CNT. Equation 2.18 and 2.19 imply a relation that can be used to eliminate the difficult to ascertain parameter $r^{\ddagger}$ in favor of B_{HON}. Specifically, $r^{\ddagger}\ln S = (3Bv_0 2\pi)^(1/3)$ for HON with spherical nuclei. This gives us the requirement for validity for the quasi-spatially uniform approximation:

$$\left(\frac{l_0 g}{D}\right)\left(\frac{3B_{HON}}{2\pi}\right)^{1/3} \ll \ln S_0(\langle\tau_i\rangle), \tag{2.20}$$

where $l_0 = v_0^{1/3}$ is approximately the solute molecular diameter.

For a spherical cap nucleus in HEN, the cap height $h = R^{\ddagger}(1-\cos\theta)$ must be much

smaller than the boundary layer thickness D/g, where θ is the contact angle. Equation 2.20 is modified to

$$\left(\frac{l_0 g}{D}\right)(1-\cos\theta)\left(\frac{3B_{HON}}{2\pi v_{HEN}(\theta)}\right)^{1/3} \ll \ln S_0(\langle\tau_i\rangle), \tag{2.21}$$

where $v_{HEN}(\theta) = (2-3\cos\theta+\cos^3\theta)/4$. For a solute diffusivity of 10^{-9} m^2/s and an ice growth rate of 10^{-6} m/s, the boundary layer thickness $D/g = 1$ mm which is much greater than a typical nuclei size. This suggests that the spatially uniform approximation is valid in many cases.

Additionally, our model is only valid within the quasi-stationary regime, when the cluster size distribution relaxes to the new stationary distribution quickly relative to the rate at which supersaturation changes. Kashchiev [9,18,27] showed that this requirement is satisfied when

$$\left|\frac{d\ln S}{dt}\right| < \frac{16}{\pi n^{\ddagger}(t)\tau_{lag}(t)}, \tag{2.22}$$

where $n^{\ddagger}(t)$ is the critical nucleus size for a static system at the supersaturation at time t and $\tau_{lag}(t)$ is the lag time for the redistribution of nuclei size after the change in supersaturation at time t. Substituting CNT-predicted values for $n^{\ddagger}$ and τ_{lag}, the HON requirement for validity of the quasi-static approximation is

$$\left|\frac{d\ln^{-6} S_0(\tau)}{d\tau}\right| < \frac{\pi v_0 A_{HON} D}{6B_{HON}^2 g^2}. \tag{2.23}$$

Equation 2.23 and the equivalent HEN requirement must be satisfied for all times prior to the first nucleation event.

Table 2.1: Average induction times for methane hydrate nucleation with and without freeze-concentration.

	freeze-concentration	quiescent
initial supersaturation, $S(t=0)$	1	5.8
observation area or volume, a or V	1 cm^2	1 cm^3
ice growth velocity, g	1 μm/s	N/A
methane diffusivity, D	1.46×10^{-9} m^2/s	N/A
average induction time, $\langle\tau\rangle$	58 hours	10^{103} years

2.3 Implications for gas hydrate nucleation

To illustrate the impact of freeze concentration, consider the nucleation of natural gas hydrates. Methane hydrate nucleation from an aqueous solution of methane is fast in simulations at extremely high supersaturation.[28–32] However, at more realistic supersaturations, Knott et al. found that homogeneous hydrate nucleation from an aqueous solution is impossibly slow.[25] HEN on the surface of ice remains a possibility, but Shepherd et al.[33] found that clathrate cages did not form within the quasi-liquid layer that forms at the ice-methane interface during their simulation. In addition, they found no enhancement in methane solubility within the quasi-liquid layer, suggesting that *static* ice surfaces do not catalyze hydrate nucleation. Yet nucleation does occur on the surface of ice in experiments.[34–41]

Here, we take values of $A_{\mathrm{HON}} = 5 \times 10^{19}$ cm^{-3}s^{-1} and $B_{\mathrm{HON}} = 930$ from the calculations of Knott et al.[25] Even with a bulk supersaturation of $S = 5.8$, CNT predicts that the induction time in a 1 cm^3 volume is over 10^{103} years. However, freeze concentration can significantly accelerate nucleation. For an observation area of 1 cm^2, a saturated bulk solution, an ice growth rate of 1 μm/s, and a methane diffusivity of 1.46×10^{-9} m^2/s (i.e. diffusivity at 273 K), the average induction time is drastically reduced to 22 hours (see Table 2.1)! The calculation illustrates how freeze-concentration in the boundary layer can provide a sufficiently high driving force to induce hydrate nucleation. Molinero

and coworkers find, in preliminary tests of the new model, that freeze-out in methane-water solutions can generate methane bubbles instead. Understanding how pressure and other factors influence selectivity between alternative nucleation processes is therefore an interesting direction for future work.

2.4 Conclusion

In conclusion, a boundary layer of giant solute supersaturation develops ahead of the moving crystallization front when a freezing solvent (often ice) excludes the solute. We have developed stochastic models of boundary layer nucleation during freeze-concentration by using quasi-steady nucleation kinetics and a time-dependent one-dimensional model of the concentration profile in the boundary layer. We provide numerical calculations of average induction times and 90% relative confidence interval widths as a function of two dimensionless variables. Whether nucleation is heterogeneous on the ice surface or homogeneous in the solution, nucleation is dramatically accelerated by freeze-concentration. For methane hydrates, which can form concurrently with ice, induction times for homogeneous nucleation could be reduced by as much as 4 orders of magnitude times because of freeze-concentration.

The stochastic model of nucleation in the freeze-concentration boundary layer is widely applicable and requires only two dimensionless parameters. These can be obtained or estimated to understand a variety of freeze-concentration induced solute nucleation processes as listed in the introduction. For example, freeze-concentration can be responsible for pore formation during the crystallization of gas-saturated melts.[42–46] The dissolved gas accumulates at the crystallizing front until the local enrichment induces gas bubble nucleation. The crystallizing front then engulfs the bubble, forming a porous structure. Porosity in solids can have both positive and negative effects on mechanical

properties. Porous solids are more susceptible to stress concentration and failure but are also lightweight and have more surface area. Wei and coworkers have extensively studied the many variables that affect pore shape.[44,46–49] This work supplements our understanding of pore formation by modeling the variables that affect pore frequency and spacing.

Future work should also improve upon some oversimplifications in our model. For example, our stochastic treatment should be combined with more comprehensive models that account for surface charging,[50,51] fluid mechanics in the process of engulfment,[11,52–56] spontaneous convection driven by buoyancy in the boundary layer,[57] and cellular/dendritic growth.[58–60] Such a comprehensive model might enable quantitative comparisons to interferometry measurements of concentration profiles and bubble formation during freeze-concentration.[60]

Bibliography

[1] R. O'Concubhair and J. R. Sodeau, *The effect of freezing on reactions with environmental impact*, *Acc. Chem. Res.* (2013).

[2] W. G. Pfann, *Principles of zone-melting*, *Journal of Metals* **4** (1952), no. 7 747–753.

[3] W. A. Tiller, K. A. Jackson, J. W. Rutter, and B. Chalmers, *The redistribution of solute atoms during the solidification of metals*, *Acta Metallurgica* **1** (1953), no. 4 428–437.

[4] V. G. Smith, W. A. Tiller, and J. W. Rutter, *A mathematical analysis of solute redistribution during solidification*, *Can. J. Phys.* **33** (1955), no. 12 723–745.

[5] S. S. Deshpande, M. Cheryan, S. K. Sathe, and D. K. Salunkhe, *Freeze concentration of fruit juices*, *CRC Crit. Rev. Food Sci. Nutr.* **20** (1984), no. 3 173–248.

[6] B. H. Ryu and J. Ulrich, *Controlled nucleation and growth of protein crystals by solvent freeze-out*, *Cryst. Growth Des.* **12** (2012), no. 12 6126–6133.

[7] J. Ihli, A. N. Kulak, and F. C. Meldrum, *Freeze-drying yields stable and pure amorphous calcium carbonate (acc)*, *Chem. Commun.* **49** (2013), no. 30 3134–3136.

[8] L. Chen, Q. Kang, Y.-L. He, and W.-Q. Tao, *Mesoscopic study of the effects of gel concentration and materials on the formation of precipitation patterns*, *Langmuir* **28** (2012), no. 32 11754–11763.

[9] D. Kashchiev, *Nucleation: Basic Theory With Applications*. Butterworth-Heinemann, Oxford, 2000.

[10] R. G. Pohl, *Solute redistribution by recrystallization*, *J. Appl. Phys.* **25** (1954), no. 9 1170–1178.

[11] G. Lipp, C. Korber, S. Englich, U. Hartmann, and G. Rau, *Investigation of the behavior of dissolved-gases during freezing*, *Cryobiology* **24** (1987), no. 6 489–503.

[12] A. E. Carte, *Air bubbles in ice*, *Proceedings of the Physical Society of London* **77** (1961), no. 495 757–&.

[13] W. R. Wilcox and V. H. S. Kuo, *Gas bubble nucleation during crystallization*, *J. Cryst. Growth* **19** (1973), no. 4 221–228.

[14] L. Leal, *Advanced Transport Phenomena: Fluid Mechanics and Convective Transport Processes*. Cambridge University Press, 2007.

[15] W. Kurz and D. Fisher, *Fundamentals of solidification. 1*. Trans Tech Publications, Limited, 1989.

[16] E. Cussler, *Diffusion: Mass Transfer in Fluid Systems*. Cambridge University Press, 2009.

[17] A. I. Fedorchenko and A. A. Chernov, *Exact solution of the problem of gas segregation in the process of crystallization*, *International Journal of Heat and Mass Transfer* **46** (2003), no. 5 915–919.

[18] D. Kashchiev and G. M. van Rosmalen, *Review: Nucleation in solutions revisited*, *Cryst. Res. Technol.* **38** (2003), no. 7-8 555–574.

[19] K. F. Kelton, A. L. Greer, and C. V. Thompson, *Transient nucleation in condensed systems*, *J. Chem. Phys.* **79** (1983), no. 12 6261–6276.

[20] B. Peters, *Supersaturation rates and schedules: Nucleation kinetics from isothermal metastable zone widths*, *J. Cryst. Growth* **317** (2011), no. 1 79–83.

[21] D. Kashchiev and A. Firoozabadi, *Kinetics of the initial-stage of isothermal gas-phase formation*, *J. Chem. Phys.* **98** (1993), no. 6 4690–4699.

[22] D. Kashchiev, D. Verdoes, and G. M. Vanrosmalen, *Induction time and metastability limit in new phase formation*, *J. Cryst. Growth* **110** (1991), no. 3 373–380.

[23] L. Goh, K. Chen, V. Bhamidi, G. He, N. C. S. Kee, P. J. A. Kenis, I. Zukoski, Charles F., and R. D. Braatz, *A stochastic model for nucleation kinetics determination in droplet-based microfluidic systems*, *Cryst. Growth Des.* **10** (2010), no. 6 2515–2521.

[24] S. S. Kadam, S. A. Kulkarni, R. C. Ribera, A. I. Stankiewicz, J. H. ter Horst, and H. J. M. Kramer, *A new view on the metastable zone width during cooling crystallization*, *Chem. Eng. Sci.* **72** (2012) 10–19.

[25] B. C. Knott, V. Molinero, M. F. Doherty, and B. Peters, *Homogeneous nucleation of methane hydrates: Unrealistic under realistic conditions*, *J. Am. Chem. Soc.* **134** (2012), no. 48 19544–19547.

[26] V. Agarwal and B. Peters, *Precipitate Nucleation: A Review of Theory and Simulation Advances*, vol. 155 of *Advances in Chemical Physics*. John Wiley & Sons, New Jersey, USA, 2014.

[27] Kashchie.D, *Nucleation at time-dependent supersaturation*, *Surf. Sci.* **22** (1970), no. 2 319–&.

[28] M. R. Walsh, C. A. Koh, E. D. Sloan, A. K. Sum, and D. T. Wu, *Microsecond simulations of spontaneous methane hydrate nucleation and growth*, *Science* **326** (2009), no. 5956 1095–1098.

[29] M. R. Walsh, G. T. Beckham, C. A. Koh, E. D. Sloan, D. T. Wu, and A. K. Sum, *Methane hydrate nucleation rates from molecular dynamics simulations: Effects of aqueous methane concentration, interfacial curvature, and system size*, *J. Phys. Chem. C* **115** (2011), no. 43 21241–21248.

[30] R. W. Hawtin, D. Quigley, and P. M. Rodger, *Gas hydrate nucleation and cage formation at a water/methane interface*, *Phys. Chem. Chem. Phys.* **10** (2008), no. 32 4853–4864.

[31] J. Vatamanu and P. G. Kusalik, *Observation of two-step nucleation in methane hydrates*, *Phys. Chem. Chem. Phys.* **12** (2010), no. 45 15065–15072.

[32] L. C. Jacobson and V. Molinero, *Can amorphous nuclei grow crystalline clathrates? the size and crystallinity of critical clathrate nuclei*, *J. Am. Chem. Soc.* **133** (2011), no. 16 6458–6463.

[33] T. D. Shepherd, M. A. Koc, and V. Molinero, *The quasi-liquid layer of ice under conditions of methane clathrate formation*, *J. Phys. Chem. C* **116** (2012), no. 22 12172–12180.

[34] L. A. Stern, S. H. Kirby, and W. B. Durham, *Polycrystalline methane hydrate: Synthesis from superheated ice, and low-temperature mechanical properties*, *Energy & Fuels* **12** (1998), no. 2 201–211.

[35] W. F. Kuhs, D. K. Staykova, and A. N. Salamatin, *Formation of methane hydrate from polydisperse ice powders*, *J. Phys. Chem. B* **110** (2006), no. 26 13283–13295.

[36] G. Genov, W. F. Kuhs, D. K. Staykova, E. Goreshnik, and A. N. Salamatin, *Experimental studies on the formation of porous gas hydrates*, *Am. Mineral.* **89** (2004), no. 8-9 1228–1239.

[37] E. D. Sloan and F. Fleyfel, *A molecular mechanism for gas hydrate nucleation from ice*, *AIChE J.* **37** (1991), no. 9 1281–1292.

[38] P. Pirzadeh and P. G. Kusalik, *Molecular insights into clathrate hydrate nucleation at an ice-solution interface*, *J. Am. Chem. Soc.* **135** (2013), no. 19 7278–7287.

[39] A. N. Salamatin, T. Hondoh, T. Uchida, and V. Y. Lipenkov, *Post-nucleation conversion of an air bubble to clathrate air-hydrate crystal in ice*, *J. Cryst. Growth* **193** (1998), no. 1-2 197–218.

[40] A. Falenty, A. N. Salamatin, and W. F. Kuhs, *Kinetics of co2-hydrate formation from ice powders: Data summary and modeling extended to low temperatures*, *J. Phys. Chem. C* **117** (2013), no. 16 8443–8457.

[41] V. P. D. Borbon and J. Ulrich, *Sfo-solvent freeze out-technology for industrial proteins*, *J. Cryst. Growth* **373** (2013) 38–44.

[42] P. S. Wei, S. Y. Hsiao, and S. S. Hsieh, *Pore formation in solid*, *Journal of Mechanics* **28** (2012), no. 1 1–6.

[43] P. S. Wei and S. Y. Hsiao, *Pore shape development from a bubble captured by a solidification front*, *International Journal of Heat and Mass Transfer* **55** (2012), no. 25-26 8129–8138.

[44] S. Hsiao, P. Wei, and L. Wang, *Effects of physico-chemical interfacial equilibrium on pore shape in solid*, *International Journal of Heat and Mass Transfer* **117** (2018) 1–10.

[45] A. Pilnik and A. Chernov, *Exact solution of the problem of dissolved gas segregation by the plane crystallization front*, in *Journal of Physics: Conference Series*, vol. 899, p. 032019, IOP Publishing, 2017.

[46] S.-Y. Hsiao and P.-S. Wei, *Case study of ambient pressure effects on pore shape in solid*, *Journal of Thermophysics and Heat Transfer* (2017).

[47] P. Wei and S. Hsiao, *Effects of solidification rate on pore shape in solid*, *International Journal of Thermal Sciences* **115** (2017) 79–88.

[48] P. Wei and S. Hsiao, *Effects of supersaturation on pore shape in solid*, *Journal of Crystal Growth* **460** (2017) 126–133.

[49] S. Hsiao and P. Wei, *Bond number effects on pore shape in solid*, *International Journal of Thermal Sciences* **116** (2017) 73–81.

[50] G. W. Gross, *Workman-reynolds effect and ionic transfer processes at ice-solution interface*, *J. Geophys. Res.* **70** (1965), no. 10 2291–&.

[51] E. J. Workman and S. E. Reynolds, *Electrical phenomena occurring during the freezing of dilute aqueous solutions and their possible relationship to thunderstorm electricity*, *Phys. Rev.* **78** (1950), no. 3 254–259.

[52] G. Lipp, C. Korber, and G. Rau, *Critical growth-rates of advancing ice water interfaces for particle encapsulation*, *J. Cryst. Growth* **99** (1990), no. 1-4 206–210.

[53] G. Lipp and C. Korber, *On the engulfment of spherical-particles by a moving ice liquid interface*, *J. Cryst. Growth* **130** (1993), no. 3-4 475–489.

[54] J. Potschke and V. Rogge, *On the behavior of foreign particles at an advancing solid liquid interface*, *J. Cryst. Growth* **94** (1989), no. 3 726–738.

[55] G. F. Bolling and J. Cisse, *Theory for interaction of particles with a solidifying front*, *J. Cryst. Growth* **10** (1971), no. 1 56–&.

[56] D. R. Uhlmann, B. Chalmers, and K. A. Jackson, *Interaction between particles + solid-liquid interface*, *J. Appl. Phys.* **35** (1964), no. 10 2986–&.

[57] G. W. Gross, P. M. Wong, and K. Humes, *Concentration dependent solute redistribution at ice-water phase boundary .3. spontaneous convection - chloride solutions*, *J. Chem. Phys.* **67** (1977), no. 11 5264–5274.

[58] M. F. Butler, *Instability formation and directional dendritic growth of ice studied by optical interferometry*, *Cryst. Growth Des.* **1** (2001), no. 3 213–223.

[59] M. F. Butler, *Freeze concentration of solutes at the ice/solution interface studied by optical interferometry*, *Cryst. Growth Des.* **2** (2002), no. 6 541–548.

[60] K. Nagashima and Y. Furukawa, *Interferometric observation of the effects of gravity on the horizontal growth of ice crystals in a thin growth cell*, *Physica D* **147** (2000), no. 1-2 177–186.

Chapter 3

Introduction to studying nucleation via simulations

3.1 Rare event methods: tackling the separation of time scales

Simulations is an extremely valuable tool to improve our understanding of nucleation because it can overcome the many difficulties in directly observing nucleation, including the short lifetime and small length scale of nuclei. Typical simulations volumes of 100 to 1000 nm^3 and trajectory lengths of 1 ns to 1 μs are comparable to the small length and time scales of nucleation. However, traditional "brute force" simulations struggle to simultaneously account for the long and stochastic induction time. Even for the larger experimentally measured rates (i.e. about 10^{21} nuclei/cm^3s), it would take on average 1 ms to observe a *single* nucleation event in a 1000 nm^3 volume. Therefore, obtaining enough statistics for nucleation at moderate supersaturations using brute force simulations is generally impossible given current computational resources.

The easiest solution is to study nucleation at larger supersaturations, where the rate is exponentially larger and the induction time is significantly smaller. However, studies that do this are often dealing with nucleation rates that exceed experimental rates by several orders of magnitude.[1] Molecular insights at these unrealistic conditions might not be transferable to nucleation at temperatures, pressures, and concentrations of interest. Furthermore, nucleation may no longer be an activated process, and phase transitions might be governed by spinoidal decomposition.

Rare event methods provide a better suite of solutions for tackling the separation of time scales problem. The most popular rare event strategy in nucleation was pioneered by Daan Frenkel and coworkers.[2–5] Although nucleation is a non-equilibrium process, they recognized that the nucleation rate is composed of two components: (1) a thermodynamic and (2) a dynamic one:

$$J = \mathcal{D}(n^\ddagger) Z \rho_1 \exp\left[-\beta \Delta F(n^\ddagger)\right], \tag{3.1}$$

where $\rho_1 \exp\left[-\beta \Delta F(n^\ddagger)\right]$ is the equilibrium population of critical nucleus and $\mathcal{D}(n^\ddagger)$ is the attachment/detachment frequency to the critical nucleus. These two quantities can be separately computed. This naturally separates the nucleation process into two problems of different time scales: (1) the long process to form critical nuclei governed by quasi-equilibrium thermodynamics and (2) the fast dynamics of the growth or dissolution of near-critical nuclei. In other words, we can take advantage of the time scale separation to simplify the problem.[1]

$\mathcal{D}(n^\ddagger)$ is also the phase-space diffusion coefficient along the cluster size coordinate near the saddle point. This can be easily measured by analyzing trajectories of seeded

[1] This brilliant strategy still impresses me. The separation of time scales that initially presented so many obstacles can be used to break up a difficult problem into several small, simpler ones.

critical nuclei:

$$\mathcal{D}(n^{\ddagger}) \approx \frac{1}{2}\frac{d\left\langle (n(t)-n^{\ddagger})^2 \right\rangle}{dt}, \tag{3.2}$$

where $\left\langle (n(t)-n^{\ddagger})^2 \right\rangle$ is the mean squared displacement along the cluster size coordinate n.

The free energy $\Delta F(n^{\ddagger})$ to form a critical nuclei (i.e. nucleation barrier) is directly related to the equilibrium population $\mathcal{N}_{eq}(n^{\ddagger})$ of critical nuclei:

$$\Delta F(n^{\ddagger}) = -k_B T \ln \frac{\mathcal{N}_{eq}(n^{\ddagger})}{\mathcal{N}(1)}, \tag{3.3}$$

where $\mathcal{N}(1)$ is the number of monomeric clusters. $\mathcal{N}_{eq}(n^{\ddagger})/\mathcal{N}_{eq}(1)$ is vanishingly small, so estimating the ratio and therefore $\Delta F(n^{\ddagger})$ using brute force simulations would be *very* inaccurate. $\Delta F(n^{\ddagger})$ can be computed using advanced sampling techniques, like umbrella sampling.

Umbrella sampling is a method used to sample configurations from a biased distribution that is different from the Boltzman distribution. But due to clever variable manipulations, the biased distribution can still be used to compute averages in the Boltzman distribution. To see this, we define the thermal average $\langle \tilde{n} \rangle$ and probability density functions $P(\tilde{n})$ of our observable, the largest cluster size $\tilde{n}$ in the simulation volume:[2]

$$\langle \tilde{n} \rangle = \frac{\int d\mathbf{r}^N \ \tilde{n}(\mathbf{r}^N) P_{eq}(\mathbf{r}^N)}{\int d\mathbf{r}^N \ P_{eq}(\mathbf{r}^N)} \tag{3.4a}$$

$$P(\tilde{n}) = \frac{\int d\mathbf{r}^N \ \delta[\tilde{n}(\mathbf{r}^N) - \tilde{n}] P_{eq}(\mathbf{r}^N)}{\int d\mathbf{r}^N \ P_{eq}(\mathbf{r}^N)} = \left\langle \delta[\tilde{n}(\mathbf{r}^N) - \tilde{n}] \right\rangle, \tag{3.4b}$$

where $P_{eq}(\mathbf{r}^N)$ is the Boltzman weight for the full configuration $\mathbf{r}^N$ of all N atoms or

[2]For small values of $\tilde{n}$, $P(\tilde{n})$ can be related to $\mathcal{N}_{eq}(n)/\mathcal{N}_{eq}(1)$ by collecting statistics at the metastable basin. This doesn't require biased sampling because $P(\tilde{n})$ is not small. When $\tilde{n}$ exceeds a threshold $\tilde{n}^*$, the ratio of probabilities is equivalent to the ratio of populations: $P(\tilde{n})/P(\tilde{n}^*) = \mathcal{N}_{eq}(n)/\mathcal{N}_{eq}(\tilde{n}^*)$.

particles. Equation 3.4a can then be rewritten as

$$\begin{aligned}\langle\tilde{n}\rangle &= \frac{\int d\mathbf{r}^N\ \tilde{n}(\mathbf{r}^N)P_{eq}(\mathbf{r}^N)}{\int d\mathbf{r}^N\ P_{eq}(\mathbf{r}^N)} \\ &= \frac{\int d\mathbf{r}^N\ e^{\beta E_b(\mathbf{r}^N)}\tilde{n}(\mathbf{r}^N)P_{eq}(\mathbf{r}^N)e^{-\beta E_b(\mathbf{r}^N)}}{\int d\mathbf{r}^N\ P_{eq}(\mathbf{r}^N)e^{-\beta E_b(\mathbf{r}^N)}} \Big/ \frac{\int d\mathbf{r}^N\ e^{\beta E_b(\mathbf{r}^N)}P_{eq}(\mathbf{r}^N)e^{-\beta E_b(\mathbf{r}^N)}}{\int d\mathbf{r}^N\ P_{eq}(\mathbf{r}^N)e^{-\beta E_b(\mathbf{r}^N)}} \\ &= \frac{\left\langle\tilde{n}e^{\beta E_b}\right\rangle_b}{\left\langle e^{\beta E_b}\right\rangle_b}, \end{aligned} \tag{3.5}$$

and therefore Equation 3.4b can then be rewritten as

$$P(\tilde{n}) = \frac{\left\langle\delta[\tilde{n}(\mathbf{r}^N) - \tilde{n}]e^{\beta E_b}\right\rangle_b}{\left\langle e^{\beta E_b}\right\rangle_b}, \tag{3.6}$$

where $\langle\tilde{n}\rangle_b$ is the average of $\tilde{n}$ in the biased distribution $P_{eq}(\mathbf{r}^N)e^{-\beta E_b(\mathbf{r}^N)}$. Biasing potentials are cleverly chosen to restrict the largest nuclei in parallel simulations to overlapping narrow ranges of sizes that span the full range of sizes. The binned statistics can then be "stitched" together using the weighted histogram analysis method (WHAM)[6] or multistate Bennet acceptance ratio (MBAR).[7]

3.2 Open simulations: overcoming finite size effects

Rare event methods have been extensively used to study nucleation in one-component systems. For example, simulations have been used to understand condensation of vapor,[8] bubble formation from liquids,[9,10] magnetic phase transitions,[11] and phase transitions involving hard spheres[5] and Lennard-Jones particles.[10] Unfortunately, simulations of nucleation in multi-component systems is much more difficult. If the nucleating phase has a different composition than the bulk, the composition of the parent phase changes as the nucleus grows or shrinks if the simulated ensemble has a constant number of each species (see Figure 3.1).[12] In other words, the driving force for nucleation is not held constant,

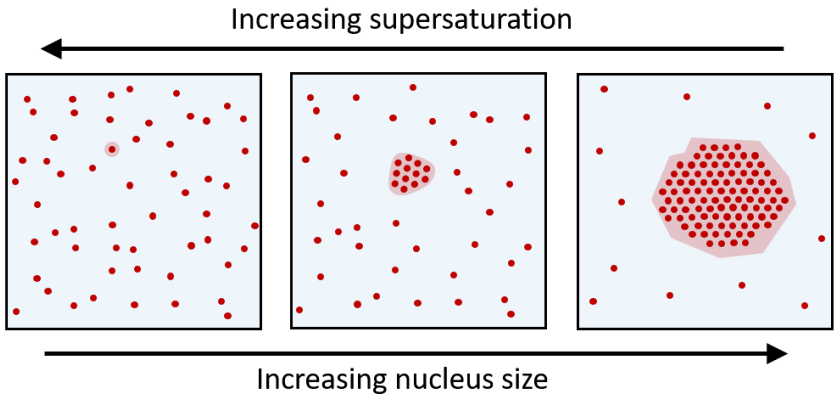

Figure 3.1: Diagram that shows that supersaturation changes as a nucleus grows in closed multi-component simulations.

making it incompatible with CNT. In fact, the nucleus can end up growing to a size that reaches a stable equilibrium with the depleted parent phase. This is qualitatively different from CNT, which models nucleation as an irreversible non-equilibrium transition.

To overcome this finite size effect, simulation sizes must either (1) be large enough that the growth of clusters only negligibly change the composition of the parent phase or (2) simulations are done using an open ensemble. The first option is often extremely computationally expensive because the large number of particles. The second option is traditionally achieved by simulating a grand canonical ensemble (i.e. μVT-ensemble), which holds the chemical potential of each species constant by coupling the insertion and deletion of molecules to a chemical potential bath. Since it holds the driving force constant, it is the ideal ensemble to study multi-component nucleation. However, insertion moves have a low probability of being accepted when the parent phase is a high density condensed phase.

The alternative open ensemble is the semigrand canonical ensemble,[13] which holds the total number of molecules constant as well as chemical potential *differences*. Instead of particle insertions, the semigrand ensemble mimics an open system by *exchanging*

molecules (e.g. swapping a solvent with a solute molecule). If the molecules being swapped are comparable sizes, the acceptance probability is high and efficient sampling is easy to achieve.

3.3 Summary

While nucleation is difficult to study with experiments due to the separation of time scales and small length scale, simulating nucleation has its own difficulties. However, advances in rare event methods has allowed us to take advantage of the separation of time scales. We can assume pre-critical nuclei are in quasi-equilibrium with the metastable state and separately study the dynamics of near-critical nuclei. This separation is reflected in the nucleation rate laws which relate the rate to the product of the equilibrium population of critical nuclei and growth dynamics of near-critical nuclei. We briefly reviewed the most popular rare event methods to compute equilibrium probabilities: umbrella sampling. Umbrella sampling uses biased simulations to accurately reconstruct the entire free energy landscape, including high free energy regions of phase space like the critical nucleus size. This allows an accurate determination of the equilibrium population of critical nuclei. We also briefly mentioned the importance in simulating open ensembles to avoid finite size effects. The nucleation driving force varies as a cluster grows in a closed simulation, making it difficult to compare the results to theories like CNT. The following two chapters utilize these two methods to study how additives promote nucleation in simple lattice simulations.

Bibliography

[1] M. R. Walsh, C. A. Koh, E. D. Sloan, A. K. Sum, and D. T. Wu, *Microsecond simulations of spontaneous methane hydrate nucleation and growth*, *Science* **326** (2009), no. 5956 1095–1098.

[2] P. Rein ten Wolde, M. J. Ruiz-Montero, and D. Frenkel, *Numerical calculation of the rate of crystal nucleation in a lennard-jones system at moderate undercooling*, *The Journal of chemical physics* **104** (1996), no. 24 9932–9947.

[3] P. R. ten Wolde and D. Frenkel, *Computer simulation study of gas–liquid nucleation in a lennard-jones system*, *The Journal of chemical physics* **109** (1998), no. 22 9901–9918.

[4] S. Auer and D. Frenkel, *Prediction of absolute crystal-nucleation rate in hard-sphere colloids*, *Nature* **409** (2001), no. 6823 1020–1023.

[5] S. Auer and D. Frenkel, *Numerical prediction of absolute crystallization rates in hard-sphere colloids*, *J. Chem. Phys.* **120** (2004), no. 6 3015–3029.

[6] S. Kumar, D. Bouzida, R. H. Swendsen, P. A. Kollman, and J. M. Rosenberg, *The weighted histogram analysis method for free-energy calculations on biomolecules .1. the method*, *J. Comput. Chem.* **13** (1992), no. 8 1011–1021.

[7] M. R. Shirts and J. D. Chodera, *Statistically optimal analysis of samples from multiple equilibrium states*, *The Journal of Chemical Physics* **129** (Aug., 2008) 124105–.

[8] R. B. Nellas, S. J. Keasler, J. I. Siepmann, and B. Chen, *Exploring the discrepancies between experiment, theory, and simulation for the homogeneous gas-to-liquid nucleation of 1-pentanol*, *J. Chem. Phys.* **132** (2010), no. 16.

[9] Z.-J. Wang, C. Valeriani, and D. Frenkel, *Homogeneous bubble nucleation driven by local hot spots: A molecular dynamics study*, *J. Phys. Chem. B* **113** (2009), no. 12 3776–3784.

[10] M. J. Uline, K. Torabi, and D. S. Corti, *Homogeneous nucleation and growth in simple fluids. ii. scaling behavior, instabilities, and the (n, v) order parameter*, *J. Chem. Phys.* **133** (2010), no. 17.

[11] G. Brown, M. A. Novotny, and P. A. Rikvold, *Micromagnetic simulations of thermally activated magnetization reversal of nanoscale magnets*, *J. Appl. Phys.* **87** (2000), no. 9 4792–4794.

[12] V. Agarwal and B. Peters, *Precipitate Nucleation: A Review of Theory and Simulation Advances*, vol. 155 of *Advances in Chemical Physics*. John Wiley & Sons, New Jersey, USA, 2014.

[13] D. A. Kofke and E. D. Glandt, *Monte-carlo simulation of multicomponent equilibria in a semigrand canonical ensemble*, *Mol. Phys.* **64** (1988), no. 6 1105–1131.

Chapter 4

Accelerating solute nucleation with molecular surfactants

4.1 Background

Metastable phases of matter include liquids that can be supercooled without freezing, vapors that can be supercooled without condensing, and solids that can exist as multiple polymorphs. Some metastable phases can survive for long times because the more stable phase cannot form without first surmounting an activation barrier for nucleation. Nucleation is a stochastic process that forms the first growing embryo of the more stable phase. Nucleation and growth from single component systems have been extensively studied, but there has been relatively little theoretical and computational work on solute precipitate nucleation. Even fewer studies have focused on nucleation in

the presence of additives.

Additives are important in nucleation and growth in many natural and industrial processes including ice formation,[1–5] pharmaceutical crystallization,[6–8] biomineralization,[9–16] and material synthesis.[17–20] For example, pharmaceutical companies use nucleants, growth promoters, and inhibitors to drive the selective crystallization of the desired polymorph.[21–24] Oil and gas companies invest millions of dollars on inhibitors to prevent methane hydrates from clogging pipelines.[25–27] Others have investigated additives to accelerate gas hydrate formation for gas storage at moderate temperatures and pressures.[28–31] In biology, salts, metabolytes, and proteins prevent the formation of urinary stones[32,33] and ice in Antarctic fish.[34–36] Therefore, there is substantial scientific and industrial interest in designing additives for controlling nucleation and growth. Additives are currently discovered by trial-and-error experiments rather than focused searches guided by physical models.

Classical nucleation theory (CNT) predicts that nucleation rates are primarily dependent on two competing factors: (1) the bulk chemical potential difference between the stable and metastable phases and (2) the interfacial free energy between the two phases.[37,38] The first factor is the nucleation driving force and is often written in terms of supersaturation (i.e. $\Delta\mu = k_B T \ln S$). The second factor, interfacial free energy, is directly responsible for the nucleation barrier. Although the nucleation barrier can be adjusted by modulating supersaturation, we are primarily interested in additives that selectively bind to the nucleus and lower the interfacial free energy. Surface-active additives can potentially have strong effects on nucleation at trace concentrations.

Most experimental and theoretical research on trace additives focus on crystal growth, not nucleation. For example, Weissbuch and coworkers have experimentally studied "tailor-made" stereospecfic promoters and inhibitors that drive the selective crystallization of polymorphs.[39,40] Ward and coworkers studied molecular inhibitors that bind

stereospecifically to growing crystal faces and suppress growth.[33,41] Storr et al.[26] and Anderson et al.[25] used molecular simulations to compare binding energies of hydrate growth inhibitors. All of these works investigate the effect of additives on large crystal surfaces instead of the microscopic clusters present during the nucleation stage.

A few recent theoretical studies investigated the effect of additives on nucleation, but these did not separately consider the interfacial and solubility contributions to the free energy barrier. Anwar et al. used short unbiased molecular simulations of a ternary Leonard Jones (LJ) system (i.e. solute-solvent-additive) to compare nucleation rates for different additive interaction and size parameters.[42] Duff et al. developed an alchemical transformation approach to compare the effects of NaCl on the interfacial free energy of nuclei for two polymorphs of glycine.[43] However, Duff et al. did not compute the effect of salt on the solubility of glycine in solution, a separately important effect of adding salt.

This chapter proposes a theoretically-motivated additive design equation that applies to low dosage nucleation promoters that strongly interact with the solution-precipitate interface. The equation is motivated by (1) the barrier's strong dependence on interfacial tension, (2) the drop in interfacial tension with increasing additive interfacial coverage, and (3) the increase in coverage with increasing additive concentration. It predicts a drop in barrier height proportional to trace additive concentration. The proportionality constant is the product of two measurable quantities: an equilibrium constant for adsorption and the reduction in interfacial tension per unit coverage. These two quantities are related to each other, so a method to quickly determine either property for a set of trial additives could help design potent nucleation promoters.

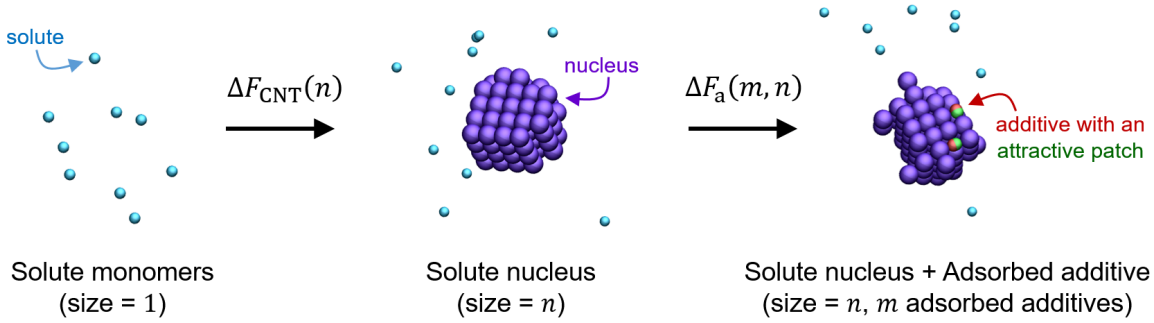

Figure 4.1: Schematic of the two-step free energy path used to compute the free energy of a nucleus of size n with m adsorbed additives. Solutes are shown in cyan. The largest nucleus is shown in violet for clarity. The surfactant additives are depicted as red/green Janus particles, where the green patch is the patch that favorably interacts with solutes.

4.2 Theory of thermodynamics: Combining Langmuir adsorption with CNT

4.2.1 Full two-dimensional treatment

The change in free energy is a state function and can be computed by constructing any free energy path that connects the initial and final states. Therefore, we decompose the reversible work $\Delta F(m,n)$ to homogeneously grow a nucleus of n solutes with m adsorbed additives into a two stage process (see Figure 4.1): (1) the work $\Delta F_{\mathrm{CNT}}(n)$ to grow a bare nucleus of size n in solution and (2) the work $\Delta F_{\mathrm{a}}(m,n)$ to adsorb m additives onto the nucleus of size n. If $\mathcal{N}(m,n)$ is the number of nuclei of size n with m adsorbed additives, then

$$\beta\Delta F_{\mathrm{CNT}}(n) = -\ln\frac{\mathcal{N}(0,n)}{\mathcal{N}(0,1)} \tag{4.1a}$$

$$\beta\Delta F_{\mathrm{a}}(m,n) = -\ln\frac{\mathcal{N}(m,n)}{\mathcal{N}(0,n)} \tag{4.1b}$$

where $1/\beta = k_{\mathrm{B}}T$ is the thermal energy. Therefore, the free energy landscape corresponds to the concentration of nuclei of different sizes and coverages relative to the isolated solute concentration:

$$\begin{aligned}\beta\Delta F(m,n) &\equiv \beta\Delta F_{\mathrm{CNT}}(n) + \beta\Delta F_{\mathrm{a}}(m,n) \\ &= -\ln\frac{\mathcal{N}(m,n)}{\mathcal{N}(0,1)}.\end{aligned} \tag{4.2}$$

$\Delta F_{\mathrm{CNT}}(n)$ is modeled by the classical nucleation theory (CNT) free energy expression discussed in Section 1.2.1:[37,38,44–47]

$$F_{\mathrm{CNT}}(n) = -n\Delta\mu + \gamma_0 a\phi n^{2/3}, \tag{4.3}$$

where $\Delta\mu$ is the chemical potential difference of the solute in the metastable solution and in the precipitate, γ_0 is the interfacial tension of an uncovered nucleus, ϕ is a shape factor such that $\phi n^{2/3}$ is the number of adsorption sites, and a is the area per adsorption site. With the Girshick-Chiu correction,[48,49] the reversible work to grow a nucleus from monomers (i.e. $n = 1$) is

$$\Delta F_{\mathrm{CNT}}(n) \equiv F_{\mathrm{CNT}}(n) - F_{\mathrm{CNT}}(1). \tag{4.4}$$

From Equation 4.1b, $\Delta F_{\mathrm{a}}(m,n)$ is clearly dependent on the probability $P(m|n)$ of a size n nucleus having m adsorbed additives. If $P(m,n)$ is the joint probability, then

$$\beta\Delta F_{\mathrm{a}}(m,n) = -\ln\frac{P(m,n)}{P(0,n)} = -\ln\frac{P(m|n)P(n)}{P(0|n)P(n)} = -\ln\frac{P(m|n)}{P(0|n)}, \tag{4.5}$$

because $\mathcal{N}(m,n) \propto P(m,n)$ and $P(m,n) = P(m|n)P(n)$ due to Bayes' theorem. Equation 4.2 does not yet make any assumptions on how to model the adsorption of additives.

However, choosing a model for the adsorption free energy allows us to predict how meaningful parameters affect adsorption behavior. Here, $\Delta F_{\mathrm{a}}(m,n)$ is modeled with one of the simplest statistical models of adsorption: Langmuir-type adsorption. Langmuir-type adsorption assumes localized adsorption onto uniform surface sites and no interaction between adsorbed molecules, which are both reasonable assumptions for dilute adsorbates.

Now we will summarize the derivation of $\Delta F_{\mathrm{a}}(m,n)$. If each adsorption site is identical and independent, then

$$P(m|N_{\mathrm{s}}(n)) = \frac{N_{\mathrm{s}}!}{m!(N_{\mathrm{s}}-m)!}\left\langle\theta\right\rangle^{m}\left(1-\left\langle\theta\right\rangle\right)^{N_{\mathrm{s}}-m}, \tag{4.6}$$

where $N_{\mathrm{s}} = \phi n^{2/3}$ is the number of binding sites, $\theta = m/N_{\mathrm{s}}$ is the fractional coverage, and $\langle\theta\rangle$ is its equilibrium average. Equation 4.6 clearly resembles a binomial distribution, where $\langle\theta\rangle$ is the success probability of each binomial trial. Using the Stirling approximation, we can approximate $P(m|n)$ in the small coverage limit (i.e. $\theta \to 0$). When combined with Equation 4.5, the adsorption free energy is approximately

$$\Delta F_{\mathrm{a}}(m,N_{\mathrm{s}}) = -N_{\mathrm{s}}\Phi(\theta) + m\Delta\mu_{\mathrm{a}}(\theta), \tag{4.7}$$

where Φ/a is the surface or spreading pressure,[50]

$$\Phi(\theta) \equiv -\frac{\partial\Delta F_{\mathrm{a}}}{\partial N_{\mathrm{s}}} = -k_{\mathrm{B}}T\ln(1-\theta), \tag{4.8}$$

and $\Delta\mu_{\mathrm{a}}$ is the chemical potential difference between adsorbed additives and additives in solution,

$$\Delta\mu_{\mathrm{a}}(\theta) \equiv \frac{\partial\Delta F_{\mathrm{a}}}{\partial m} = k_{\mathrm{B}}T\ln\left[\left(\frac{\theta}{1-\theta}\right)\left(\frac{1-\left\langle\theta\right\rangle}{\left\langle\theta\right\rangle}\right)\right]. \tag{4.9}$$

For equilibrium adsorption in the macroscopic limit, $\Delta\mu_{\mathrm{a}} = 0$ and the chemical

potential of the adsorbing species at the surface $k_{\mathrm{B}}T\ln[\theta/(1-\theta)q]$ is equivalent to that in the bulk solution $k_{\mathrm{B}}T\ln[\langle\theta\rangle/(1-\langle\theta\rangle)q]$.[50] If we assume the adsorbant is an ideal solute, then we can relate the adsorbant chemical potential in bulk solution to its concentration in solution:

$$\ln\frac{\langle\theta\rangle}{(1-\langle\theta\rangle)q}=\frac{\mu_{\mathrm{a}}^{\circ}(T,P)}{k_{\mathrm{B}}T}+\ln x_{\mathrm{a}}, \tag{4.10}$$

where q is the partition function for an adsorbed additive, μ_{a}° is the reference chemical potential of the additive in solution, and x_{a} is the additive mole fraction in solution. Equation 4.10 can then be rearranged to produce the Langmuir isotherm:[50]

$$\langle\theta\rangle=\frac{Kx_{\mathrm{a}}}{1+Kx_{\mathrm{a}}}, \tag{4.11}$$

where K is the Langmuir constant:

$$K\equiv qe^{\mu_{\mathrm{a}}^{\circ}/k_{\mathrm{B}}T}. \tag{4.12}$$

For small additive concentrations, Equation 4.11 simplifies to Henry's law (i.e. $\langle\theta\rangle = Kx_{\mathrm{a}}$).

Figure 4.2 shows what a typical free energy landscapes $\Delta F(m,n)$ (using Equation 4.2) look like. It is important to note that $\Delta F_{\mathrm{a}}(m,N_{\mathrm{s}}(n))\neq\Delta F_{\mathrm{a}}(m,n)$. Equation 4.7 is a continuous representation of the adsorption free energy, so a Jacobian factor $\mathcal{J}$ is needed to map ΔF_{a} from (m,N_{s}) to (m,n) coordinates:

$$\begin{aligned}\Delta F_{\mathrm{a}}(m,n) &= \Delta F_{\mathrm{a}}(m,N_{\mathrm{s}}(n))-k_{\mathrm{B}}T\ln\mathcal{J}\\ &= \Delta F_{\mathrm{a}}(m,N_{\mathrm{s}}(n))+\tfrac{k_{\mathrm{B}}T}{3}\ln\phi n.\end{aligned} \tag{4.13}$$

where $\mathcal{J}=dN_s/dn$. If the barrier is large, the Jacobian factor has a negligible effect on

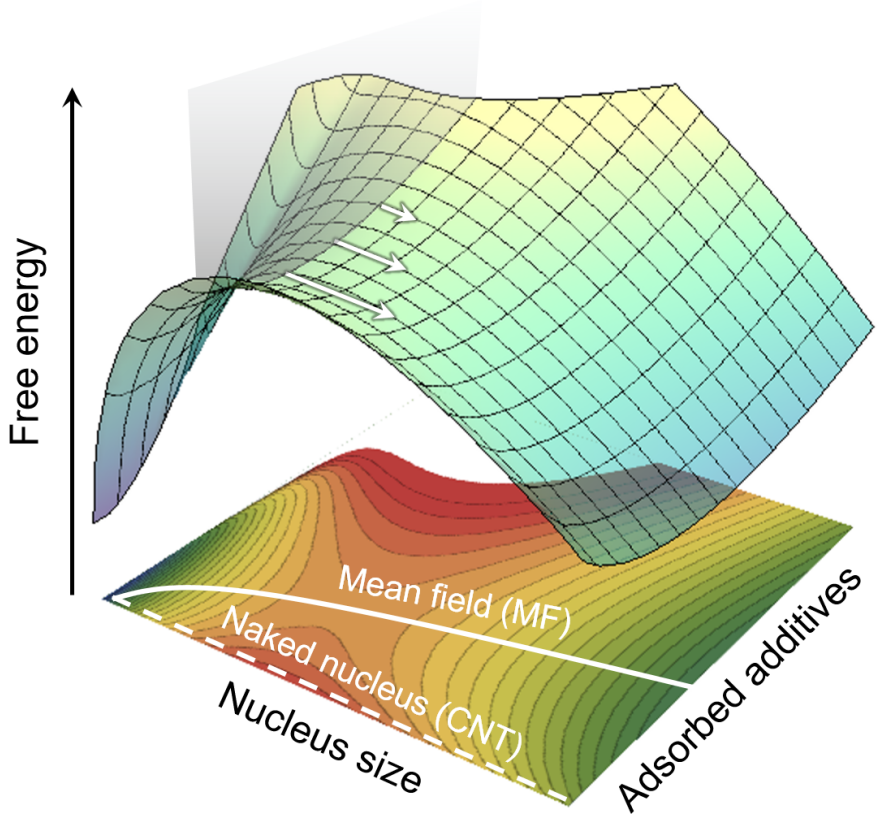

Figure 4.2: Free energy landscape as a function of number of absorbed additives (m) and nucleus size (n). The parameters used in Equation **??** are: $\Delta\mu/k_BT = 4/3$, $\gamma_0 a/k_BT = 4/3$, $\phi = 6$, and $\langle\theta\rangle = 0.05$. Mean-field models assume nucleating trajectories follow the $\theta = \langle\theta\rangle$ contour (solid white line). No-additive trajectories follow classical nucleation theory (dashed white line). The saddle point is approximately at $m_\ddagger = \langle\theta\rangle\,\phi n^{2/3}$ and $n_\ddagger = (2a\phi\gamma(\langle\theta\rangle)/3\Delta\mu)^3$.

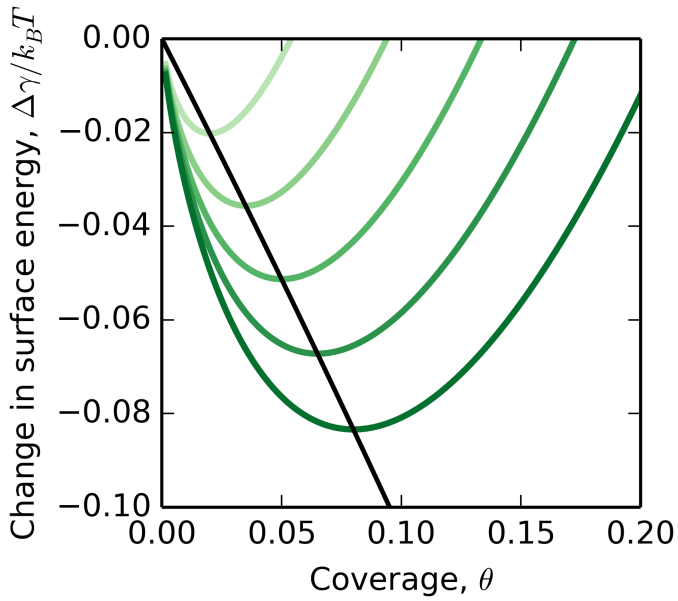

Figure 4.3: Plot of change in surface energy $\Delta\gamma(\theta)$ due to adsorption according to Equation 4.14. From light to darker green, $\langle\theta\rangle = 0.02$, 0.035, 0.05, 0.065, and 0.08. The black curve corresponds to $\Delta\gamma(\langle\theta\rangle) = -\Phi(\langle\theta\rangle)/a$, which shows $\Delta\gamma$ for the minimum free energy path model that assumes equilibrium adsorption (i.e. $\Delta\mu_{\mathrm{a}} = 0$) in the macroscopic limit.

the free energy surface near the saddle point and will be ignored from now on. However, it is necessary to recover the no-additive landscape (i.e. $\Delta F = \Delta F_{\mathrm{CNT}}$) when $\langle\theta\rangle = 0$ and the m-coordinate is integrated out.

If we ignore the negligible Jacobian factor, $\Delta F_a(m,n)$ scales proportionally to the surface area of the nucleus $a\phi n^{2/3}$. This suggests that we can directly relate $\Delta F_a(m,n)$ to the change in surface energy $\Delta\gamma(\theta)$ due to the adsorption of additives (see Figure 4.3):

$$\Delta\gamma(\theta(m,n)) \equiv \frac{\Delta F_{\mathrm{a}}(m,n)}{a\phi n^{2/3}} = \frac{1}{a}\left[-\Phi(\theta(m,n)) + \theta(m,n)\Delta\mu_{\mathrm{a}}(\theta(m,n))\right], \tag{4.14}$$

where $\theta = m/\phi n^{2/3}$, $\Phi(\theta)$ is defined by Equation 4.8, and $\Delta\mu_{\mathrm{a}}(\theta)$ is defined by Equation 4.9. We can better understand the implications of Equation 4.14 if we make a simplifying assumption: the adsorption of additives to the surface of the nucleus is in macroscopic

equilibrium (i.e. there is no fluctuations in coverage, $\theta = \langle\theta\rangle$, and $\Delta\mu_{\mathrm{a}} = 0$).[1] If we make this assumption, the change in surface energy becomes

$$\Delta\gamma(\langle\theta\rangle) = -\frac{\Phi(\langle\theta\rangle)}{a} = \frac{k_B T}{a}\ln(1 - \langle\theta\rangle). \tag{4.15}$$

Since we are primarily interested in the low coverage limit (i.e. $\langle\theta\rangle \ll 1$), the surface energy is reduced approximately linearly with coverage: $\Delta\gamma \approx -k_B T \langle\theta\rangle / a$. This suggests that stronger adsorbing additives (i.e. larger values of $\langle\theta\rangle$) are more effective at reducing the surface energy.

Equation 4.15 is consistent with the Gibbs adsorption isotherm, which relates the surface excess Γ_{a} of the adsorbant to the change in surface energy:

$$\Gamma_{\mathrm{a}} = -\frac{1}{k_B T}\left(\frac{\partial\gamma}{\partial \ln c_{\mathrm{a}}}\right), \tag{4.16}$$

where c_{a} is the concentration of the adsorbant. If an additive favorably adsorbs to the surface (i.e. $\Gamma_{\mathrm{a}} > 0$), the surface energy *must* decrease with increasing additive concentration (i.e. $\partial\gamma/\partial \ln C_{\mathrm{a}} < 0$). The same qualitative trend is shown in Equation 4.15. If the additive favorably adsorbs onto the surface, increasing additive concentration increases $\langle\theta\rangle$ (see Equation 4.11) and therefore decreases the surface energy.

We get our final expression for the free energy landscape $\Delta F(m, n)$ by combining

[1] Macroscopic equilibrium is not always the same as thermal equilibrium. For thermal equilibrium at both small and large length scales, the probability of a particular state is equal to its Boltzman weight. However, at large length scales, the probability distribution is *strongly* peaked at the lowest free energy state. For small length scales, thermal fluctuations allow the system to explore states around the most stable state.

Equation 4.2, 4.3, 4.4, and 4.14:

$$\begin{aligned}\Delta F(m,n) &= \Delta F_{\mathrm{CNT}}(n) + \Delta F_{\mathrm{a}}(m,n) \\ &= \left\{-(n-1)\Delta\mu + \gamma_0 a\phi\left(n^{2/3}-1\right)\right\} + \left\{\Delta\gamma(\theta(m,n))a\phi n^{2/3}\right\} \\ &= -(n-1)\Delta\mu + \gamma_0 a\phi\left[\left(1+\frac{\Delta\gamma(\theta(m,n))}{\gamma_0}\right)n^{2/3}-1\right]. \end{aligned} \tag{4.17}$$

Equation 4.17 is very similar to the CNT expression for $\Delta F(n)$. The only difference is the $(1+\Delta\gamma/\gamma_0)$ factor that accounts for the adsorbing additives decreasing the surface energy. As expected, if there is no change in the surface energy (i.e. $\Delta\gamma = 0$), we recover the CNT expression for $\Delta F(n)$. It is important to note that we assumed that additives change the surface energy but have a negligible affect on the chemical potential $\Delta\mu$ of the nucleating solute. This is an assumption we can relax by computing the relationship between the solute activity coefficient and the solution composition.

4.2.2 Minimum free energy path and potential of mean force

Mean field (MF) model

Mean-field approximations simplify models by neglecting fluctuations in one or more variables. Instead of accounting for the distribution of values that variable(s) can take, its contribution to the free energy is approximated by a single averaged effect. In the context of this work, we ignore the fluctuations in additive coverage (i.e. $\theta = \langle\theta\rangle$).[51,52] This reduces the full two-dimensional landscape to a one-dimensional one along the size coordinate.

Ignoring the negligible Jacobian factor, the mean-field free energy is[2]

$$\begin{aligned}\Delta F_{\mathrm{MF}}(n) &= -[n-1]\Delta\mu + [\gamma_0 + \Delta\gamma(\langle\theta\rangle)]a\phi\left[n^{2/3}-1\right] \\ &= -[n-1]\Delta\mu + [\gamma_0 + k_BT\ln(1-\langle\theta\rangle)]a\phi\left[n^{2/3}-1\right]. \end{aligned} \tag{4.18}$$

$\Delta F_{\mathrm{MF}}(n)$ is the same as ΔF_{CNT} except the surface energy is now $\gamma = \gamma_0 + k_BT\ln(1-\langle\theta\rangle)/a$. Therefore, the mean-field free energy of a critical nucleus (i.e. $d\delta F_{\mathrm{MF}}/dn = 0$ at $n = n^{\ddagger}_{\mathrm{MF}}$), or nucleation barrier, is

$$\begin{aligned}\Delta F^{\ddagger}_{\mathrm{MF}} &= \frac{4(\gamma a\phi)^3}{27\Delta\mu^2} - [-\Delta\mu + \gamma a\phi] \\ &= \left[\frac{4(\gamma_0 a\phi)^3}{27\Delta\mu^2} + \Delta\mu - \gamma_0 a\phi\right] - k_BT\left[\frac{4(\gamma_0 a\phi)^2}{9\Delta\mu^2} - 1\right]\phi\langle\theta\rangle + \cdots \\ &= \Delta F^{\ddagger}_{\mathrm{CNT}} - k_BT\left[3\frac{F^{\ddagger}_{\mathrm{CNT}}}{\gamma_0 a\phi} - 1\right]\phi K x_{\mathrm{a}} + \cdots. \end{aligned} \tag{4.19}$$

The second equality is a Taylor series expansion of the first equality around $\langle\theta\rangle$. Since we are primarily interested in low coverage situations, we higher order terms are safely neglected. The third equality comes from a simple substitution using Equation 4.3, 4.4, and 1.6 and predicts an approximately linear drop in barrier heights with increasing additive concentration x. Equation 4.19 differs from our previous mean-field model which predicts a different slope when the drop in barrier is plotted as function of Kx_{a}.[51] This is because our previous study did not account for the configurational degeneracies of adsorbed additives that are now included in the spreading pressure.

It is important to note that the mean field model reproduces the minimum free

[2]Equation 4.18 is not quite what you might expect from looking at Equation 4.17 (i.e. $\Delta F_{\mathrm{MF}}(n) \neq \Delta F(m = \langle\theta\rangle\phi n^{2/3}, n)$). This is because doing so would make $\Delta F_{\mathrm{MF}}(1)$ nonzero. This means that the reference state (i.e. when the free energy is zero) is not a bare isolated solute, but a solute with a coverage of $\langle\theta\rangle$. Since we are specifically interested in situations when the coverage is small, the free energy discrepancy (i.e. $\Delta\gamma(\langle\theta\rangle)a\phi$) is small as well.

energy path (MFEP). The MFEP is the path that connects two states (usually free energy minima) via a saddle point and is always parallel to ∇F (i.e. $(\nabla F)^{\perp} = 0$ along the whole path), where F defines the free energy landscape. In this case, the MFEP represents the quasi-equilibrium "path of least resistance" to overcome the barrier and form a post-critical nuclei. We will also show in Section 4.4 that the MFEP is the reaction coordinate if the attachment frequency of additives and solutes to the nucleus are equivalent.

Potential of mean force (PMF)

We improve upon mean-field predictions by using the potential of mean force (PMF) along the size coordinate. For simulations, this is equivalent to computing the PMF along the n-coordinate using umbrella sampling or other free energy methods. The PMF $\Delta F_{\mathrm{PMF}}(n)$ is estimated by using a quadratic expansion of $\Delta F(m,n)$ around the $m = \langle\theta\rangle\, \phi n^{2/3}$ contour and integrating out the m-dependence.

$$\begin{aligned} \Delta F(m,n) &\approx \Delta F_{\mathrm{MF}}(n) + \frac{1}{2}\left(\frac{\partial^2 \Delta F}{\partial m^2}\right)_{\mathrm{MF}} \delta m^2 + \cdots \\ &\approx \Delta F_{\mathrm{MF}}(n) - \frac{k_B T}{2\sigma^2}\delta m^2 + \cdots . \end{aligned} \tag{4.20}$$

and integrating out the m-dependence. For small coverages, the predicted drop in barrier using the PMF is

$$\frac{\Delta F^{\ddagger}_{\mathrm{PMF}}}{k_{\mathrm{B}}T} - \frac{\Delta F^{\ddagger}_{\mathrm{CNT}}}{k_{\mathrm{B}}T} = -\left[3\frac{F^{\ddagger}_{\mathrm{CNT}}}{\gamma_0 a} - \phi\right] K x_{\mathrm{a}} - \ln\left[\frac{1+\mathrm{erf}\sqrt{\phi n_{\ddagger}^{2/3} K x_{\mathrm{a}}/2}}{1+\mathrm{erf}\sqrt{\phi K x_{\mathrm{a}}/2}}\right] + \cdots , \tag{4.21}$$

which includes an additional term not found in Equation 4.19. Sometimes this term is comparable to the predicted effect of additives using the mean-field model. This is especially true at very low coverages, where the extra term approximately scales with

$\sqrt{Kx_a}$ and is often larger than the mean-field term that only scales with Kx_a. Therefore the sum over fluctuations *should be included* if accurate barriers and rates are required.

4.3 Monte Carlo simulations of Potts lattice gas

4.3.1 Ternary Potts lattice gas (PLG) model

Lattice models enable the investigation of metastable solutions independent of system-specific chemical details.[53,54] They are frequently used to test new rare event algorithms and to provide general insight into nucleation but primarily on single component systems. A number of studies have combined lattice gas simulations with theoretical analyses based on CNT.[54–57] For example, Pan and Chandler studied the transition state ensemble of critical nuclei of an lattice gas model and confirmed that cluster size is a reasonable reaction coordinate for nucleation.[58] Sear used lattice gas models to investigate heterogeneous nucleation in pores of different shapes and sizes.[59–61]

The Potts model is a generalization of the lattice gas model with each Potts orientation representing a particular phase or component[62,63] and has been used to study structural transitions in solids.[64,65] Peters and coworkers developed a binary Potts lattice gas (PLG) model with a lattice gas-like degree of freedom to distinguish between lattice sites occupied by solutes or solvents and a Potts-like degree of freedom to represent the orientation of molecules or lattice vectors at each lattice site.[66,67] The PLG model is a minimal nearest-neighbor model for orientation-specific interactions between solute-solute, solute-solvent, and solvent-solvent pairs. The interaction parameters can be tuned to obtain phase diagrams that resemble those of real binary mixtures. The PLG and closely related models have now been used in studies of phase equilibria, self-assembly, and several nucleation processes.[66–72]

The model in this work starts with the PLG and incorporates additives as a third component. Each lattice site is therefore occupied by either a solute, solvent, or additive (labeled species $k = 1$, 2, and 3 respectively) having one of $Q = 24$ possible orientations. 24 is the number of possible orientations for a cube with 6 distinguishable faces, so for a cubic lattice, $Q = 24$ represents the most asymmetric case.[73][3] The PLG Hamiltonian takes solute-solvent interactions as the zero of energy and sums over all nearest neighbor solute-solute, solvent-solvent, and additive-solute interactions. Using the notation $\langle i, j \rangle$ to denote nearest neighbor pairs, the Hamiltonian is:

$$\beta H = \beta H_0 + \beta \Delta H \tag{4.22}$$

where $\beta \Delta H$ and βH_0 are the additive and additive-free Hamiltonians respectively. The solute-solute and solvent-solvent interactions are those of the standard PLG model:

$$\beta H_0 = -\sum_{k=1}^{2} \sum_{\langle i,j \rangle} \delta_{m(i),k} \delta_{m(j),k} \left[\beta G_k + \beta A_k \delta_{s(i),s(j)} \right] \tag{4.23}$$

where $m(i)$ represents the species at lattice site i, $s(i)$ represents the local orientation of the molecule at lattice site i, and βG_k and βA_k are the species-specific and orientation-specific interaction respectively. βG_1 and βG_2 stabilize solute-solute and solvent-solvent pairs respectively and primarily control the solubility of solute in the solvent-rich phase and solvent in the solute-rich phase. Like neighbors with matching orientations are further stabilized by βA_1 and βA_2. For this study, we use the following PLG Hamiltonian parameters: $\beta G_1 = \beta G_2 = \beta A_1 = 1.25$ and $\beta A_2 = 0$. This choice of PLG parameters results in a weakly soluble solute and a relatively pure solute precipitate identical to the binary PLG model shown on Figure 1a of Duff and Peters at $k_B T = 0.8$ (see Figure

[3]Smaller values of Q can be used to represent more symmetric molecules.[74,75] However, we stick with $Q = 24$.

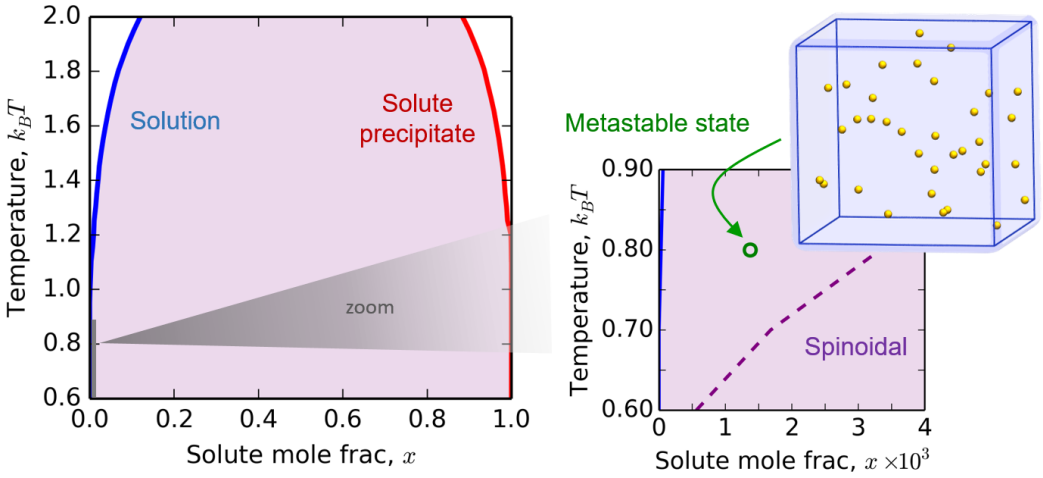

Figure 4.4: The phase diagram for the binary solute-solvent system determined by two-phase coexistence simulations. All simulations are done at $k_BT = 0.8$.

4.3.1).[66,73]

The additives mimic amphiphilic molecules through interactions that favor adsorption at the solute precipitate-solution interface. Additive-solvent and additive-additive interactions are equivalent to the zero energy solute-solvent interactions, making the additives sparingly soluble in solution and preventing them from aggregating. Additives interact with solutes only along the direction of their orientation:

$$\beta\Delta H = -\sum_{\langle i,j \rangle} \delta_{m(i),3}\delta_{m(j),1}\delta_{g(i),n(j,i)}\beta A_3 \tag{4.24}$$

where $n(j,i)$ is the neighbor index of lattice site j with respect to lattice site i which varies from 1 to 6 for a cubic lattice and $g(i)$ indexes the neighbor to which the orientation of the additive at lattice site i points. For a cubic lattice, $g(i) =$ mod $[Q,6]+1$ (i.e. 1 plus the remainder of $Q/6$) also varies from 1 to 6. Therefore, only additives whose orientation points toward a solute experiences a favorable interaction (see Figure 4.5). This directional additive-solute interaction mimics the attraction between the head/tail

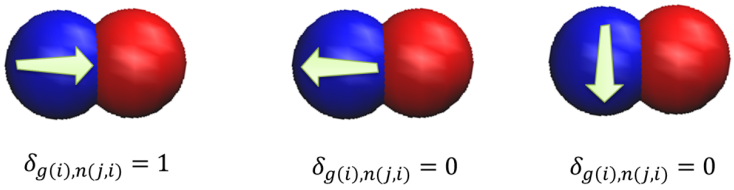

Figure 4.5: The additive (blue) only interacts with a neighboring solute if its orientation points toward a solute (red), i.e. $g(i) = n(j, i)$.

group of surfactants and the interface and prevents the nucleating phase from having many additive inclusions even though their interactions are strong. For this study, we used five different values of βA_3 to investigate the effect of additive binding strength: $\beta A_3 = 2.5$, 2.875, 3.125, 3.375 , and 3.75.

4.3.2 Simulation details

In a small closed simulation with fixed composition, a solute nucleus depletes the solute from its surroundings and consumes the driving force for its own growth.[47,76–79] Because of these finite size effects, solute precipitate nucleation is best simulated in the grand or semigrand (open) ensembles.[47,66,67,80] We use semigrand canonical Monte Carlo (SGMC) (or NT$\{\mu_i - \mu_r\}$ ensemble) simulations[81] to maintain differences in chemical potentials of each species and that of the solvent reference species. Our SGMC moves include (1) local and non-local swaps, (2) orientation flips, and (3) semigrand identity changes (see Figure 4.6). The first two move types are accepted or rejected using the standard canonical Metropolis criterion. The acceptance probability for identity changes from species i to j involves an additional fugacity ratio prefactor.[81]

Free energy landscapes along the nucleus size coordinate n are computed as:

$$\beta F(n) = -\ln \frac{\langle N(n) \rangle}{\langle N(1) \rangle} \tag{4.25}$$

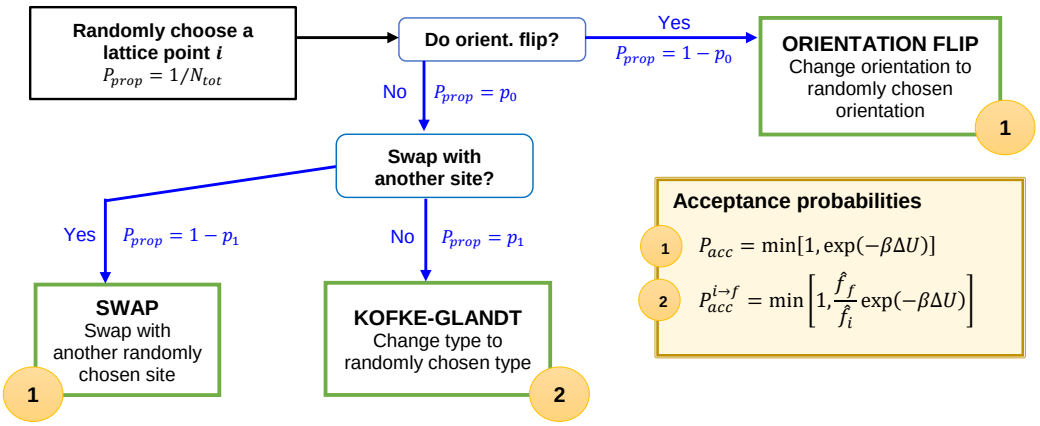

Figure 4.6: Algorithm of a single random move of a sweep.

where $\langle N(n) \rangle$ is the average number of nuclei composed of n solute monomers in the simulation box.[47,82,83] The size n of each nucleus is computed by counting contiguously neighboring solutes. However, it is computationally impractical to calculate $F(n)$ using unbiased Boltzman sampling for high barrier processes due to the exponentially vanishing probability of visiting higher free energy states. We overcome this issue with umbrella sampling which imposes a set of artificial biasing potentials to improve sampling of less probable configurations.[84–86] We use windows of width three units along the nucleus size n-coordinate with hard walls at the window edges. Each umbrella window is sampled for at least 500,000 SGMC sweeps to guarantee sufficient sampling.

Compositions of equal driving force

The nucleation free energy barrier depends on both the driving force (or supersaturation) and interfacial free energy. To isolate the effects of the additive on the interfacial free energy, we prepared compositions of equal driving force. The driving force is measured by simulating slab growth in a long elongated cell (in this case a 10x10x80 lattice)

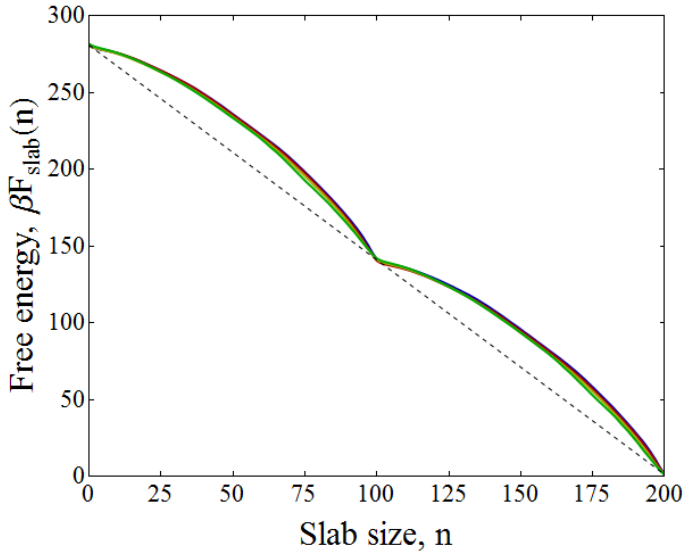

Figure 4.7: The free energy landscape of solute slab growth at different fugacity ratios with the same driving force for $\beta A_3 = 3.75$. The driving force $\Delta\mu$ is estimated by the common tangent through troughs (dashed line).

which maximizes the volume to surface ratio for a two phase system. The change in free energy for layer-by-layer slab growth is $F_{slab}(n) - F_{slab}(n_0) = -(n - n_0)\Delta\mu$. The driving force is therefore:[87]

$$\Delta\mu = -\frac{\partial F_{slab}}{\partial n} \tag{4.26}$$

The set of compositions of constant driving force can be calculated by the following iterative process:

1. Simulate slab growth using SGMC and calculate the dimensionless driving force with no additive ($\beta\Delta\mu_0$) using Equation 4.26.

2. Adjust the additive-solvent (f_3/f_2) and solute-solvent (f_1/f_2) fugacity ratio and repeat Step 1 until the driving force is approximately $\beta\Delta\mu_0$.

3. Repeat Step 2 for each solute-solvent-additive composition.

Increasing f_1/f_2 will increase the solute concentration and therefore driving force. In-

creasing f_3/f_2 will increase the additive concentration and therefore increase coverage, lower interfacial tension, and lower barrier height. The four sets of fugacity ratios we use that have the same driving force are: $f_1/f_2 = 2.25$ and $f_3/f_2 = 0$, $f_1/f_2 = 2.25$ and $f_3/f_2 = 0.01$, $f_1/f_2 = 2.258$ and $f_3/f_2 = 0.03$, and $f_1/f_2 = 2.26$ and $f_3/f_2 = 0.05$. These fugacity ratios are used for each metastable state in all other simulations. The composition of each metastable state is determined using unbiased 500,000 sweep-long SGMC simulations on a $64 \times 64 \times 64$ periodic lattice.

Free energy barriers and interfacial tension

We use umbrella sampling to compute the work required to grow a nucleus from size 1 to n on a $32 \times 32 \times 32$ periodic lattice.[84–86,88] Since the probability of observing more than one cluster of size $n > 4$ in our simulation box is negligible, $N(n)$ for values of $n > 4$ is approximated by the probability that the largest cluster in the system is of size n.[82,83] CNT fits of the free energy landscape with Equation 4.3 and 4.4 used to estimate nucleation barriers and interfacial tension.

Additive adsorption

SGMC simulations are used to estimate the adsorption constant. Simulations are done on a $64 \times 64 \times 64$ lattice with a 64×64 solute sheet. The sheet is not allowed to grow, dissolve, or change any of its Potts degrees of freedom. Coverage is estimated by averaging the fraction of lattice sites neighboring the solute sheet that is occupied by an additive[89] from at least 500,000 SGMC sweeps.

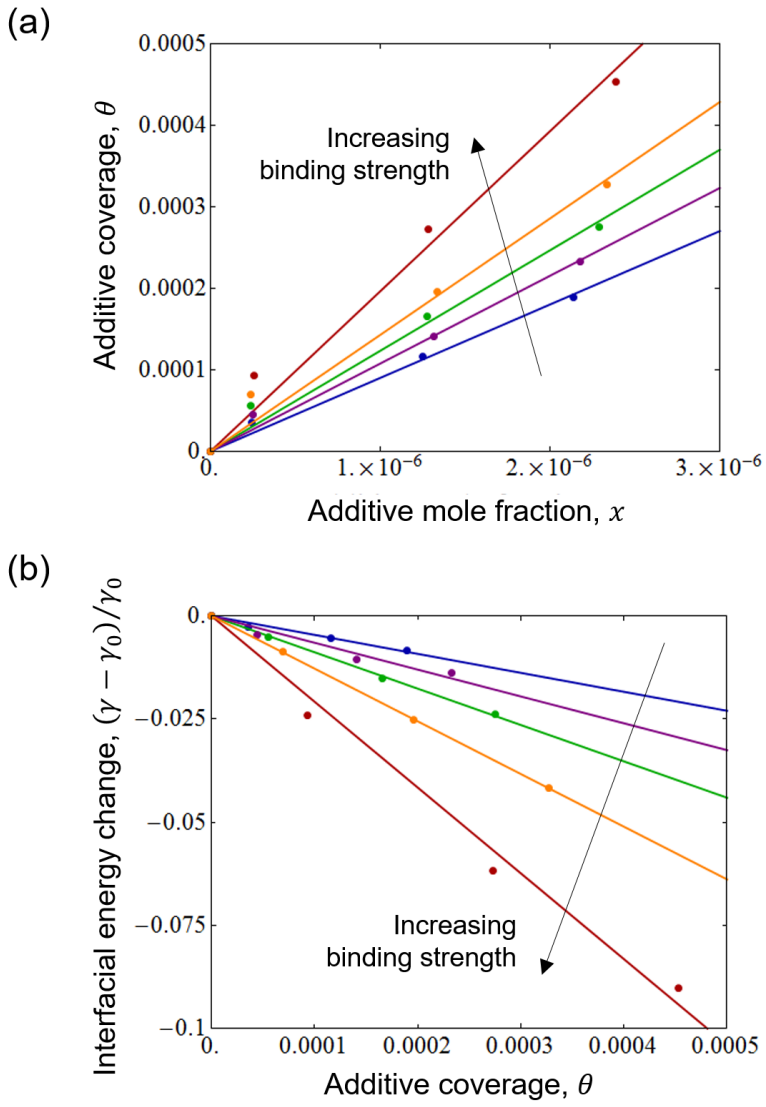

Figure 4.8: Proportional relationships between (a) additive coverage θ and additive concentration x and (b) change in interfacial free energy $(\gamma - \gamma_0)/\gamma_0$ and θ. Lines are linear fits constrained to pass through the origin for additive-solute interactions $\beta A_3 = 2.5$ (blue), 2.875 (purple), 3.125 (green), 3.375 (orange), and 3.75 (red).

4.3.3 Results and comparison to theory

Figure 4.8a shows that the average additive coverage θ for a range of average additive mole fraction x agrees with the predicted Henry's law behavior at low concentrations. Figure 4.9 shows the free energy $F(n)$ for the four compositions of equal driving force for $\beta A_3 = 3.75$, which is qualitatively similar for other values of βA_3. Interfacial tension

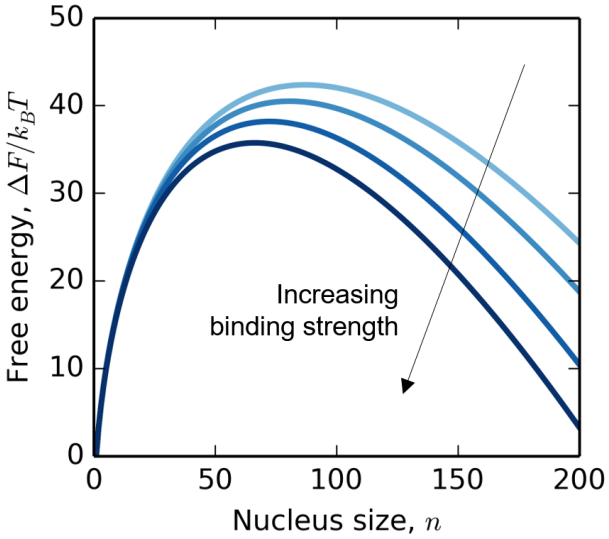

Figure 4.9: The reversible work $\beta F(n)$ to create a nucleus of size n at different additive concentrations for $\beta A_3 = 3.75$ at different binding strengths. The curves are well described by CNT fits with the constraint that the driving force at each additive concentration is the same.

$\beta a \gamma \phi$ is obtained by fitting $F(n)$ to Equation 4.3 and 4.4 for each additive concentration with the constraint that the driving force at each additive concentration is the same. The proportional relationships in Figures 4.8a and b are consistent with our theoretical prediction that increased adsorption will lower interfacial tension.

Figure 4.10 shows that Equation 4.21 accurately models our data for all additive-solute interactions and correctly predicts the data collapse when barrier reductions is plotted against coverage. Mean-field models that lack the additional term in Equation

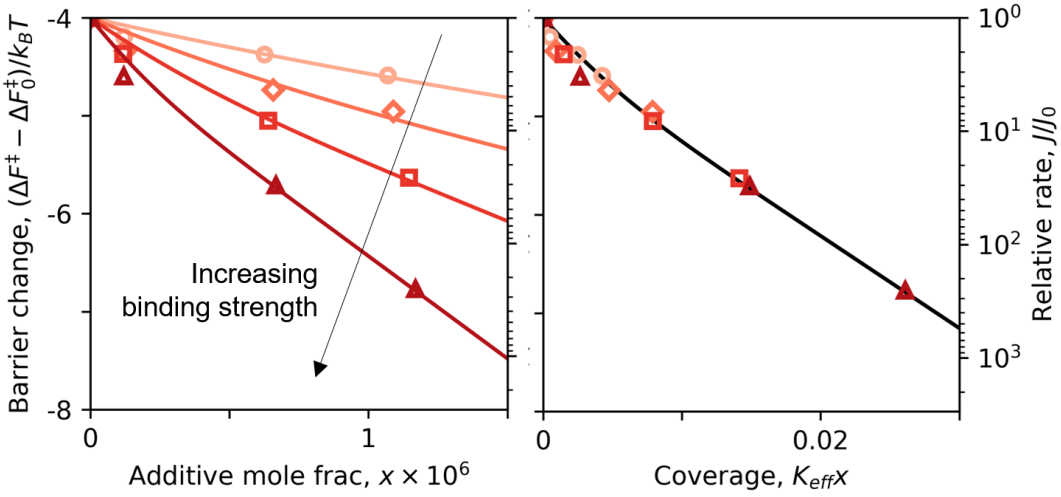

Figure 4.10: The change in free energy barrier as a function of additive mole fraction or coverage for additive-solute interactions (from light to dark red) $\beta A_3 = 2.5$, 2.875, 3.125, 3.375, and 3.75. The lines are fits using Equation 4.21 (the predicted potential of mean force) where K_{eff} is the lone fitting parameter.

4.21 cannot capture the sudden drop in barrier at very small coverages that causes the non-linear behavior. This suggests that Equation 4.21 should be used by simulations to predict the effect of additives on barriers.

4.4 Theory of dynamics: Rates and reaction coordinates

We can estimate the effect of additives on the rate J_{PMF} using Equation 4.21 and the Zeldovich-Frenkel equation: $J = c_{\mathrm{s}}\mathcal{D}(n^{\ddagger})Z\exp[\Delta F^{\ddagger}/k_{\mathrm{B}}T]$ where Z is the Zeldovich factor ($2\pi k_BTZ^2 = (\partial^2\Delta F/\partial n^2)_{\ddagger}$) and $\mathcal{D}(n^{\ddagger})$ is the phase space diffusion coefficient along the n-coordinate near the critical nucleus size. For low coverages, the ratio of Zeldovich factors is

$$\ln\frac{Z_{\mathrm{PMF}}}{Z_{\mathrm{CNT}}} = \frac{3}{2}\frac{k_{\mathrm{B}}T}{\gamma_0 a}Kx_{\mathrm{a}} + \cdots, \tag{4.27}$$

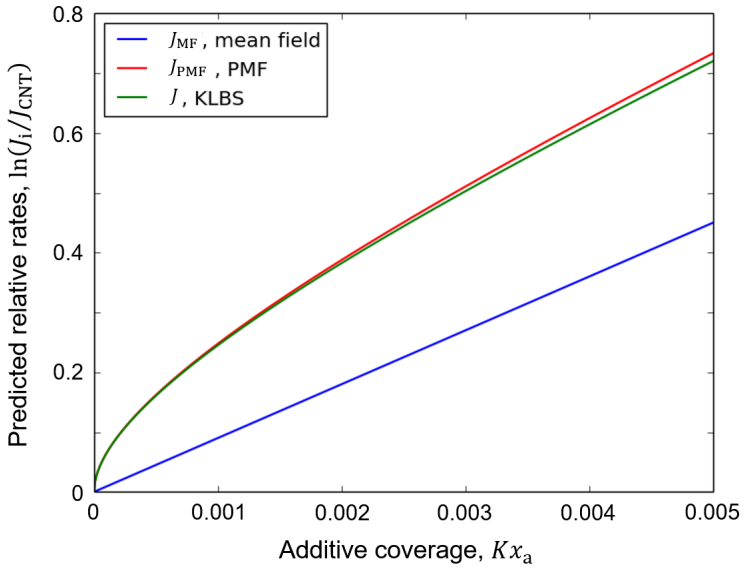

Figure 4.11: Predicted rate relative to the no-additive rate as a function of average additive coverage ($\langle\theta\rangle = Kx_a$) using three levels of theory of increasing accuracy: the mean-field free energy (blue), the PMF along the size coordinate (red), and the KLBS theory result that uses PMF with Zeldovich and reaction coordinate corrections (green). We use the same parameters used in Figure 4.2 except for $\langle\theta\rangle$. Mean field models under-predict the effect of additives on the rate.

where Z_{PMF} and Z_{CNT} is the Zeldovich factor when additives are and are not added. The ratio of rates is

$$\ln \frac{J_{\mathrm{PMF}}}{J_{\mathrm{CNT}}} = \ln \frac{Z_{\mathrm{PMF}}}{Z_{\mathrm{CNT}}} - \left[\frac{\Delta F^{\ddagger}_{\mathrm{PMF}}}{k_{\mathrm{B}}T} - \frac{\Delta F^{\ddagger}_{\mathrm{CNT}}}{k_{\mathrm{B}}T} \right], \tag{4.28}$$

where J_{CNT} is the rate when no additives are added. It is important to note that even small errors in predicted barriers are exponentiated in rate calculations. This causes mean-field models to yield large errors in predicted rates (see Figure 4.11). However, Equation 4.27 and Figure 4.11 show that changes in the Zeldovich factor have a much less pronounced effect on the rate and can be ignored if the barrier is very large (i.e. $\Delta F^{\ddagger}_{\mathrm{CNT}} \gg k_{\mathrm{B}}T$).

Equation 4.28 predicts the rate by assuming nucleus size is the reaction coordinate and projecting the free energy and dynamics onto the n-coordinate. Many studies of

nucleation in other systems have suggested that nucleus size alone is an adequate reaction coordinate.[58,66,75,82,83,90–94] However, these were analyses of single component nucleation without additives. It is unclear whether the extremely slow adsorption of trace additives needs to be explicity accounted for to properly model the dynamics. Here, we model the effect of additives on the rate without assuming nucleus size is the reaction coordinate a priori.

The rate can be calculated directly from the two-dimensional landscape using Kramers-Langer theory.[95–97] The theory requires a quadratic expansion of the free energy surface at the saddle point $(n_\ddagger, m_\ddagger)$:

$$\Delta F(n,m) \approx \Delta F(n_\ddagger, m_\ddagger) + \frac{1}{2} \begin{bmatrix} \delta n \\ \delta m \end{bmatrix}^{\mathrm{T}} \mathbf{H}_\ddagger \begin{bmatrix} \delta n \\ \delta m \end{bmatrix}, \tag{4.29}$$

where $\delta n \equiv n - n_\ddagger$, $\delta m \equiv m - m_\ddagger$, and $\mathbf{H}_\ddagger$ is the second derivative matrix. Kramers-Langer theory also requires the mobility tensor near the saddle point $\mathbf{M}_\ddagger$ to describe the diffusive dynamics along each coordinate. The mobilities along the m and n-coordinates are the attachment frequencies of additives and solutes onto the nucleus. If we assume uncoupled diffusion-controlled attachment, the mobility tensor is

$$\mathbf{M}_\ddagger = 4\pi R_\ddagger^2 \, \frac{D_\mathrm{s} c_\mathrm{s}}{R_\ddagger} \begin{bmatrix} 1 & 0 \\ 0 & D_\mathrm{a} c_\mathrm{a} / D_\mathrm{s} c_\mathrm{s} \end{bmatrix}, \tag{4.30}$$

where D_a and D_s are the diffusion constants of the additive and solute, c_a and c_s are the concentration of additive and solute, and $4\pi R_\ddagger D_\mathrm{s} c_\mathrm{s}$ is the attachment frequency of solutes for compact spherical nuclei with a critical radii of $R_\ddagger$. The absolute value of the attachment frequency is unimportant for our anyalsis but can be estimated using

simulations.[75,98–101] The steady-state nucleation rate is then

$$J = \frac{c_{\mathrm{s}}}{2\pi}\lambda \left|\det\left[\frac{\mathbf{H}_{\ddagger}}{2\pi k_{\mathrm{B}}T}\right]\right|^{-1/2} \exp\left[-\frac{\Delta F(n_{\ddagger}, m_{\ddagger})}{k_{\mathrm{B}}T}\right]. \tag{4.31}$$

where $-\lambda$ is the negative eigenvalue that corresponds to the lone unstable eigenvector of $\mathbf{M}_{\ddagger}\mathbf{H}_{\ddagger}$.[?] For low additive concentrations (i.e. $D_{\mathrm{a}}c_{\mathrm{a}}/D_{\mathrm{s}}c_{\mathrm{s}} \ll 1$),

$$\begin{aligned}\lambda \quad &\approx -\frac{4\pi R_{\ddagger} D_{\mathrm{s}} c_{\mathrm{s}}}{k_{\mathrm{B}}T}\left(\frac{\partial^2 \Delta F}{\partial n^2}\right)_{\ddagger} \\ &\approx \left(\frac{4\pi R_{\ddagger} D_{\mathrm{s}} c_{\mathrm{s}}}{k_{\mathrm{B}}T}\right)\left(\frac{2a\phi\gamma_0}{9n_{\ddagger}^{4/3}}\right)\left[1 - \frac{3k_{\mathrm{B}}T}{a\gamma_0}Kx_{\mathrm{a}} + \cdots\right].\end{aligned} \tag{4.32}$$

Equation 4.31 is slightly different from Langer's result. Langer's rate expression is for the decay of the metastable state which includes the entire reactant basin (or all small nuclei commonly found in the metastable solution). It is often used when the free energy landscape has *largest* nucleus size as a coordinate. However, our landscape is built using CNT which uses population ratios of nuclei of different sizes. By redefining the reactant state as $(m, n) = (0, 1)$, J in Equation 4.31 is the rate that uncovered solute monomers grow.

In the spirit of variational transition theory (a theory which owes much to the work of Bruce Garrett), Berezhkovskii and Szabo demonstrated that the rate calculated using the PMF along the coordinate that minimizes the rate is identical to the Langer result in Equation 4.31.[97] That coordinate is both the eigenvector $\mathbf{u}$ of $\mathbf{H}_{\ddagger}\mathbf{M}_{\ddagger}$ and the true reaction coordinate. For small coverages (see Figure 4.12),

$$\mathbf{u} \approx \left[\frac{a\gamma_0\phi}{3k_{\mathrm{B}}Tn_{\ddagger}^{1/3}}\left(1 - \left(1 + \frac{3k_{\mathrm{B}}T}{a\gamma_0}\right)Kx_{\mathrm{a}} + \cdots\right),\ 1\right]^{\mathrm{T}}. \tag{4.33}$$

The reaction coordinate deviates from the minimum free energy path and tilts toward

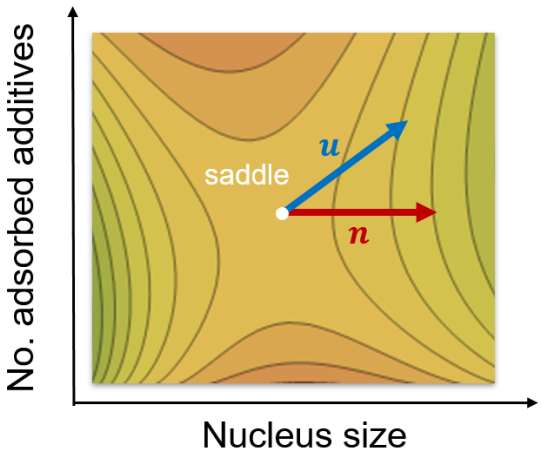

Figure 4.12: Diagram of the reaction coordinate u relative to the nucleus size coordinate n.

the slow coordinate (i.e. number of adsorbed additives). Estimating rates using the PMF along an arbitrary coordinate $\mathbf{e}$ will either overestimate the true rate or equal it if $\mathbf{e} = \mathbf{u}$. This begs an important question: can rates be reasonably estimated if only a PMF along the size coordinate (not $\mathbf{u}$) is used?

The ratio of the true rate and the estimated rate is calculated using Berezhkovskii-Szabo theory and the size PMF:

$$\frac{J}{J_{\mathrm{PMF}}} = \lambda \left(\frac{\mathbf{n}^{\mathrm{T}} \mathbf{M}_{\ddagger} \mathbf{n}}{\left| \mathbf{n}^{\mathrm{T}} \mathbf{H}_{\ddagger}^{-1} \mathbf{n} \right|} \right)^{-1}, \tag{4.34}$$

where $\mathbf{n} = [1, 0]^T$ points along the size coordinate. When additive coverage is small, the ratio simplifies to

$$\frac{J}{J_{\mathrm{PMF}}} = 1 - \frac{2 k_{\mathrm{B}} T}{a \gamma_0} K x_{\mathrm{a}} + \cdots . \tag{4.35}$$

Equation 4.35 shows that reasonably accurate rate predictions can be obtained from a one-dimensional analysis using the size PMF as long as additive coverage is low and the barrier is high (i.e. $\Delta F_{\mathrm{CNT}}^{\ddagger} \gg k_{\mathrm{B}} T$). This is also demonstrated in Figure 4.11. This

suggests that simulations likely do not have to explicitly account for the dynamics of additive adsorption when investigating the effect of additives, which will be both simpler and less expensive than a full two-dimensional study.

It is interesting to note that Berezhkovskii-Szabo theory still holds in this example of severe anisotropic mobility. Berezhkovskii and Zitserman showed that, in the anomalous regime where mobility is severely anisotropic, dynamical trajectories typically avoid the saddle because the slow coordinate is "frozen." [102,103] However, in this special case, both the position of the saddle and the relative mobility are proportional to the concentration of additives. So as the relative mobility along the m-direction approaches zero, the minimum free energy path becomes more like the no additive case where trajectories moving only in the n-direction pass through the saddle.

4.5 Conclusion

This work develops a theoretical model for the thermodynamics and kinetics of nucleation in the presence of additives that bind to the surface of nuclei. We combined elements of classical nucleation theory with a statistical model for Langmuir adsorbtion to derive the free energy as a function of nucleus size and additive coverage. The predicted relationship between the free energy barrier and additive concentration is consistent with our semigrand Monte Carlo simulations of a ternary Potts lattice gas model. We also showed that increasing the additive-solute interaction strength (or binding strength) corresponded to an increase in the Langmuir constant, a decrease in the surface energy of a nucleus at fixed additive concentration, and therefore a decrease in the nucleation barrier. Therefore, we expect stronger adsorbing surfactants to be better nucleation promoters.

We also developed a simple dynamical model for diffusion controlled attachment of additives and solutes to nuclei. The model accounts for both the size and dynamics

of fluctuations in coverage during the nucleation process and computes rates using a multidimensional Zeldovich-Frenkel equation similar to Langer theory. We compare those rates to those computed using free energy barriers of free energy landscapes projected onto the nucleus size coordinate using Kramers-Langer-Berezhkovskii-Szabo theory. This calculation essentially computes the error in the rate if we ignore the dynamics of the additive adsorption process.

Simple and convenient mean-field models capture most of the trends, and they may help devise experiments to screen for potent nucleants. However, the mean-field calculation ignores the effects of fluctuating coverage, and these effects are significant when the mean coverage is small. The potential of mean force includes the effects of additive coverage fluctuations, and thus barriers and rates from the potential of mean force are more accurate for sparse additive coverages. The full two-dimensional rate calculation captures the dynamics of additive adsorption, but it gives results which are similar to the potential of mean force calculation for small additive concentrations. We show that the potential of mean force model accurately collapses all of our simulation results whereas their previous mean field model did not. This suggests that the new model may help interpret the kinetics of nucleation in the presence of additives that bind to the precipitate surfaces.

The hope is that this work will inspire

- Theoretical modeling of experimental nucleation rates for different surface-adsorbing additives at different concentrations. Unlike empirical models, our theoretical framework relates changes in nucleation rates to physically meaningful parameters, such as additive concentration and adsorption constant. The effective adsorption constant obtained from a fit of rate versus concentration data can be used as a figure of merit that quantifies the effectiveness of different additives at accelerating

nucleation. It can also be used to verify if this simple adsorption mechanism is consistent with the observed kinetics trends.

- High-throughput screening of nucleants. Our model predicts that stronger binding additives are more effective nucleants. Binding coefficients can be computed much faster using either molecular dynamics or electronic structure calculations than nucleation barriers. Even if our model is not quantitatively accurate, the qualitative trend it predicts can be used to rank promoters from least to most effective. This can help experiments prioritize their investigation to the most promising promoters.

While we may be years away from these goals, we feel this work is an important first step in improving how we understand and discover molecular-scale nucleants.

Bibliography

[1] A. Hudait and V. Molinero, *Ice crystallization in ultrafine water-salt aerosols: Nucleation, ice-solution equilibrium, and internal structure*, *J. Am. Chem. Soc.* **136** (2014), no. 22 8081–8093.

[2] G. Bullock and V. Molinero, *Low-density liquid water is the mother of ice: on the relation between mesostructure, thermodynamics and ice crystallization in solutions*, *Faraday Discuss.* **167** (2013) 371–388.

[3] C. Budke, A. Dreyer, J. Jaeger, K. Gimpel, T. Berkemeier, A. S. Bonin, L. Nagel, C. Plattner, A. L. DeVries, N. Sewald, and T. Koop, *Quantitative efficacy classification of ice recrystallization inhibition agents*, *Cryst. Growth Des.* **14** (2014), no. 9 4285–4294.

[4] P. A. Alpert, J. Y. Aller, and D. A. Knopf, *Ice nucleation from aqueous nacl droplets with and without marine diatoms*, *Atmos. Chem. Phys.* **11** (2011), no. 12 5539–5555.

[5] T. Koop and B. Zobrist, *Parameterizations for ice nucleation in biological and atmospheric systems*, *Phys. Chem. Chem. Phys.* **11** (2009), no. 46 10839–10850.

[6] R. J. Davey, N. Blagden, G. D. Potts, and R. Docherty, *Polymorphism in molecular crystals: Stabilization of a metastable form by conformational mimicry*, *J. Am. Chem. Soc.* **119** (1997), no. 7 1767–1772.

[7] N. Blagden and R. J. Davey, *Polymorph selection: Challenges for the future?*, *Cryst. Growth Des.* **3** (2003), no. 6 873–885.

[8] A. Llinas and J. M. Goodman, *Polymorph control: past, present and future*, *Drug Discovery Today* **13** (2008), no. 5-6 198–210.

[9] V. Pipich, M. Balz, S. E. Wolf, W. Tremel, and D. Schwahn, *Nucleation and growth of caco(3) mediated by the egg-white protein ovalbumin: A time-resolved in situ study using small-angle neutron scattering*, *J. Am. Chem. Soc.* **130** (2008), no. 21 6879–6892.

[10] Y. Levi, S. Albeck, A. Brack, S. Weiner, and L. Addadi, *Control over aragonite crystal nucleation and growth: An in vitro study of biomineralization*, *Chem. Eur. J.* **4** (1998), no. 3 389–396.

[11] M. F. Butler, N. Glaser, A. C. Weaver, M. Kirkland, and M. Heppenstall-Butler, *Calcium carbonate crystallization in the presence of biopolymers*, *Cryst. Growth Des.* **6** (2006), no. 3 781–794.

[12] F. C. Meldrum and H. Coelfen, *Controlling mineral morphologies and structures in biological and synthetic systems*, *Chem. Rev.* **108** (2008), no. 11 4332–4432.

[13] K. Naka and Y. Chujo, *Control of crystal nucleation and growth of calcium carbonate by synthetic substrates*, *Chem. Mater.* **13** (2001), no. 10 3245–3259.

[14] S. Elhadj, J. J. De Yoreo, J. R. Hoyer, and P. M. Dove, *Role of molecular charge and hydrophilicity in regulating the kinetics of crystal growth*, *Proc. Natl. Acad. Sci. U. S. A.* **103** (2006), no. 51 19237–19242.

[15] D. Gebauer, H. Coelfen, A. Verch, and M. Antonietti, *The multiple roles of additives in caco3 crystallization: A quantitative case study*, *Advanced Materials* **21** (2009), no. 4 435–439.

[16] D. C. Popescu, M. M. J. Smulders, B. P. Pichon, N. Chebotareva, S.-Y. Kwak, O. L. J. van Asselen, R. P. Sijbesma, E. DiMasi, and N. A. J. M. Sommerdijk, *Template adaptability is key in the oriented crystallization of caco(3)*, *J. Am. Chem. Soc.* **129** (2007), no. 45 14058–14067.

[17] C. Brinker and G. Scherer, *Sol-gel Science: The Physics and Chemistry of Sol-gel Processing*. Academic Press, 1990.

[18] R. F. Lobo, S. I. Zones, and M. E. Davis, *Structure-direction in zeolite synthesis*, *J. Inclusion Phenom. Mol. Recognit. Chem.* **21** (1995), no. 1-4 47–78.

[19] Q. S. Huo, D. I. Margolese, and G. D. Stucky, *Surfactant control of phases in the synthesis of mesoporous silica-based materials*, *Chem. Mater.* **8** (1996), no. 5 1147–1160.

[20] Y. Kubota, M. M. Helmkamp, S. I. Zones, and M. E. Davis, *Properties of organic cations that lead to the structure-direction of high-silica molecular sieves*, *Microporous Materials* **6** (1996), no. 4 213–229.

[21] O. Galkin and P. G. Vekilov, *Control of protein crystal nucleation around the metastable liquid-liquid phase boundary*, *Proc. Natl. Acad. Sci. U. S. A.* **97** (2000), no. 12 6277–6281.

[22] P. G. Vekilov, *Nucleation*, *Cryst. Growth Des.* **10** (2010), no. 12 5007–5019.

[23] V. Y. Torbeev, E. Shavit, I. Weissbuch, L. Leiserowitz, and M. Lahav, *Control of crystal polymorphism by tuning the structure of auxiliary molecules as nucleation inhibitors. the beta-polymorph of glycine grown in aqueous solutions*, *Cryst. Growth Des.* **5** (2005), no. 6 2190–2196.

[24] R. P. Sear, *Nucleation of the crystalline phase of proteins in the presence of semidilute nonadsorbing polymer*, *J. Chem. Phys.* **115** (2001), no. 1 575–579.

[25] B. J. Anderson, J. W. Tester, G. P. Borghi, and B. L. Trout, *Properties of inhibitors of methane hydrate formation via molecular dynamics simulations*, *J. Am. Chem. Soc.* **127** (2005), no. 50 17852–17862.

[26] M. T. Storr, P. C. Taylor, J. P. Monfort, and P. M. Rodger, *Kinetic inhibitor of hydrate crystallization*, *J. Am. Chem. Soc.* **126** (2004), no. 5 1569–1576.

[27] A. K. Sum, C. A. Koh, and E. D. Sloan, *Clathrate hydrates: From laboratory science to engineering practice*, *Ind. Eng. Chem. Res.* **48** (2009), no. 16 7457–7465.

[28] J. S. Zhang, S. Lee, and J. W. Lee, *Kinetics of methane hydrate formation from sds solution*, *Ind. Eng. Chem. Res.* **46** (2007), no. 19 6353–6359.

[29] J. S. Zhang, C. Lo, P. Somasundaran, S. Lu, A. Couzis, and J. W. Lee, *Adsorption of sodium dodecyl sulfate at thf hydrate/liquid interface*, *J. Phys. Chem. C* **112** (2008), no. 32 12381–12385.

[30] A. Fazlali, S.-A. Kazemi, M. Keshavarz-Moraveji, and A. H. Mohammadi, *Impact of different surfactants and their mixtures on methane-hydrate formation*, *Energy Technology* **1** (2013), no. 8 471–477.

[31] S.-Q. Hao, S. Kim, Y. Qin, and X.-H. Fu, *Enhanced methane hydrate storage using sodium dodecyl sulfate and coal*, *Environ. Chem. Lett.* **12** (2014), no. 2 341–346.

[32] H. X. Yuan and J. M. Ouyang, *Chemical basis in inhibition of urinary stones by tartaric acid and its salts*, *Progress in Chemistry* **18** (2006), no. 5 573–578.

[33] J. D. Rimer, Z. An, Z. Zhu, M. H. Lee, D. S. Goldfarb, J. A. Wesson, and M. D. Ward, *Crystal growth inhibitors for the prevention of l-cystine kidney stones through molecular design*, *Science* **330** (2010), no. 6002 337–341.

[34] A. L. Devries, *Glycoproteins as biological antifreeze agents in antarctic fishes*, *Science* **172** (1971), no. 3988 1152–&.

[35] J. G. Duman, *Antifreeze and ice nucleator proteins in terrestrial arthropods*, *Annu. Rev. Physiol.* **63** (2001) 327–357.

[36] F. Sicheri and D. S. C. Yang, *Ice-binding structure and mechanism of an antifreeze protein from winter flounder*, *Nature* **375** (1995), no. 6530 427–431.

[37] D. Kashchiev and G. M. van Rosmalen, *Review: Nucleation in solutions revisited*, *Cryst. Res. Technol.* **38** (2003), no. 7-8 555–574.

[38] D. Kashchiev, *Nucleation: Basic Theory With Applications*. Butterworth-Heinemann, Oxford, 2000.

[39] I. Weissbuch, M. Lahav, and L. Leiserowitz, *Toward stereochentical control, monitoring, and understanding of crystal nucleation*, *Cryst. Growth Des.* **3** (2003), no. 2 125–150.

[40] I. Weissbuch, V. Y. Torbeev, L. Leiserowitz, and M. Lahav, *Solvent effect on crystal polymorphism: Why addition of methanol or ethanol to aqueous solutions induces the precipitation of the least stable beta form of glycine*, *Angew. Chem. Int. Ed.* **44** (2005), no. 21 3226–3229.

[41] L. N. Poloni and M. D. Ward, *The materials science of pathological crystals*, *Chem. Mater.* **26** (2014), no. 1 477–495.

[42] J. Anwar, P. K. Boateng, R. Tamaki, and S. Odedra, *Mode of action and design rules for additives that modulate crystal nucleation*, *Angew. Chem. Int. Ed.* **48** (2009), no. 9 1596–1600.

[43] N. Duff, Y. R. Dahal, J. D. Schmit, and B. Peters, *Salting out the polar polymorph: Analysis by alchemical solvent transformation*, *J. Chem. Phys.* **140** (2014), no. 1 014501.

[44] R. Becker and W. Doring, *Kinetic treatment of grain-formation in super-saturated vapours*, *Annalen der Physik* **24** (1935), no. 8 719–752.

[45] M. Volmer and A. Weber, *Nuclei formation in supersaturated states*, *Z. Phys. Chem.* **119** (1926) 277–301.

[46] J. Frenkel, *Kinetic Theory of Liquids*. Dover Publications. Dover, 1955.

[47] V. Agarwal and B. Peters, *Precipitate Nucleation: A Review of Theory and Simulation Advances*, vol. 155 of *Advances in Chemical Physics*. John Wiley & Sons, New Jersey, USA, 2014.

[48] S. L. Girshick, *Comment on: Self consistency correction to homogeneous nucleation theory*, *The Journal of Chemical Physics* **94** (1991), no. 1 826–827.

[49] S. L. Girshick and C.-P. Chiu, *Kinetic nucleation theory: A new expression for the rate of homogeneous nucleation from an ideal supersaturated vapor*, *The Journal of Chemical Physics* **93** (1990), no. 2 1273–1277.

[50] T. Hill, *An Introduction to Statistical Thermodynamics*. Addison-Wesley series in chemistry. Dover Publications, 1960.

[51] G. G. Poon, S. Seritan, and B. Peters, *Fd nucleation: A design equation for low dosage additives that accelerate nucleation*, *Faraday Discussions* (2015).

[52] M. A. L. J. Fransen, J. Hruby, D. M. J. Smeulders, and M. E. H. van Dongen, *On the effect of pressure and carrier gas on homogeneous water nucleation*, *Journal of Chemical Physics* **142** (2015), no. 16 64307–64307.

[53] K. Binder and H. Muller-Krumbhaar, *Investigation of metastable states and nucleation in kinetic ising-model*, *Phys. Rev. B* **9** (1974), no. 5 2328–2353.

[54] D. Stauffer, A. Coniglio, and D. W. Heermann, *Monte-carlo experiment for nucleation rate in the 3-dimensional ising-model*, *Phys. Rev. Lett.* **49** (1982), no. 18 1299–1302.

[55] J. Schmelzer and D. P. Landau, *Monte carlo simulation of nucleation and growth in the 3d nearest-neighbor ising model*, *International Journal of Modern Physics C* **12** (2001), no. 3 345–359.

[56] V. A. Shneidman, K. A. Jackson, and K. M. Beatty, *On the applicability of the classical nucleation theory in an ising system*, *J. Chem. Phys.* **111** (1999), no. 15 6932–6941.

[57] F. Schmitz, P. Virnau, and K. Binder, *Monte carlo tests of nucleation concepts in the lattice gas model*, *Phys. Rev. E* **87** (2013), no. 5 053302.

[58] A. C. Pan and D. Chandler, *Dynamics of nucleation in the ising model*, *J. Phys. Chem. B* **108** (2004), no. 51 19681–19686.

[59] R. P. Sear, *Heterogeneous and homogeneous nucleation compared: Rapid nucleation on microscopic impurities*, *J. Phys. Chem. B* **110** (2006), no. 10 4985–4989.

[60] R. P. Sear, *Non-self-averaging nucleation rate due to quenched disorder*, *J. Phys.: Condens. Matter* **24** (2012), no. 5 052205.

[61] A. J. Page and R. P. Sear, *Heterogeneous nucleation in and out of pores*, *Phys. Rev. Lett.* **97** (2006), no. 6 065701.

[62] F. Y. Wu, *Dilute potts-model, duality and site-bond percolation*, *J. Phys. A: Math. Gen.* **14** (1981), no. 2 L39–L44.

[63] F. Y. Wu, *The potts-model*, *Reviews of Modern Physics* **54** (1982), no. 1 235–268.

[64] R. Devanathan, L. Van Brutzel, A. Chartier, C. Gueneau, A. E. Mattsson, V. Tikare, T. Bartel, T. Besmann, M. Stan, and P. Van Uffelen, *Modeling and simulation of nuclear fuel materials*, *Energy & Environmental Science* **3** (2010), no. 10 1406–1426.

[65] V. Tikare, E. A. Holm, D. Fan, and L. Q. Chen, *Comparison of phase-field and potts models for coarsening processes*, *Acta Mater.* **47** (1998), no. 1 363–371.

[66] N. Duff and B. Peters, *Nucleation in a potts lattice gas model of crystallization from solution*, *J. Chem. Phys.* **131** (2009), no. 18 184101.

[67] V. Agarwal and B. Peters, *Nucleation near the eutectic point in a potts-lattice gas model*, *J. Chem. Phys.* **140** (2014), no. 8 084111.

[68] D. Bellucci, V. Cannillo, and A. Sola, *Monte carlo simulation of microstructure evolution in biphasic-systems*, *Ceram. Int.* **36** (2010), no. 6 1983–1988.

[69] L. O. Hedges and S. Whitelam, *Selective nucleation in porous media*, *Soft Matter* **9** (2013), no. 41 9763–9766.

[70] J. Grant, R. L. Jack, and S. Whitelam, *Analyzing mechanisms and microscopic reversibility of self-assembly*, *J. Chem. Phys.* **135** (2011), no. 21 214505.

[71] W. M. Jacobs, D. W. Oxtoby, and D. Frenkel, *Phase separation in solutions with specific and nonspecific interactions*, *J. Chem. Phys.* **140** (2014), no. 20 204109.

[72] T. K. Haxton and S. Whitelam, *Do hierarchical structures assemble best via hierarchical pathways?*, *Soft Matter* **9** (2013), no. 29 6851–6861.

[73] N. Duff and B. Peters, *Nucleation in a potts lattice gas model of crystallization from solution (vol 131, 184101, 2009)*, *J. Chem. Phys.* **132** (2010), no. 12 129901.

[74] B. C. Knott, M. F. Doherty, and B. Peters, *A simulation test of the optical kerr mechanism for laser-induced nucleation*, *J. Chem. Phys.* **134** (2011), no. 15 154501.

[75] B. C. Knott, N. Duff, M. F. Doherty, and B. Peters, *Estimating diffusivity along a reaction coordinate in the high friction limit: Insights on pulse times in laser-induced nucleation*, *J. Chem. Phys.* **131** (2009), no. 22 224112.

[76] D. Reguera, R. K. Bowles, Y. Djikaev, and H. Reiss, *Phase transitions in systems small enough to be clusters*, *J. Chem. Phys.* **118** (2003), no. 1 340–353.

[77] R. Grossier and S. Veesler, *Reaching one single and stable critical cluster through finite-sized systems*, *Cryst. Growth Des.* **9** (2009), no. 4 1917–1922.

[78] J. Wedekind, D. Reguera, and R. Strey, *Finite-size effects in simulations of nucleation*, *J. Chem. Phys.* **125** (2006), no. 21 214505.

[79] A. S. Abyzov and J. W. P. Schmelzer, *Kinetics of segregation processes in solutions: Saddle point versus ridge crossing of the thermodynamic potential barrier*, *J. Non-Cryst. Solids* **384** (2014) 8–14.

[80] R. Ni, F. Smallenburg, L. Filion, and M. Dijkstra, *Crystal nucleation in binary hard-sphere mixtures: the effect of order parameter on the cluster composition*, *Mol. Phys.* **109** (2011), no. 7-10 1213–27.

[81] D. A. Kofke and E. D. Glandt, *Monte-carlo simulation of multicomponent equilibria in a semigrand canonical ensemble*, *Mol. Phys.* **64** (1988), no. 6 1105–1131.

[82] L. Maibaum, *Comment on "elucidating the mechanism of nucleation near the gas-liquid spinodal"*, *Phys. Rev. Lett.* **101** (2008), no. 1 019601.

[83] L. Maibaum, *Phase transformation near the classical limit of stability*, *Phys. Rev. Lett.* **101** (2008), no. 25 256102.

[84] G. M. Torrie and J. P. Valleau, *Non-physical sampling distributions in monte-carlo free-energy estimation - umbrella sampling*, *J. Comput. Phys.* **23** (1977), no. 2 187–199.

[85] S. Kumar, D. Bouzida, R. H. Swendsen, P. A. Kollman, and J. M. Rosenberg, *The weighted histogram analysis method for free-energy calculations on biomolecules .1. the method*, *J. Comput. Chem.* **13** (1992), no. 8 1011–1021.

[86] S. Auer and D. Frenkel, *Quantitative prediction of crystal-nucleation rates for spherical colloids: A computational approach*, *Annu. Rev. Phys. Chem.* **55** (2004) 333–361.

[87] M. Salvalaglio, T. Vetter, M. Mazzotti, and M. Parrinello, *Controlling and predicting crystal shapes: The case of urea*, *Angew. Chem. Int. Ed.* **52** (2013), no. 50 13369–13372.

[88] B. Roux, *The calculation of the potential of mean force using computer-simulations*, *Comput. Phys. Commun.* **91** (1995), no. 1-3 275–282.

[89] P. Rinaldi, F. Bulnes, A. J. Ramirez-Pastor, and G. Zgrablich, *Monte carlo study of multicomponent adsorption on triangular lattices*, *Surf. Sci.* **602** (2008), no. 10 1783–1794.

[90] S. Auer and D. Frenkel, *Prediction of absolute crystal-nucleation rate in hard-sphere colloids*, *Nature* **409** (2001), no. 6823 1020–1023.

[91] S. Punnathanam and P. A. Monson, *Crystal nucleation in binary hard sphere mixtures: A monte carlo simulation study*, *J. Chem. Phys.* **125** (2006), no. 2 024508.

[92] S. L. Meadley and F. A. Escobedo, *Thermodynamics and kinetics of bubble nucleation: Simulation methodology*, *J. Chem. Phys.* **137** (2012), no. 7 074109.

[93] I. Saika-Voivod, P. H. Poole, and R. K. Bowles, *Test of classical nucleation theory on deeply supercooled high-pressure simulated silica*, *J. Chem. Phys.* **124** (2006), no. 22 224709.

[94] E. Sanz, C. Vega, J. R. Espinosa, R. Caballero-Bernal, J. L. F. Abascal, and C. Valeriani, *Homogeneous ice nucleation at moderate supercooling from molecular simulation*, *J. Am. Chem. Soc.* **135** (2013), no. 40 15008–15017.

[95] J. Langer, *Statistical theory of the decay of metastable states*, *Annals of Physics* **54** (1969), no. 2 258–275.

[96] H. Weidenmüller and Z. Jing-Shang, *Stationary diffusion over a multidimensional potential barrier: A generalization of kramers' formula*, *Journal of statistical physics* **34** (1984), no. 1-2 191–201.

[97] A. Berezhkovskii and A. Szabo, *One-dimensional reaction coordinates for diffusive activated rate processes in many dimensions*, *The Journal of Chemical Physics* **122** (2005), no. 1 –.

[98] B. C. Knott, V. Molinero, M. F. Doherty, and B. Peters, *Homogeneous nucleation of methane hydrates: Unrealistic under realistic conditions*, *J. Am. Chem. Soc.* **134** (2012), no. 48 19544–19547.

[99] B. Peters and B. L. Trout, *Obtaining reaction coordinates by likelihood maximization*, *J. Chem. Phys.* **125** (2006), no. 5.

[100] A. Ma and A. R. Dinner, *Automatic method for identifying reaction coordinates in complex systems*, *The Journal of Physical Chemistry B* **109** (2005), no. 14 6769–6779.

[101] E. E. Borrero and F. A. Escobedo, *Reaction coordinates and transition pathways of rare events via forward flux sampling*, *The Journal of chemical physics* **127** (2007), no. 16 164101.

[102] A. Berezhkovskii and V. Y. Zitserman, *Anomalous regime for decay of the metastable state: An extension of multidimensional kramers theory*, *Chemical Physics Letters* **158** (1989), no. 5 369–374.

[103] A. M. Berezhkovskii, A. Szabo, N. Greives, and H.-X. Zhou, *Multidimensional reaction rate theory with anisotropic diffusion*, *The Journal of Chemical Physics* **141** (2014), no. 20 –.

Chapter 5

Accelerating solute nucleation with adsorbing oligomeric chains

5.1 Introduction

Solute precipitate nucleation is often influenced by species other than the solute and the solvent, including small molecules,[1–5] salts,[6,7] surfactants,[8–11] peptides,[12] and impurities.[13,14] Polymeric additives (e.g. PEG, PVP, HPMC, and PVA) have also been experimentally shown to enhance or inhibit the nucleation of proteins and small molecule drugs[15–17], lower or raise the freezing temperature of water,[18,19] and selectively control polymorph selection during $CaCO_3$ nucleation and crystallization.[20,21] An understanding of the mechanisms by which these species influence nucleation rates might guide the development of tailor designed additives to modify nucleation rates or to selectively promote nucleation of certain polymorphs.[1,15,22]

Reproduced in part with permission from Poon, G. G., Lemke, T., Peter, C., Molinero, V., and Peters, B. (2017). "Oligomeric Nucleants: Simulations of Chain Length, Binding Strength, and Volume Fraction Effects." The Journal of Physical Chemistry Letters.

Efforts to model the effects of additives began with Sangwal's semi-empirical models of metastable zone widths.[23,24] Anwar et al. discovered that additive size and interaction strength with solutes are important design variables for a promoter and inhibitor.[25] Their simulations of ternary Lennard-Jones systems showed that amphiphilic additives with a strong attraction to the nuclei surface decreased the waiting time for solute cluster formation. Poon et al.[26,27] and van Dongen et al.[28,29] combined Langmuir adsorption and classical nucleation theory (CNT) to show how adsorbing additives lower the surface free energy and accelerate nucleation. These theoretical models showed that stronger surface-binding additives are more effective promoters and predicted specific trends in free energy barriers.

The model from our previous work is not applicable to oligomeric nucleants because their adsorption onto surfaces does not follow a Langmuir isotherm. In this work, we consider the effects of oligomeric additives where each segment of the adsorbing chain can bind to unoccupied surface sites on the nuclei. The nucleation rate J is

$$J = A \exp\left[-\beta \Delta F^{\ddagger}\right], \tag{5.1}$$

where A is a pre-exponential factor, $\beta = 1/k_B T$, and $\Delta F^{\ddagger}$ is the maximum of the free energy as a function of nucleus size. According to CNT, A is proportional to the attachment frequency. $\Delta F^{\ddagger}$ depends on the thermodynamic driving force for nucleation and on the interfacial free energy of the nuclei.[30] Therefore Equation 5.1 suggests that additives can influence nucleation rates in three ways: by changing the thermodynamic driving force, by changing the interfacial free energies of nuclei, or by changing the attachment frequency.[23,31,32] In general, additives must be present in large amounts to alter the thermodynamic driving force (e.g. by changing solubility limits or freezing points), although in some cases they can promote nucleation in very dilute solutions

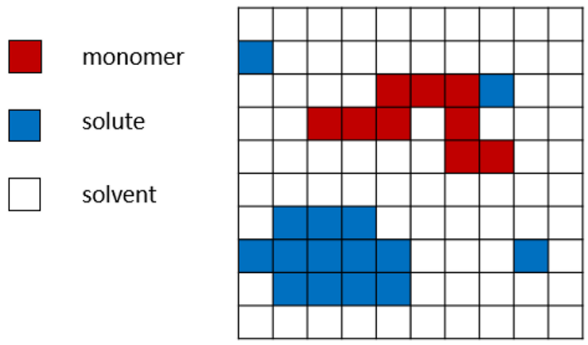

Figure 5.1: A two dimensional representation of our Potts lattice gas model.

by non-ideal mixing effects.[?] In this work, we focus on trace oligomeric additives that lower the interfacial free energy of nuclei by adsorbing to their surfaces. More specifically, we investigate how different conditions (i.e. chain length, volume fraction, and surface attraction) affect $\Delta F^{\ddagger}$ and therefore nucleation rates. We do not consider the effects of additives on solute attachment (i.e. prefactors) because coverages on critical nuclei do not closely approach unity for any conditions examined.

5.2 Simulation details of Potts lattice gas model with oligomeric additive

5.2.1 Hamiltonian

Following previous works,[26,33] we use a ternary Potts lattice gas (PLG) model to reveal generic design principles. The PLG in this work represents a solution with solutes, solvents, and dissolved oligomeric additives. Each site i on the $32 \times 32 \times 32$ cubic lattice has two properties: a type m_i and an orientation s_i. m_i is either 0, 1, or 2 which indicates that the site is occupied by an oligomer segment, solute, or solvent respectively (see Figure 5.2.1). Oligomers occupy a series of N connected lattice sites where N is the

Table 5.1: Pairwise interaction parameter values.

A_{11}	B_{11}	A_{22}	A_{00}	B_{01}	A_{02}
-1.25	-1.25	-1.25	-1.25	-2.5 or -3.0	-1.25

oligomer chain length. In contrast, solutes and solvents only occupy one site. For each occupant, s_i can be one of 24 possible orientations (the number of distinct orientations of a cube), allowing similarly oriented solutes to be more attracted to each other.[34] It also allows non-isotropic oligomer-solute interactions to ensure chains adsorb onto the cluster surface without becoming inclusions in the solute precipitate.

The total energy E is the sum of pairwise interactions U_{m_i,m_j} between nearest-neighbor sites i and j:

$$\beta E = \sum_{\langle i,j \rangle} U_{m_i,m_j}. \tag{5.2}$$

The pair interactions are defined by species-specific and orientation-specific parameters $A_{m_i m_j}$ and $B_{m_i m_j}$, respectively (see Table 5.1):

$$\beta U_{m_i,m_j} = \begin{cases} A_{00} & \text{if } m_i = m_j = 0 \\ A_{11} + \delta_{s_i,s_j} B_{11} & \text{if } m_i = m_j = 1 \\ A_{22} & \text{if } m_i = m_j = 2 \\ \xi_{ij} B_{01} & \text{if } m_i = 0, m_j = 1 \\ A_{02} & \text{if } m_i = 0, m_j = 2 \\ 0 & \text{otherwise} \end{cases} \tag{5.3}$$

where interactions (in order) are between oligomer segments (bonded and non-bonded), between solutes, between solvents, between segments and solutes, and between segments and solvents. All other interactions are zero. The absence of solute-solvent interactions leads to a nearly pure solute precipitate with poor solubility.[34] $\xi_{ij} = 1$ for the 4 orienta-

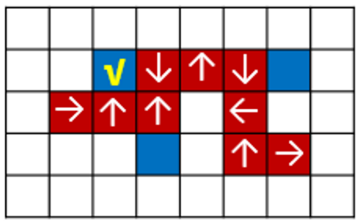

Figure 5.2: A solute (blue) only interacts with an oligomer segment (red) if the segment is "pointing" toward it (white arrow). The yellow check indicates which solutes interact with an oligomer segment.

tions that "point" to neighbor j (see Equation 5.2). Otherwise $\xi_{ij} = 0$. For all pairwise interactions involving at least one solvent site, the energies of these interactions are independent of the orientation of either site. However, even though the orientations of solvent sites do not affect the total energy, explicitly removing their orientations will result in not properly accounting for the energetically degenerate states of the solvent sites. This will lead to an underestimation of the density of states and incorrect free energy values. Therefore, including these rotation moves is necessary to accurately explore the ensemble of states. The absence of solute-solvent interactions leads to a nearly pure solute precipitate with poor solubility.[34] Oligomer segments only interact with solutes it is oriented toward and therefore are weakly soluble in the bulk solute precipitate. We do not expect oligomers to be incorporated in nuclei unless growth is fast and far from equilibrium.[35] $\xi_{ij} = 1$ for the 4 orientations that "point" to neighbor j. Otherwise $\xi_{ij} = 0$. We restrict our study to parameters where the solvent is a good/athermal solvent for the oligomer by setting $A_{00} = A_{22}$ (i.e. Flory parameter χ is zero).[36,37] We also consider cases where B_{01} is large enough that the chains adsorb onto a solute surface. If oligomer segments are not attracted enough to the surface, an oligomer depletion layer forms because the entropic cost to confine the chain to the surface outweighs the enthalpy of adsorption.

5.2.2 Algorithm

We sample the configuration space by accepting or rejecting Monte Carlo (MC) moves according to the Metropolis criteria. Moves include orientation flips, local and non-local swaps between solutes and solvents, and four local polymer moves:[38] end rotation, kink jump, crankshaft, and snake. Semigrand-canonical moves are also used to control the chemical potential driving force for nucleation. In a small closed simulation, the formation of a nucleus artificially depletes the dissolved solute concentration and lowers the driving force, even while nuclei are precritical.[39–42] Therefore solute precipitate nucleation is best simulated using open, grand or semigrand ensembles.[34,43–45] We use Kofke-Glandt[46] semigrand moves to swap solutes and solvents and Müller-Binder[47] semigrand moves to swap oligomers with either solutes or solvents. These moves maintain the chemical potential differences between all three species.

Monte Carlo moves

Figure 5.3 summarizes our semigrand Monte Carlo (SGMC) algorithm. A lattice point is randomly chosen every SGMC move and the randomly chosen move attempt is selected according to the move proposition probabilities p_i, which are chosen to ensure frequent attempts of each move type and a net acceptance rate around 30 to 70%. The values of each p_i should not affect the final results, but only the algorithm's efficiency. The acceptance probability for each move is chosen to enforce detailed balance given the probability the forward and reverse move is attempted.

Orientation flips involve changing the orientation of the occupant of the lattice point i to any one of $Q = 24$ possible orientations:

$$s_i \leftarrow \text{RandInt}[0, 23] \tag{5.4}$$

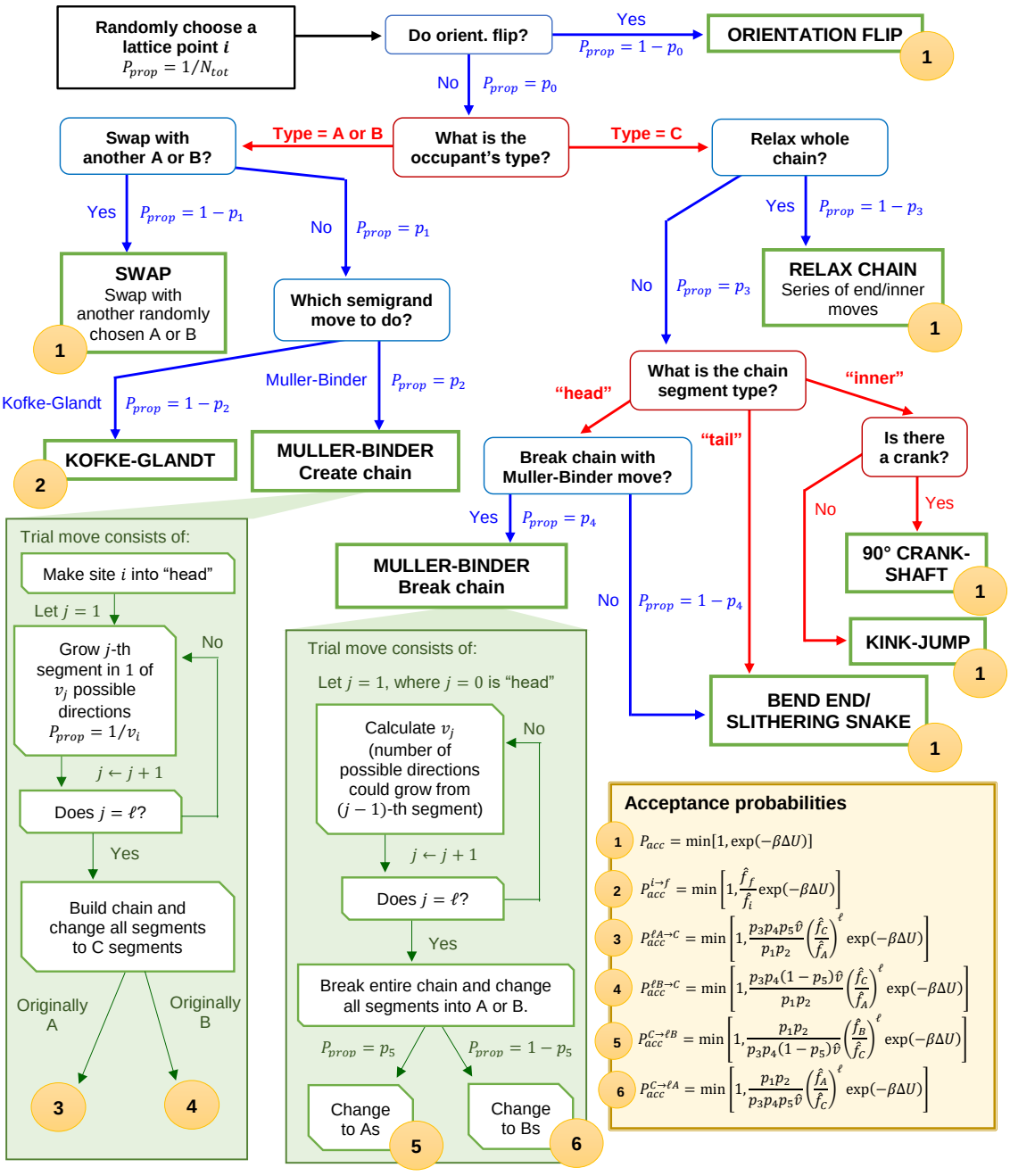

Figure 5.3: Semigrand Monte Carlo algorithm. In our simulations, $p_0 = 0.9$, $p_1 = 0.5$, $p_2 = 0.5$, $p_3 = 0.3$, $p_4 = 0.9$ and $p_5 = 0.1$. The moves are described in the text.

Swaps involve switching the type and orientation of the occupant of lattice point i with those of another randomly chosen lattice point j:

$$\begin{aligned} (m_i, s_i) &\leftarrow (m_j, s_j) \\ (m_j, s_j) &\leftarrow (m_i, s_i). \end{aligned} \tag{5.5}$$

Kofke-Glandt semigrand moves are used to change the identity of the occupant i if it is either a solute ($m_i = 1$) or solvent ($m_i = 2$):

$$m_i \leftarrow \begin{cases} 1 & \text{if } m_i = 2 \\ 2 & \text{if } m_i = 1 \end{cases} \tag{5.6}$$

If it is a solute, it is changed to a solvent. If it is a solvent, it is changed to a solute. These moves are the same as those used in our previous paper [26].

Figure 5.4 show the lattice polymer moves used to explore the many chain conformations. Every chain has two ends: a "head" and a "tail." This distinction is defined immediately after the chain is added. The other segments are labeled "inner" segments. End moves involve swapping an oligomer end with the occupant of a neighboring lattice of the segment currently bonded to the chosen end ("bend end" move) or with the occupant of a a neighboring lattice of the other end ("slithering snake" move). Inner moves include rotating two bonded segments around the axis formed by the vector connecting the two adjacent segments ("crankshaft" move) and moving a kink one segment within the chain ("kink-jump" move). For all lattice polymer moves, the final position of segment(s) must be initially occupied by either a solute or solvent. The moves are accepted according to the traditional Metropolis criteria. [48]

Müller-Binder semigrand moves are used to change the identity of a chain of connect-

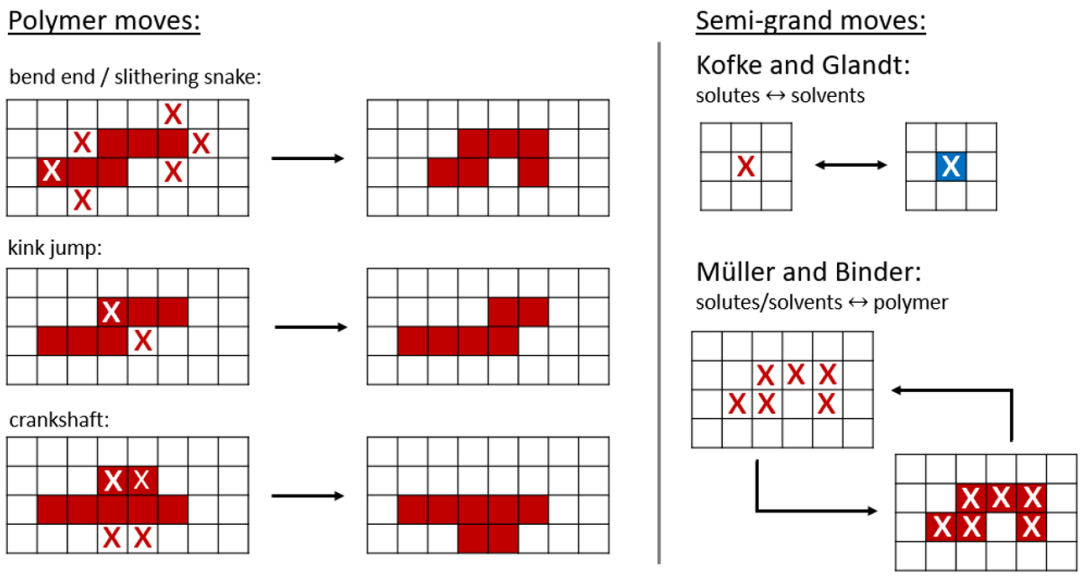

Figure 5.4: Schematic example of configurational polymer moves and both semigrand moves (i.e. Kofke-Glandt and Müller-Binder). For polymer moves, the white X's mark the initial position of the segment(s) to be moved, and the red X's mark the potential final positions of those segments. For the semigrand moves, the X's mark the lattice sites that will change identities. The color of the lattice point represents the identity of the occupant (i.e. white is solvent, blue is solute, and red is an additive segment).

ing occupants. All occupants of the chain must have the same identity. If all occupants are initially solutes or solvents, they are all changed to bonded additive segments. If all occupants are initially additive segments, they are all changed to either solutes or solvents with a set probability p_5.

Umbrella sampling

We use a rare event strategy to sample the distribution of solute clusters from pre-critical to post-critical sizes with varying number of bound oligomers. Specifically, we use umbrella sampling[49] and the multistate Bennett acceptance ratio (MBAR)[50] to compute the probability $P(\tilde{n}, m, X)$ that the largest solute cluster in the simulation is size $\tilde{n}$ and has m adsorbed oligomers with X segments in contact with the cluster surface. Clusters are contiguous groups of neighboring solutes. Adsorbed oligomers have at least one segment that contacts the cluster. Sampling was biased along the $\tilde{n}$ and X coordinates with harmonic biasing potentials:

$$U_b(n) = \frac{1}{2}k_n(\tilde{n} - \tilde{n}')^2 + \frac{1}{2}k_x(X - X')^2, \tag{5.7}$$

where $\beta(k_n, k_x) = (0.1, 0.03)$ are the restraining spring constants and $(\tilde{n}', X')$ is where the biasing potential is centered. Each window is sampled for at least 500,000 additional MC sweeps after equilibrating for 10,000 MC sweeps, where a sweep is a series of 32^3 (i.e. number of lattice points) MC moves. To visualize the nucleation barrier, we project $P(\tilde{n}, m, X)$ onto the two-dimensional Landau free energy surfaces $F_L(\tilde{n}, X)$ and $F_L(\tilde{n}, m)$:

$$\beta F_L(\tilde{n}, X) \quad = -\ln\left[P(\tilde{n}, X)/P(1, 0)\right] \tag{5.8}$$

$$\beta F_L(\tilde{n}, m) \quad = -\ln\left[P(\tilde{n}, m)/P(1, 0)\right] \tag{5.9}$$

where $P(\tilde{n}, X) = \sum_m P(\tilde{n}, m, X)$ and $P(\tilde{n}, m) = \sum_X P(\tilde{n}, m, X)$.

5.2.3 Justification of a quasi-equilibrium approach

Our simulations and analysis are based on a quasi-equilibrium approach to estimating changes in nucleation rate. It is possible that very slow diffusion of oligomers can result in nucleation before an oligomer can adsorb onto the nucleus. This can be addressed by comparing two time scales: (1) the transition path time of nucleation without the presence of oligomers and (2) characteristic time for oligomer adsorption. Our quasi-equilibrium approach should be valid if the adsorption time scale is smaller than that of the transition time. If we assume diffusion-limited attachment of both solutes and oligomers, then the transition time approximately scales with $\log(3.562\Delta F^{\ddagger}/k_B T)/D_{\text{sol}}$,[?] where $\Delta F^{\ddagger}$ is the barrier height and D_{sol} is the solute diffusion coefficient, and the adsorption time scales with $1/D_{\text{olig}}$ where D_{olig} is the oligomer diffusion coefficient.

Because the two time scales in question will be closer for oligomeric additives than for our previous study of small molecule (single lattice site) nucleants. However, we expect the gap in time scales to close slowly because $D_{\text{olig}} \propto N^{-0.6}$, where N is chain length, based on Stokes-Einstein and radius of gyration arguments. Hence it will take ca. two orders of magnitude in chain length to increase the diffusivity by ca. one order of magnitude. Based on this semi-quantitative argument, we expect the quasi-equilibrium assumption to be valid. Also note that our HEN+HON model of nucleation does *not* assume the time scale separation between transition path time for a nucleation event and adsorption of oligomers. Our confidence in the assumption is further buoyed by the apparent agreement between calculations that do (Muller-Binder) and do not (HON+HEN) rely on the assumption.

Therefore, a quasi-equilibrium approach should be valid for a sufficiently large bar-

rier. We also showed in our work on adsorbing surfactants that differences in diffusion coefficients of solutes and additives likely have little effect on estimated rates if the barrier is large.

5.3 Results and discussion

5.3.1 Effect of chain length on free energy

Figure 5.5a shows that increasing N in the range of $10 \leq N \leq 50$ at constant oligomer volume fraction increases the average surface coverage θ on solute clusters. A long chain can make more of the contacts that drive adsorption,[51,52] while losing only marginally more entropy than a short chain. Therefore increasing chain length results in more surface contacts, larger binding affinity, and lower surface energy.

Multiple chains can adsorb to the nucleus when N is sufficiently large to drive binding and when free sites remain available on the nucleus surface (see Figure 5.5b and c). For $N = 10$, the minimum free energy path (MFEP) follows the traditional CNT mechanism: growth of a cluster unassisted by an oligomer. However, a small (but not negligible) fraction of critical nuclei have one adsorbed chain. For $N = 30$ and 50, the MFEP shows that nucleation is typically assisted by one or two oligomer(s). Note that a single adsorbed $N = 50$ chain covers a large fraction of the available surface sites (see Figure 5.5a). High coverage from the first chain hinders the adsorption of the second chain and results in a large fraction of the critical nuclei with $m = 1$ (see Figure 5.5c). For larger chains ($N \gg 50$), we expect all transition states to have $m = 1$ as a single oligomer covers the surface and excludes additional chains from binding.

The impact of additive adsorption on the rate is estimated by defining a cluster free

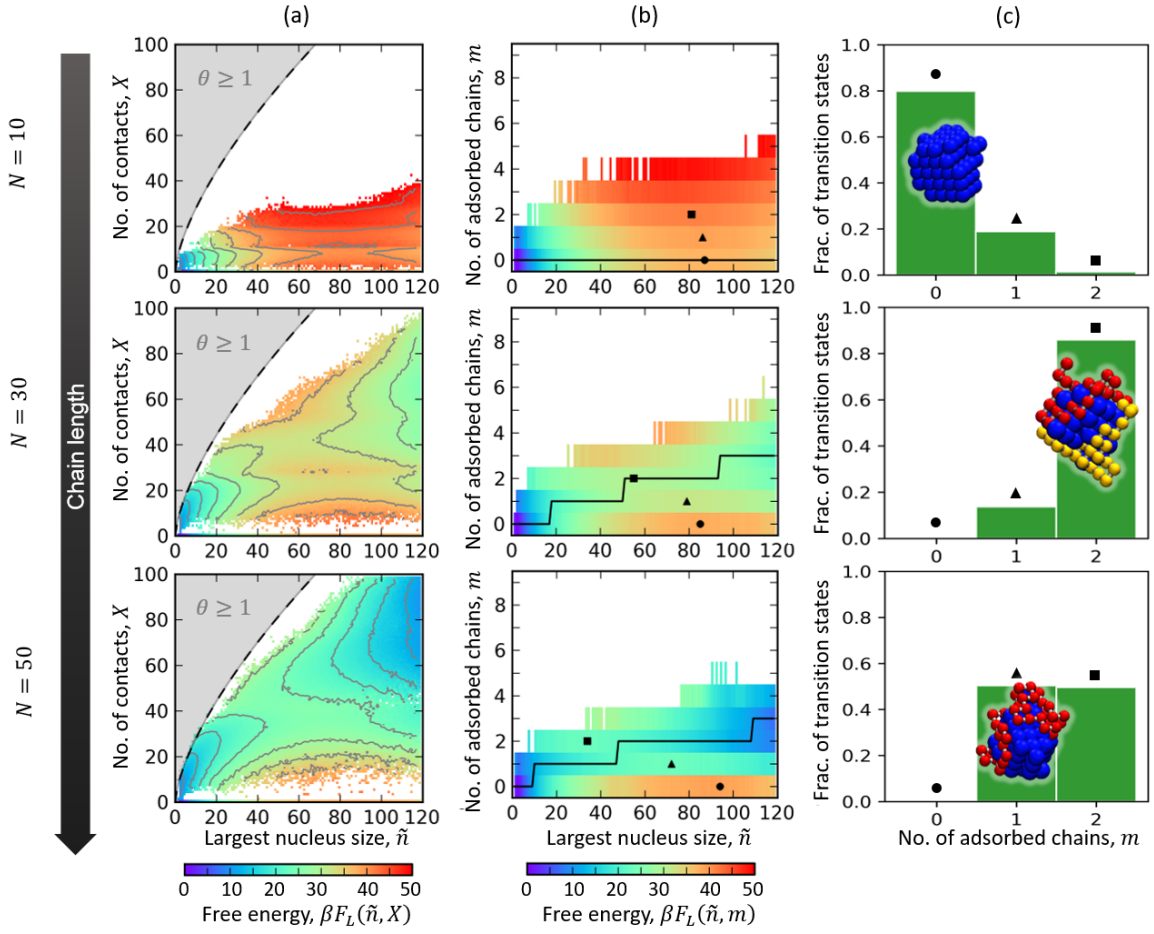

Figure 5.5: (Rows top to bottom) Free energies and histograms for chain lengths $N = 10$, 30, and 50 at comparable volume fractions ($\varphi \times 10^5 = 1.47$, 1.02, and 1.26 respectively). The segment-solute interaction parameter is $B_{01} = -3.0$. (a) $\beta F_L(\tilde{n}, X)$. The gray region above the dashed line is where X exceeds the number of available surface sites (i.e. $\theta > 1$) on a compact cubic cluster of size $\tilde{n}$. (b) $\beta F_L(\tilde{n}, m)$. •, ▲, and ■ correspond to transition states for motion along $\tilde{n}$ at fixed values of $m = 0, 1$, and 2, respectively. The black line is the minimum free energy path. (c) Histogram of m in the transition state ensemble. Examples of the most common critical nuclei (blue) are shown with adsorbed chains (red and yellow).

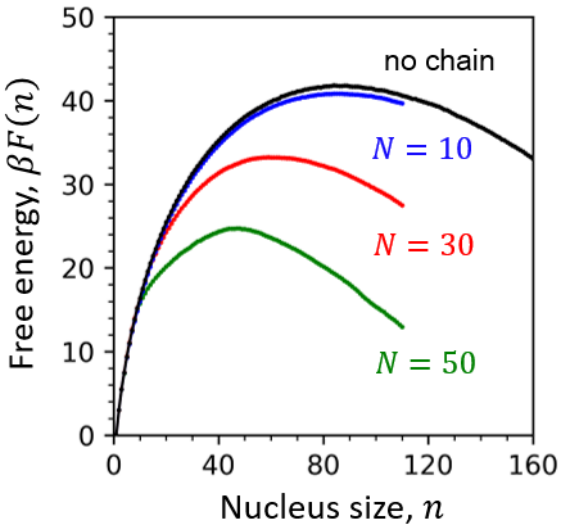

Figure 5.6: Cluster free energy (see Equation 5.10) for nucleation with and without (black) oligomeric additives of different chain lengths (N = 10, 30, and 50) at the same conditions in Figure 5.5.

energy $F(n)$ analogous to that used in CNT:

$$\beta F(n) = -\ln\left[\mathcal{N}(n)/\mathcal{N}(1)\right]. \tag{5.10}$$

where $\mathcal{N}(n)$ is the average number of clusters of size n and $\mathcal{N}(1)$ is that of dissolved solute monomers. In contrast to $P(\tilde{n}) = \sum_m \sum_X P(\tilde{n}, m, X)$, $\mathcal{N}(n)/\mathcal{N}(1)$ is independent of system size.[44,53] The free energy barrier $\Delta F^\ddagger$ is defined as $\Delta F^\ddagger = F(n^\ddagger)$, where the critical nucleus size $n^\ddagger$ maximizes $\beta F(n)$. Figure 5.6 shows that $\Delta F^\ddagger$ is strongly dependent on the length N of the oligomeric chain when oligomer volume fractions is held approximately constant. Monomeric additives ($N = 1$) did not lower the barrier (within errors), but increasing N to 10, 30, and then 50 reduced the barrier by as much as $17 k_B T$. Figure 5.5b shows the MFEP on the $F_L(\tilde{n}, m)$ landscape for each chain length N. For $N = 30$ and 50, the value of m along the MFEP jumps discontinuously from 0 to 1, from 1 to 2, etc. Each jump from m to $m+1$ occurs at a point along $\tilde{n}$ where $F_L(\tilde{n}, m)$

crosses $F_L(\tilde{n}, m+1)$, somewhat like the diabat crossings in a non-adiabatic reaction.[?]

Based on Equation 5.1, the enhanced rate J due to oligomeric additives should be approximately

$$J = J_0 \exp\left[-\beta \Delta\Delta F^{\ddagger}\right], \tag{5.11}$$

where $J_0 = A \exp[-\beta \Delta F^{\ddagger}(N, 0)]$ is the rate without oligomers and $\Delta\Delta F^{\ddagger} = \Delta F^{\ddagger}(N, \varphi) - \Delta F^{\ddagger}(N, 0)$ is the difference between the barrier with oligomers of length N at volume fraction φ and the barrier without oligomers.

5.3.2 Effect of binding strength on free energy

$\Delta\Delta F^{\ddagger}$ also depends on the strength of chain segment-solute interactions B_{01}. For example, the barrier is reduced by about $8.4 k_B T$ when $N = 30$, $B_{01} = -3.0$, and $\varphi = 1.0 \times 10^{-5}$, but the change in barrier is negligible when $B_{01} = -2.5$. In other words, previously effective promoters no longer adsorb and accelerate nucleation for all additive concentrations studied due to the reduction in oligomer segment-solute attraction. For $N = 50$, Figure 5.7 shows the additive still reduces the barrier when $B_{01} = -2.5$ but much less effectively than when $B_{01} = -3.0$.

Although we only show two different binding strengths, we feel that we have shown the extremely non-linear relationship between the nucleation barrier and binding strength. When B_{01} is below a threshold value, there is little to no rate enhancement, but above that threshold value, the rate quickly increases with binding strength. This highlights what makes adsorbing oligomeric additives different from molecular surfactants like those studied in the prior section. Relative to molecular surfactants,[26,27] the dependence on binding strength is exaggerated for oligomers due to cooperative binding of covalently linked segments. The adsorption of a single segment to the surface makes it highly likely that a nearby segment (i.e. not too many bonds away) is also adsorbed onto the surface.

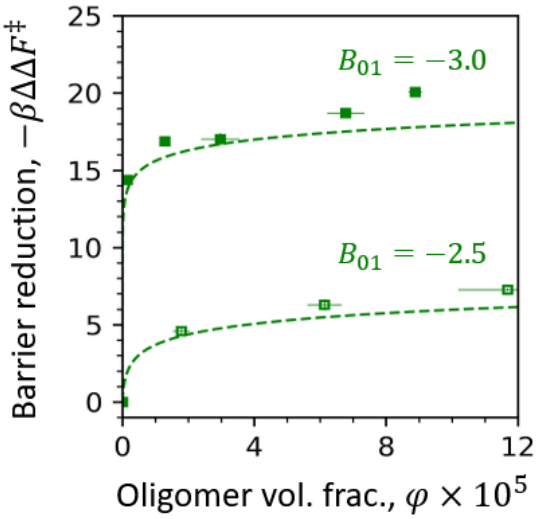

Figure 5.7: Barrier reduction $-\beta\Delta\Delta F^{\ddagger} \approx \ln(J/J_0)$ as a function of φ at two chain segment-solute interaction strengths B_{01}. Results are for chain length $N = 50$. Dashed lines are mixed HON+HEN model predictions (Equation 5.12).

Therefore, once the binding strength is strong enough to overcome the entropic cost of confining and distorting the oligomer as it is brought from the solution onto the surface, the oligomer's overall binding affinity is very sensitive to the segment-solute binding strength.

5.3.3 Effect of oligomer volume fraction on free energy

For oligomers with $B_{01} = -3.0$, we vary additive volume fraction φ by changing the additive segment-to-solvent fugacity ratios that control the acceptance probability of oligomer insertion and deletion. As expected from previous work,[26,27] higher φ more strongly promotes nucleation. However, Figure 5.7 and 5.8b show that there are two distinct regimes that describe the φ-dependence of the nucleation barrier. $-\Delta\Delta F^{\ddagger}$ rises rapidly at very low φ but levels off at larger φ.

This qualitative behavior can be understood by modeling chains as heterogeneous nucleation sites. We call this model the mixed homogeneous/heterogeneous nucleation

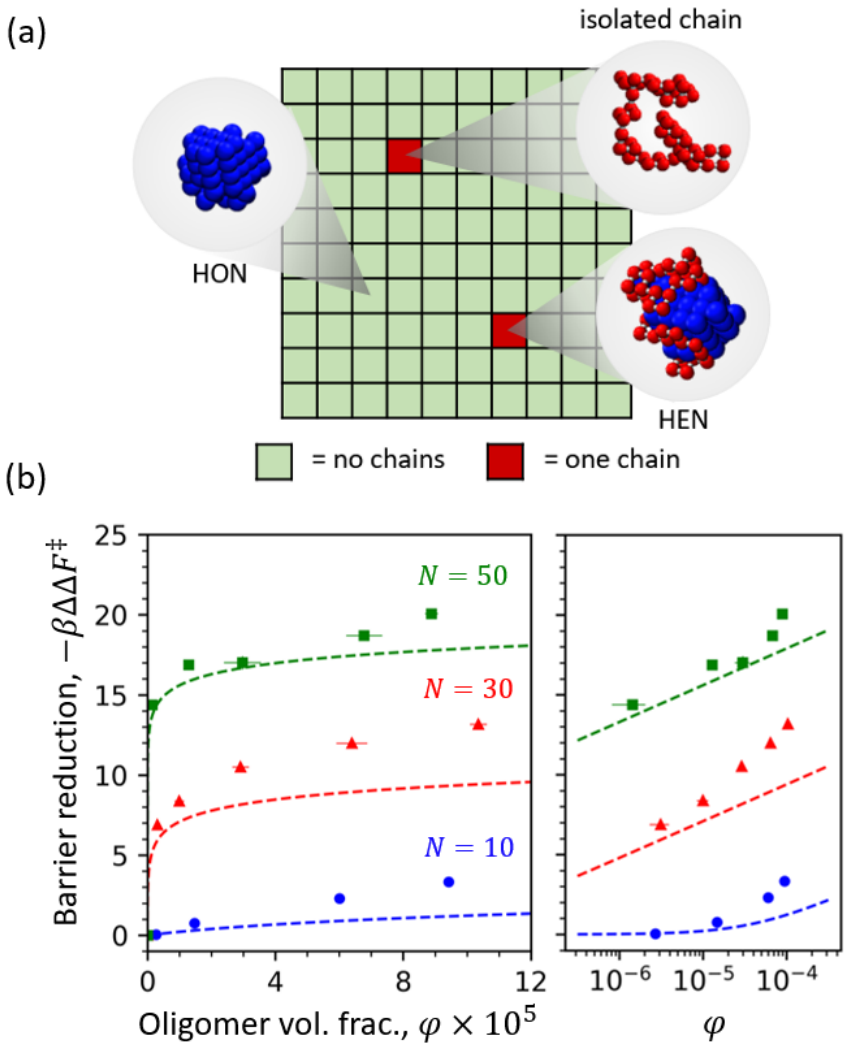

Figure 5.8: (a) Diagram of mixed HON+HEN model. (b) (left) Barrier reduction $-\beta\Delta\Delta F^{\ddagger} \approx \ln(J/J_0)$ as a function of φ for different chain lengths N for $B_{01} = -3.0$. (right) Same data on a semilog scale. Dashed lines are mixed HON+HEN model predictions (Equation 5.12).

(HON+HEN) model (see Figure 5.8a). Imagine dividing the solution into small cells where the probability distribution for the number of oligomer chains in each cell follows a Poisson distribution. For very small φ, the probability of two or more chains residing in a cell is prohibitively small, so each cell contains zero or one chain. The fraction of cells with a chain is then the product of the volume of the cell v and the concentration of oligomer chains $\varphi/v_s N$, where v_s is the volume of an oligomer segment. If the probability of a nucleus interacting with two or more chains is also small, we can estimate the apparent rate J as a volume weighted average of nucleation rates in cells with zero or one chain:

$$J = J_0 \left[1 - \frac{v\varphi}{v_s N}\right] + J_0 \frac{v\varphi}{v_s N} \exp\left[\beta\Delta F_0^{\ddagger} - \beta\Delta F_1^{\ddagger}\right], \tag{5.12}$$

where the first and second terms are the HON and HEN contributions respectively. $\Delta F_0^{\ddagger} - \Delta F_1^{\ddagger}$ is the difference in nucleation barriers in cells with zero or one chain. To compute $\Delta F_1^{\ddagger}$, the nucleation barrier is calculated for a system initiated with a single chain and simulated without Müller-Binder moves.

Our simulations agree with the model in Equation 5.12 at very low φ. However, significant deviations occur at larger φ when the predominant critical nuclei in the fully open system have more than one adsorbed chain. Therefore, the model of oligomers as isolated HEN sites only works at very dilute oligomer concentrations. Since $\Delta F_0^{\ddagger} - \Delta F_1^{\ddagger}$ increases with increasing N, the HEN barrier may become vanishingly small for very long chains. HEN events would occur almost instantly on each chain, making the HON contribution negligible in Equation 5.12. Beyond some chain length (not reached in our simulations), any further increase of N at constant volume fraction only decreases the number of cells where nucleation can be promoted, and the rate enhancement J/J_0 becomes proportional to $v\varphi/v_s N$. Equation 5.12 does not account for the possibility of multiple nuclei forming on a single chain. However, those nuclei would likely agglomerate

to form a single particle. Therefore, our simulation results and Equation 5.12 suggest the existence of an optimal oligomer size at constant oligomer volume fraction.

5.4 Conclusion

Our simulations show that soluble oligomeric additives are more potent nucleants than their monomeric counterparts, sometimes by several orders of magnitude. Long oligomers can make more energetically favorable contacts, with only marginally more entropy losses than short oligomers. Increases in binding strength, chain length, and volume fraction of oligomers all tend to lower the nucleation barrier and therefore accelerate nucleation. Unlike our simulation results for molecular-scale nucleants,[26,27] the effects of oligomeric nucleants are highly nonlinear in concentration. Very small concentrations have a large effect but only modest additional rate enhancements are obtained from further concentration increases. We have provided a mixed homogeneous/heterogeneous nucleation (HON+HEN) model where oligomers act as heterogeneous nucleation sites. The mixed HON+HEN model explains the nonlinear dependence of the free energy barriers on oligomer concentration, and it predicts an optimal oligomer chain length at constant oligomer volume fraction. Further studies are needed to verfiy the optimal chain length prediction and investigate behavior at high volume fraction where critical nuclei with multiple adsorbed additives become important.

Bibliography

[1] V. Y. Torbeev, E. Shavit, I. Weissbuch, L. Leiserowitz, and M. Lahav, *Control of crystal polymorphism by tuning the structure of auxiliary molecules as nucleation inhibitors. the beta-polymorph of glycine grown in aqueous solutions*, *Cryst. Growth Des.* **5** (2005), no. 6 2190–2196.

[2] M. Salvalaglio, T. Vetter, F. Giberti, M. Mazzotti, and M. Parrinello, *Uncovering*

molecular details of urea crystal growth in the presence of additives, *J. Am. Chem. Soc.* **134** (2012), no. 41 17221–17233.

[3] M. Salvalaglio, T. Vetter, M. Mazzotti, and M. Parrinello, *Controlling and predicting crystal shapes: The case of urea*, *Angew. Chem. Int. Ed.* **52** (2013), no. 50 13369–13372.

[4] J. D. Rimer, Z. An, Z. Zhu, M. H. Lee, D. S. Goldfarb, J. A. Wesson, and M. D. Ward, *Crystal growth inhibitors for the prevention of l-cystine kidney stones through molecular design*, *Science* **330** (2010), no. 6002 337–341.

[5] J. Chung, I. Granja, M. G. Taylor, G. Mpourmpakis, J. R. Asplin, and J. D. Rimer, *Molecular modifiers reveal a mechanism of pathological crystal growth inhibition*, *Nature* **536** (Aug., 2016) 446–450.

[6] I. R. Krauss, A. Merlino, A. Vergara, and F. Sica, *An overview of biological macromolecule crystallization*, *International Journal of Molecular Sciences* **14** (May, 2013) 11643–11691.

[7] M. Hrkovac, J. Prlic Kardum, A. Schuster, and J. Ulrich, *Influence of additives on glycine crystal characteristics*, *Chemical Engineering & Technology* **34** (2011), no. 4 611–618.

[8] A. Fazlali, S.-A. Kazemi, M. Keshavarz-Moraveji, and A. H. Mohammadi, *Impact of different surfactants and their mixtures on methane-hydrate formation*, *Energy Technology* **1** (2013), no. 8 471–477.

[9] S. Lee, J. Zhang, R. Mehta, T. K. Woo, and J. W. Lee, *Methane hydrate equilibrium and formation kinetics in the presence of an anionic surfactant*, *J. Phys. Chem. C* **111** (2007), no. 12 4734–4739.

[10] Q. S. Huo, D. I. Margolese, and G. D. Stucky, *Surfactant control of phases in the synthesis of mesoporous silica-based materials*, *Chem. Mater.* **8** (1996), no. 5 1147–1160.

[11] J.-W. Kim, J.-H. Park, H.-M. Shim, and K.-K. Koo, *Effect of amphiphilic additives on nucleation of hexahydro-1,3,5-trinitro-1,3,5-triazine*, *Crystal Growth & Design* **13** (2013), no. 11 4688–4694, [http://dx.doi.org/10.1021/cg4006423].

[12] C. Budke, C. Heggemann, M. Koch, N. Sewald, and T. Koop, *Ice recrystallization kinetics in the presence of synthetic antifreeze glycoprotein analogues using the framework of lsw theory*, *J. Phys. Chem. B* **113** (2009), no. 9 2865–2873.

[13] N. Kubota, M. Yokota, and J. Mullin, *Supersaturation dependence of crystal growth in solutions in the presence of impurity*, *Journal of Crystal Growth* **182** (1997), no. 1 86–94.

[14] W. Van Enckevort and A. Van den Berg, *Impurity blocking of crystal growth: a monte carlo study*, *Journal of crystal growth* **183** (1998), no. 3 441–455.

[15] O. Galkin and P. G. Vekilov, *Control of protein crystal nucleation around the metastable liquid-liquid phase boundary*, *Proc. Natl. Acad. Sci. U. S. A.* **97** (2000), no. 12 6277–6281.

[16] S. K. Poornachary, G. Han, J. W. Kwek, P. S. Chow, and R. B. Tan, *Crystallizing micronized particles of a poorly water-soluble active pharmaceutical ingredient: Nucleation enhancement by polymeric additives*, *Crystal Growth & Design* **16** (2016), no. 2 749–758.

[17] M. T. Storr, P. C. Taylor, J. P. Monfort, and P. M. Rodger, *Kinetic inhibitor of hydrate crystallization*, *J. Am. Chem. Soc.* **126** (2004), no. 5 1569–1576.

[18] S. Ogawa, M. Koga, and S. Osanai, *Anomalous ice nucleation behavior in aqueous polyvinyl alcohol solutions*, *Chemical Physics Letters* **480** (2009), no. 1 86 – 89.

[19] T. Inada, T. Koyama, F. Goto, and T. Seto, *Ice nucleation in emulsified aqueous solutions of antifreeze protein type iii and poly(vinyl alcohol)*, *J. Phys. Chem. B* **115** (2011), no. 24 7914–7922.

[20] R. Lakshminarayanan, S. Valiyaveettil, and G. L. Loy, *Selective nucleation of calcium carbonate polymorphs: Role of surface functionalization and poly(vinyl alcohol) additive*, *Cryst. Growth Des.* **3** (2003), no. 6 953–958.

[21] I. W. Kim, R. E. Robertson, and R. Zand, *Effects of some nonionic polymeric additives on the crystallization of calcium carbonate*, *Cryst. Growth Des.* **5** (2005), no. 2 513–522.

[22] N. Duff, Y. R. Dahal, J. D. Schmit, and B. Peters, *Salting out the polar polymorph: Analysis by alchemical solvent transformation*, *J. Chem. Phys.* **140** (2014), no. 1 014501.

[23] K. Sangwal, *Effect of impurities on the metastable zone width of solute–solvent systems*, *Journal of Crystal Growth* **311** (2009), no. 16 4050–4061.

[24] K. Sangwal, *On the effect of impurities on the metastable zone width of phosphoric acid*, *Journal of crystal growth* **312** (2010), no. 22 3316–3325.

[25] J. Anwar, P. K. Boateng, R. Tamaki, and S. Odedra, *Mode of action and design rules for additives that modulate crystal nucleation*, *Angew. Chem. Int. Ed.* **48** (2009), no. 9 1596–1600.

[26] G. G. Poon, S. Seritan, and B. Peters, *Fd nucleation: A design equation for low dosage additives that accelerate nucleation*, *Faraday Discussions* (2015).

[27] G. G. Poon and B. Peters, *Accelerated nucleation due to trace additives: A fluctuating coverage model*, *The Journal of Physical Chemistry B* **120** (2016), no. 8 1679–1684, [http://dx.doi.org/10.1021/acs.jpcb.5b08510]. PMID: 26485064.

[28] C. C. M. Luijten and M. E. H. van Dongen, *Nucleation at high pressure. i. theoretical considerations*, *Journal of Chemical Physics* **111** (1999), no. 18 8524–8534.

[29] M. A. L. J. Fransen, J. Hruby, D. M. J. Smeulders, and M. E. H. van Dongen, *On the effect of pressure and carrier gas on homogeneous water nucleation*, *Journal of Chemical Physics* **142** (2015), no. 16 64307–64307.

[30] D. Kashchiev, *Nucleation*. Elsevier Science, 2000.

[31] D. Kashchiev, *Nucleation: Basic Theory With Applications*. Butterworth-Heinemann, Oxford, 2000.

[32] R. P. Sear, *Nucleation of the crystalline phase of proteins in the presence of semidilute nonadsorbing polymer*, *J. Chem. Phys.* **115** (2001), no. 1 575–579.

[33] Y. Lifanov, B. Vorselaars, and D. Quigley, *Nucleation barrier reconstruction via the seeding method in a lattice model with competing nucleation pathways*, *The Journal of Chemical Physics* **145** (2016), no. 21 211912, [http://dx.doi.org/10.1063/1.4962216].

[34] N. Duff and B. Peters, *Nucleation in a potts lattice gas model of crystallization from solution*, *J. Chem. Phys.* **131** (2009), no. 18 184101.

[35] R. P. Sear, *Computer simulation of soft matter at the growth front of a hard-matter phase: incorporation of polymers, formation of transient pits and growth arrest*, *Faraday Discuss.* **159** (2012) 263–276.

[36] P. de Gennes, *Scaling Concepts in Polymer Physics*. Cornell University Press, 1979.

[37] M. Doi, *Introduction to Polymer Physics*. Oxford science publications. Clarendon Press, 1996.

[38] K. Binder and W. Paul, *Monte carlo simulations of polymer dynamics: Recent advances*, *Journal of Polymer Science Part B: Polymer Physics* **35** (1997), no. 1 1–31.

[39] D. Reguera, R. K. Bowles, Y. Djikaev, and H. Reiss, *Phase transitions in systems small enough to be clusters*, *J. Chem. Phys.* **118** (2003), no. 1 340–353.

[40] R. Grossier and S. Veesler, *Reaching one single and stable critical cluster through finite-sized systems*, *Cryst. Growth Des.* **9** (2009), no. 4 1917–1922.

[41] J. Wedekind, D. Reguera, and R. Strey, *Finite-size effects in simulations of nucleation*, *J. Chem. Phys.* **125** (2006), no. 21 214505.

[42] A. S. Abyzov and J. W. P. Schmelzer, *Kinetics of segregation processes in solutions: Saddle point versus ridge crossing of the thermodynamic potential barrier*, *J. Non-Cryst. Solids* **384** (2014) 8–14.

[43] V. Agarwal and B. Peters, *Nucleation near the eutectic point in a potts-lattice gas model*, *J. Chem. Phys.* **140** (2014), no. 8 084111.

[44] V. Agarwal and B. Peters, *Precipitate Nucleation: A Review of Theory and Simulation Advances*, vol. 155 of *Advances in Chemical Physics*. John Wiley & Sons, New Jersey, USA, 2014.

[45] R. Ni, F. Smallenburg, L. Filion, and M. Dijkstra, *Crystal nucleation in binary hard-sphere mixtures: the effect of order parameter on the cluster composition*, *Mol. Phys.* **109** (2011), no. 7-10 1213–27.

[46] D. A. Kofke and E. D. Glandt, *Monte-carlo simulation of multicomponent equilibria in a semigrand canonical ensemble*, *Mol. Phys.* **64** (1988), no. 6 1105–1131.

[47] M. Müller and K. Binder, *An algorithm for the semi-grand-canonical simulation of asymmetric polymer mixtures*, *Computer Physics Communications* **84** (Nov., 1994) 173–185.

[48] D. Landau and K. Binder, *A Guide to Monte Carlo Simulations in Statistical Physics*. Cambridge University Press, 2014.

[49] G. M. Torrie and J. P. Valleau, *Non-physical sampling distributions in monte-carlo free-energy estimation - umbrella sampling*, *J. Comput. Phys.* **23** (1977), no. 2 187–199.

[50] M. R. Shirts and J. D. Chodera, *Statistically optimal analysis of samples from multiple equilibrium states*, *The Journal of Chemical Physics* **129** (Aug., 2008) 124105–.

[51] P. De Gennes, *Scaling theory of polymer adsorption*, *Journal de Physique* **37** (1976), no. 12 1445–1452.

[52] P. Pincus, C. Sandroff, and T. Witten, *Polymer adsorption on colloidal particles*, *Journal de Physique* **45** (1984), no. 4 725–729.

[53] L. Maibaum, *Comment on "elucidating the mechanism of nucleation near the gas-liquid spinodal"*, *Phys. Rev. Lett.* **101** (2008), no. 1 019601.

Appendix A

Deriving equilibrium probabilities for semi-grand ensembles

A.1 Kofke-Glandt semi-grand

For the canonical ensemble (fixed $n_i VT$), the partition function is

$$Z = \sum_{states} \exp[-\beta U(state)], \tag{A.1}$$

where each state has a $\exp[-\beta U(state)]$ statistical weight on Z where $U(state)$ is the energy of the state (or configuration). This partition function corresponds to the Helmholtz

free energy, βA, which has the following differential form:

$$\begin{aligned} d(\beta A) &= U d\beta - \beta P dV + \sum_{j=0}^{c} \beta \mu_j dn_j \\ &= U d\beta - \beta P dV + \beta \mu_0 dn_{tot} + \sum_{j=0}^{c} (\beta \mu_j - \beta \mu_0) dn_j \\ &= U d\beta - \beta P dV + \beta \mu_0 dn_{tot} + \sum_{j=0}^{c} \Delta \mu_j dn_j \end{aligned} \tag{A.2}$$

where species are numbered 0 through c (i.e. $j = 0, 1, ...c$). Kofke and Glandt showed how to get the Kofke-Glandt semi-grand free energy βY from βA:

$$\beta Y = \beta A - \sum_{j=0}^{c} \beta \Delta \mu_j n_j, \tag{A.3}$$

which implies the following differential form:

$$\begin{aligned} d(\beta Y) &= d(\beta A) - \sum_{j=0}^{c} \beta \Delta \mu_j dn_j - \sum_{j=0}^{c} n_j d(\beta \Delta \mu_j) \\ &= U d\beta - \beta P dV + \beta \hat{\mu}_0 dn_{tot} - \sum_{j=0}^{c} n_j d(\beta \Delta \mu_j). \end{aligned} \tag{A.4}$$

Kofke and Glandt [1] showed that the configurational partition function for this ensemble (fixed $n_{tot} \Delta \mu_i V T$) under the constraint that the number of molecules of each species n_i belongs to the set $\{n_j\} = \{n_0, n_1, ..., n_c\}$ and has the configuration of a certain "state" is

$$\Upsilon(\{n_j\}, state) = \left[\prod_{j=0}^{c} \frac{1}{n_j!} \left[q_j \exp(\beta \Delta \mu_j) \right]^{n_j} \right] \exp[-\beta U(state)]. \tag{A.5}$$

The inner-most bracketed quantity is the non-canonical contribution to the partition function of a single molecule of species i. The $1/n_j!$ accounts for molecules of the same species being indistinguishable. The partition function with only the $\{n_j\}$ constraint is

just the sum of the previous one over all possible configurations:

$$\begin{aligned}\Upsilon(\{n_j\}) &= \sum_{states} \Upsilon(\{n_j\}, state) \\ &= \left[\prod_{j=0}^{c} \frac{1}{n_j!} \left[q_j \exp(\beta\Delta\mu_j)\right]^{n_j}\right] Z. \end{aligned} \tag{A.6}$$

Similarly, the full partition function is the sum of $\Upsilon(\{n_j\})$ over all possible sets $\{n_j\}$:

$$\Upsilon = \sum_{\{n_j\}} \Upsilon(\{n_j\}) \tag{A.7}$$

such that $n_{tot} = \sum_{j=0}^{c} n_j$ is constant for all sets. We can also rewrite Equation A.7 using the multinomial theorem:

$$\Upsilon = \frac{1}{n_{tot}!}[\Upsilon_1]^{n_{tot}} Z, \tag{A.8}$$

where the single molecule non-canonical partition function Υ_1 is

$$\Upsilon_1 = \sum_{i=0}^{c} \left[q_j \exp(\beta\Delta\mu_j)\right], \tag{A.9}$$

which is the sum of single molecule non-canonical partition function of type i over all types. Since each molecule has the same partition function (can be one of the $c+1$ types), $1/n_{tot}!$ is used to account for indistinguishable molecules (which can be one of the $c+1$ types).

Using the definition of the fugacity and single molecule partition function, we can show the following:

$$\begin{aligned} f_j &= \exp(\beta\mu_j - \beta\mu_j^0) \\ &= q_j \exp(\beta\mu_j), \end{aligned} \tag{A.10}$$

$$\frac{f_j}{f_0} = \frac{q_j}{q_0} \exp(\beta \Delta \mu_j). \tag{A.11}$$

$$q_j \exp(\beta \Delta \mu_j) = q_0 \frac{f_j}{f_0} \tag{A.12}$$

This is used to simplify Equation A.9 to

$$\Upsilon_1 = q_0 \sum_{i=0}^{c} \left(\frac{f_i}{f_0} \right). \tag{A.13}$$

This partition function implies that the equilibrium probability that molecule k is type j is

$$P_k^{eq}(j) = \left(\frac{q_0 f_j / f_0}{\Upsilon_1} \right) \left(\frac{\exp[-\beta U_k(j)]}{Z_k} \right), \tag{A.14}$$

where Z_k is the canonical partition function of that molecule:

$$Z_k = \sum_{j=0}^{c} \exp[-\beta U_k(j)] \tag{A.15}$$

and $U_k(j)$ is the sum of all interactions with molecule k that is type j (i.e. energy of the molecule). Therefore the probability that molecule k is type j relative to that of type i is

$$\frac{P_k^{eq}(j)}{P_k^{eq}(i)} = \frac{f_j}{f_i} \exp[-\beta (U_k(j) - U_k(i))]. \tag{A.16}$$

A.2 Muller-Binder semi-grand

Muller and Binder modified the semi-grand ensemble to preserve the total number of *segments* instead of total number of molecules. To obtain their equilibrium probability

distribution, we can rewrite Equation A.2 in terms of monomers instead of molecules:

$$\begin{aligned} d(\beta A) &= U d\beta - \beta P dV + \sum_{j=0}^{c} \frac{\beta \mu_j}{\ell_i} dN_j \\ &= U d\beta - \beta P dV + \frac{\beta \mu_0}{\ell_0} dN_{tot} + \sum_{j=0}^{c} \left(\frac{\beta \mu_j}{\ell_i} - \frac{\beta \mu_0}{\ell_0} \right) dN_j \\ &= U d\beta - \beta P dV + \beta \hat{\mu}_0 dN_{tot} + \sum_{j=0}^{c} \beta \Delta \hat{\mu}_i dN_j \end{aligned} \tag{A.17}$$

We can get the Muller-Binder semi-grand free energy $\beta \hat{Y}$ from βA:

$$\beta \hat{Y} = \beta A - \sum_{j=0}^{c} \beta \Delta \hat{\mu}_j N_j, \tag{A.18}$$

which implies the following differential form:

$$\begin{aligned} d(\beta \hat{Y}) &= d(\beta A) - \sum_{j=0}^{c} \beta \Delta \hat{\mu}_j dN_j - \sum_{j=0}^{c} N_j d(\beta \Delta \hat{\mu}_j) \\ &= U d\beta - \beta P dV + \beta \hat{\mu}_0 dN_{tot} - \sum_{j=0}^{c} N_j d(\beta \Delta \hat{\mu}_j). \end{aligned} \tag{A.19}$$

Equation A.19 is analogous to Equation A.4 (Kofke-Glandt version). Number of molecules is simply replaced with number of segments, and chemical potentials are simply replaced with per segment chemical potentials. Therefore, the partition function for this ensemble (fixed $N_{tot} \Delta \hat{\mu}_i V T$) is also almost identical to Equation A.8:

$$\hat{\Upsilon} = \frac{1}{N_{tot}!} [\hat{\Upsilon}_1]^{N_{tot}} Z, \tag{A.20}$$

where the single monomer non-canonical partition function resembles Equation A.13:

$$\hat{\Upsilon}_1 = \hat{q}_0 \sum_{i=0}^{c} \left(\frac{\hat{f}_i}{\hat{f}_0} \right). \tag{A.21}$$

The only difference is that we replace n_i with N_i, q_0 with $\hat{q}_0$, and f_i with $\hat{f}_i$. The hat accent just means everything is on a per monomer basis instead of per molecule basis (as is typical for traditional chemical potentials).

The equilibrium probability for monomer k (not molecule) is type j is very similar to Kofke and Glandt's:

$$P^{eq}_{\{k_m\}}(j) = \left(\frac{\hat{q}_0 \hat{f}_j / \hat{f}_0}{\hat{\Upsilon}_1} \right) \left(\frac{\exp[-\beta \hat{U}_k(j)]}{\hat{Z}_k} \right), \tag{A.22}$$

where $\hat{Z}_k$ is the canonical partition function of that monomer:

$$\hat{Z}_k = \sum_{j=0}^{c} \exp[-\beta \hat{U}_k(j)] \tag{A.23}$$

and $\hat{U}_k(j)$ is the sum of all interactions with monomer k of type j (i.e. energy of the monomer). Therefore the probability that the entire set of m_{tot} molecules, $\{k_m\}$, are all type j is

$$\begin{aligned} P^{eq}_{\{k_m\}}(j) &= \prod_{m=1}^{m_{tot}} \left(\frac{\hat{q}_0 \hat{f}_j / \hat{f}_0}{\hat{\Upsilon}_1} \right) \left(\frac{\exp[-\beta \hat{U}_{k_m}(j)]}{\hat{Z}_{k_m}} \right) \\ &= \left(\frac{\hat{q}_0 \hat{f}_j / \hat{f}_0}{\hat{\Upsilon}_1} \right)^{m_{tot}} \exp\left[-\sum_{m=1}^{m_{tot}} \beta \hat{U}_{k_m}(j) \right] \prod_{m=1}^{m_{tot}} \frac{1}{\hat{Z}_{k_m}}. \end{aligned} \tag{A.24}$$

Therefore we can describe the probability that all $\{k_m\}$ monomers, which are all close

enough to make a chain, are type j relative to that of type i is

$$\frac{P^{eq}_{\{k_m\}}(j)}{P^{eq}_{\{k_m\}}(i)} = \left(\frac{\hat{f}_j}{\hat{f}_0}\right)^{m_{tot}} \exp\left[-\sum_{m=1}^{m_{tot}}\left[\beta\hat{U}_{k_m}(j) - \beta\hat{U}_{k_m}(i)\right]\right]. \tag{A.25}$$

If j is the larger chain and $\ell_j/\ell i$ is an integer, Muller-Binder semi-grand moves involves changing $m_{tot} = \ell_j$ monomers from either a single molecule of j into multiple molecules of i or the reverse. Equation A.25 shows that we can think of Muller-Binder semi-grand moves as just doing ℓ_j Kofke-Glandt semi-grand moves if all fugacities are on a per monomer basis.

Bibliography

[1] D. A. Kofke and E. D. Glandt, *Monte-carlo simulation of multicomponent equilibria in a semigrand canonical ensemble*, *Mol. Phys.* **64** (1988), no. 6 1105–1131.